

博士学位論文

リチウム空気電池における過酸化リチウ  
ムの電荷移動特性の第一原理計算

東北大学大学院工学研究科  
知能デバイス材料学専攻

康利静

2015 年 1 月 15 日

Doctoral Thesis

First Principles Investigation of Charge  
Transport Properties of Lithium Peroxide  
in Lithium-Air Battery

Lijing Kang

Department of Materials Science, Graduate School of  
Engineering  
WPI-AIMR, Tohoku University

Jan. 15, 2015



## Acknowledgments

First of all, I would like to express my great thanks to my supervisor Prof. Mingwei Chen for accepting me to study in his Lab., and giving my very important guidance during my Ph.D study. His supervision would have a deep impact in my future study and work.

I would also like to express my sincerest thanks and appreciation to Prof. Yoshiyuki Kawazoe for his continuous support and kind help ever since I came to Japan, without which I would not be able to finish my entire study here.

Then I wish to show my special thanks to Pro. Masaru Tsukada for allowing me to join his group and giving me the opportunity to study and communicate with the members in his group, which helped a lot to fulfill my Ph.D study.

Thanks are also due to Prof. Takashi Goto, Prof. Hiroshi Ohtani, and Prof. Ying Chen for their kind help as well as valuable comments and criticisms. All of their suggestions greatly enhanced this current work.

The support from associate Prof. Takeshi Fujita, Akihiko Hirata, Kazuto Akagi, Rodion Belosludov, and Dr. Yunye Liang, Dr. Vei Wang are also greatly appreciated. Their patient explanation and detailed instructions are essential to ensure the accomplishment of this research work.

I would also like to thank all the other members in Chen Lab., Akagi group, and Kawazoe group, as well as the staff members of the Center for Computational Materials Science, IMR for providing the SR16000 supercomputing resources and the technical supports.

I'm also grateful for the JST-CREST research fund about this Ph.D thesis work as well as the financial support from 'China Scholarship Council' for my study in Japan.

Finally, I wish to show my personal thanks to my family for their continuous love, encourage, and support during my entire study period.



## Abstract

The aim of this thesis is to investigate the charge transport properties of lithium peroxide ( $\text{Li}_2\text{O}_2$ ), which is the dominant discharge product of lithium air batteries (LAB), by applying first principles calculations.

LAB have now drawn increasing research interests as a new generation of batteries for long distance electric vehicles, because of their extremely high theoretical specific energy density. However despite the promising advantages of LAB, there are still severe technical as well as theoretical challenges regarding to the practical application of LAB. And the charge transport property within  $\text{Li}_2\text{O}_2$  is one of the most important issues. Bulk  $\text{Li}_2\text{O}_2$  is an insulator, and it is formed on the surface of electrode during discharge process. Once it fully covers the surface, the charge transport process would become the rate limiting factor of the battery performance.

In the recent two decades, there have been many research papers regarding the charge transfer mechanisms in  $\text{Li}_2\text{O}_2$ , and difference mechanisms have been proposed theoretically. However a well-accepted theory has not yet been achieved. Detailed and systematical investigations of the different factors that might affect the conductivity of  $\text{Li}_2\text{O}_2$  are also quite few.

Thus in this study, we employed the first principles calculation approach to investigate the defect and interface induced conductivity in  $\text{Li}_2\text{O}_2$ . Starting from the bulk calculation, we presents a detailed comparison of the bulk bandgap calculated by applying different methods, including standard DFT, hybrid DFT, as well as the state-of-the-art many-body GW approximation in Chapter 3. Chapter 4 and 5 give a systematical investigation of the intrinsic and extrinsic point defects in  $\text{Li}_2\text{O}_2$ . The properties of native vacancies, intended metal/semimetal doping and the unavoidable hydrogen impurity, as well as their effects relevant to the conductivity of  $\text{Li}_2\text{O}_2$  were calculated and discussed thoroughly. In Chapter 6, the interface between Au and  $\text{Li}_2\text{O}_2$ , which is driven by the experimental conditions, has been investigated. A comparison of the coherent and semicoherent interface configurations was carried out. The strain induced artificial effect in the coherent case was discussed, and the effect of the gold substrate on the conductivity of  $\text{Li}_2\text{O}_2$  was emphasized.

Finally, we summarized the conclusion of this current study in Chapter 7. Bulk  $\text{Li}_2\text{O}_2$  is a large bandgap insulator, and as there is no experimental bandgap value available now, a careful theoretical calculation of its bandgap is essential to obtain a reliable prediction of its other properties. The defective properties of  $\text{Li}_2\text{O}_2$  are dominated by the ability of  $\text{O}_2^{-2}$  peroxide anion to change its charge states. Li vacancy migration and hole polaron hopping are predicted to be the dominating charge transfer mechanisms in intrinsic  $\text{Li}_2\text{O}_2$ . Doping of light metal/semimetal elements in  $\text{Li}_2\text{O}_2$  would not be an effective way to improve its conductivity due to the formation of highly localized polarons within  $\text{O}_2^{-2}$  peroxide anion. And the possible existence of hydrogen impurities will also counteract with the prevailing conductivity of  $\text{Li}_2\text{O}_2$ , and hydrogen behaviors as compensating sources in both n-type and p-type  $\text{Li}_2\text{O}_2$ . However the calculation of Au/ $\text{Li}_2\text{O}_2$  interface system demonstrated that the interface induced Au states will fill the gap between the valence and conduction band of  $\text{Li}_2\text{O}_2$ , resulting in conductivity. This result is consistent with the experimental founding that the using of nano-porous gold substrate for the cathode of LAB will greatly decrease the overpotential and enhance the cycling stability.

GENERAL INTRODUCTION .....	1
REFERENCES .....	5
CHAPTER 1 BACKGROUND AND MOTIVATION.....	7
1.1 BACKGROUND.....	7
1.1.1 Mechanism of LAB .....	7
1.1.2 Challenges and problems related to LAB .....	10
1.1.3 Literature review about the charge transport mechanism of $\text{Li}_2\text{O}_2$ .....	12
1.2 MOTIVATION AND OBJECTIVES .....	14
REFERENCES .....	16
CHAPTER 2 THEORETICAL BACKGROUND .....	19
2.1 INTRODUCTION.....	19
2.2 GROUND STATE PROPERTIES.....	19
2.2.1 Many-body problem.....	19
2.2.2 Density function theory (DFT) .....	20
2.2.2.1 Thomas-Fermi-Dirac approximation .....	21
2.2.2.2 Hohenberg-Kohn theorem .....	21
2.2.2.3 Kohn-Sham equation.....	23
2.2.3 Exchange-correlation approximations .....	25
2.2.3.1 Local density approximation (LDA) .....	25
2.2.3.2 Generalized gradient approximation (GGA) .....	26
2.2.3.3 Hybrid functional.....	27
2.3 EXCITED STATE PROPERTIES .....	27
2.3.1 GW approximation.....	28
2.3.1.1 Green's function .....	28
REFERENCES .....	30
CHAPTER 3 BULK PROPERTIES OF $\text{Li}_2\text{O}_2$ .....	31
3.1 INTRODUCTION.....	31
3.2 CALCULATION METHODS .....	31
3.3 RESULTS AND DISCUSSION .....	33
3.3.1 Crystal structure .....	33
3.3.1.1 Symmetric analysis of atomic positions in $\text{Li}_2\text{O}_2$ .....	33
3.3.1.2 Lattice constants.....	34
3.3.2 electron density distribution.....	35
3.3.3 Electronic structure.....	36
3.3.2.1 Density of states (DOS).....	36
3.3.2.2 Bandgap calculation .....	37
3.4 CONCLUSIONS .....	43
REFERENCES .....	45

CHAPTER 4 INTRINSIC POINT DEFECTS IN $\text{Li}_2\text{O}_2$ .....	47
4.1 INTRODUCTION.....	47
4.2 CALCULATION METHODS .....	48
4.2.1 Defect types .....	48
4.2.2 Modeling methods .....	48
4.3.3 Calculation parameters .....	49
4.3 RESULTS AND DISCUSSION .....	50
4.3.1 Formation energy .....	50
4.3.2 Electronic structure.....	53
4.3.2.1 Electron and hole polarons.....	53
4.3.2.2 Li vacancy.....	55
4.3.2.3 O vacancy.....	56
4.3.2.4 Di-O vacancy.....	57
4.3.3 Defect levels .....	58
4.4 CONCLUSIONS .....	61
REFERENCES .....	63
CHAPTER 5 EXTRINSIC DOPING EFFECT IN $\text{Li}_2\text{O}_2$ .....	65
5.1 INTRODUCTION.....	65
5.2 CALCULATION METHODS .....	66
5.3 RESULTS AND DISCUSSION .....	68
5.3.1 Metal/semimetal doping in $\text{Li}_2\text{O}_2$ .....	68
5.3.1.1 Formation energy .....	68
5.3.1.2 Atomic configuration .....	70
5.3.1.3 Defect levels .....	71
5.3.1.4 Si doping.....	73
5.3.2 Hydrogen impurity in $\text{Li}_2\text{O}_2$ .....	75
5.3.2.1 Formation energy .....	75
5.3.2.2 Atomic bonding configuration .....	79
5.3.2.3 Electronic structure.....	81
5.3.2.3.1 <i>Interstitial hydrogen</i> (Hiq) .....	81
5.3.2.3.2 <i>H substitution of Li</i> (HLiq) .....	84
5.3.2.3.3 <i>H substitution of O</i> (H0q).....	85
5.3.2.3.4 <i>H substitution of di-O</i> (H02q).....	86
5.4 CONCLUSIONS .....	87
REFERENCES .....	89
CHAPTER 6 INTERFACIAL PROPERTIES BETWEEN $\text{Au}/\text{Li}_2\text{O}_2$ .....	91
6.1 INTRODUCTION.....	91
6.1.1 Experimental background.....	91
6.1.2 Interface model between Au and $\text{Li}_2\text{O}_2$ .....	93

## Content

---

6.1.2.1 Coherent interface model .....	93
6.1.2.2 Semicoherent interface model.....	94
6.2 CALCULATION METHODS .....	98
6.2.1 Coherent interface.....	98
6.2.2 Semicoherent interface .....	101
6.3 RESULTS AND DISCUSSION .....	102
6.3.1 Coherent interface .....	102
6.3.1.2 Atomic configuration .....	102
6.3.1.2 Formation energy .....	103
6.3.1.3 Differential charge density .....	105
6.3.1.4 Electronic structure.....	106
6.3.2 Semicoherent interface .....	109
6.3.2.1 Atomic configuration .....	109
6.3.2.2 Differential charge density .....	110
6.3.2.3 Electronic structure.....	111
6.4 CONCLUSIONS .....	115
REFERENCES .....	117
CHAPTER 7 FINAL CONCLUSIONS .....	119





## General Introduction

As one of the most fundamental elements in our universe, energy defines the ability to do work. The worldwide demand for energy keeps accelerating every year. In 2013 the global primary energy consumption exhibits a growth of 2.3%, with fossil fuels as the dominating fuel types due to their significant energy density. Oil takes 32.9% of the global energy consumption, remaining the world's leading fuel, whereas natural gas and coal account for 23.7% and 30.1% respectively. And for fossil fuels, the global consumption rose more rapidly than production, which suggests that global CO<sub>2</sub> emission from energy use also accelerated in 2013.<sup>1</sup> The desire to solve the serious environmental issues (climate change/global warming), especially the green house effect due to the emission of CO<sub>2</sub>, as well as the concern of the finite fossil fuel supplies and fluctuation of oil prices, have leading to a worldwide interest in pursuit of new energy sources and energy storage devices.

Besides, as the world's leading fuel, oil is used mostly for transportation applications. However, the city pollution caused by automobiles has forced people to work on a transition from the current internal combustion engine vehicle to a new electrified road transportation system. The advent of the first gasoline-electric hybrid automobile 'Lohner-Porsche Mixte Hybrid' in 1901 by Ferdinand Porsche heralded the beginning of hybrid electric vehicles (HEVs), following by the proposal of plug-in hybrid vehicles (PHEVs) by Professor Andrew Frank in 1990s. Both PHEVs and the ultimately pure electric vehicles (EVs) will eventually accelerate the transition process.<sup>2</sup>

Towards the goal of complete electrification of road transportation, the major technical challenge is to develop high efficiency electrical energy storage and conversion systems. The electrochemical storage devices, which convert the internal chemical energy into electricity, become the most attractive option, since both energy forms have the same energy carrier of electrons.<sup>3</sup> The development in battery technology over the past decades has enabled the rechargeable batteries systems to be a promising energy sources for EVs. However the main technical hurdle of the current battery systems is the

insufficient storage capacity. Figure 1 summaries a comparison of energy densities between various types of battery systems and gasoline.<sup>2,4</sup>

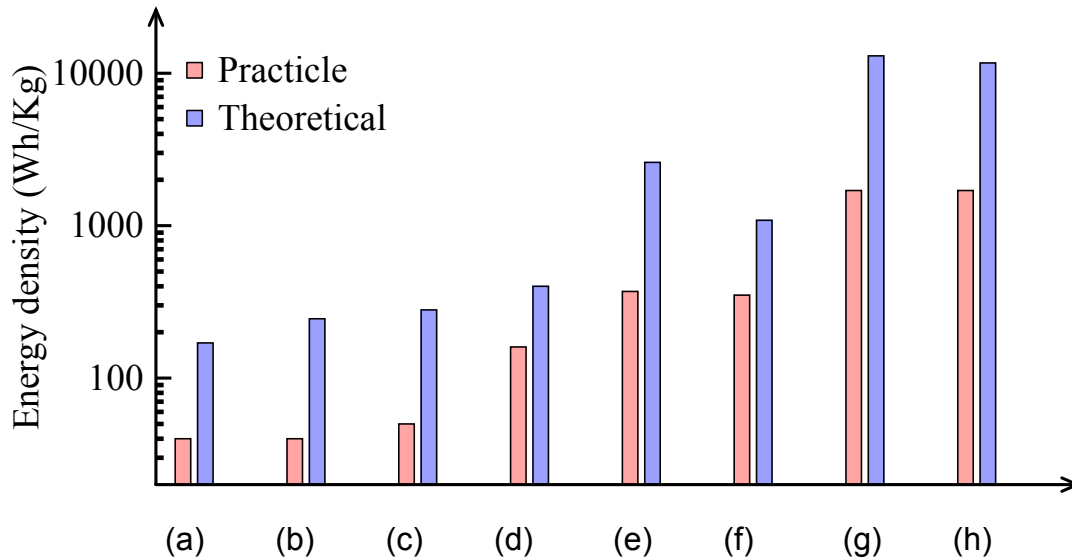


Figure 1: The theoretical and practical gravimetric energy densities (Wh/kg) for various types of rechargeable battery systems compared to gasoline. (a) Lead-acid, (b) Ni-Cd, (c) Ni-MH, (d) Li-ion, (e) Li-S, (f) Zn-Air, (g) Gasoline, (i) Li-Air.

Compared to that of gasoline, the gravimetric energy density of currently most successful Li-ion batteries (LIB), which is in the range of 100 ~ 200 Wh/kg, is still much lower for long distance EVs. An estimation made by Peter G. Bruce et al showed that the current LIB would support a driving distance of around 160km. Even in the future LIB is fully developed, its theoretical energy density of ~400 Wh/kg is still insufficient to meet the demands of long distance EVs, which should be more than 700 Wh/kg. New battery chemistries should be explored for this application, and the metal-air battery systems have attracted much attention as the most likely candidates due to their high energy density than the conversional battery systems. The concept of metal-air battery means using the oxidation of metal with oxygen in the air to produce electricity. The setup of this battery includes a pure metal anode, an external ambient air cathode as well as different types of electrolyte. Due to the utilization of oxygen from air rather than storing it in the batteries, the energy density of metal-air batteries is highly increased. Figure 2 shows the theoretical energy density of different metal-air battery chemistries.

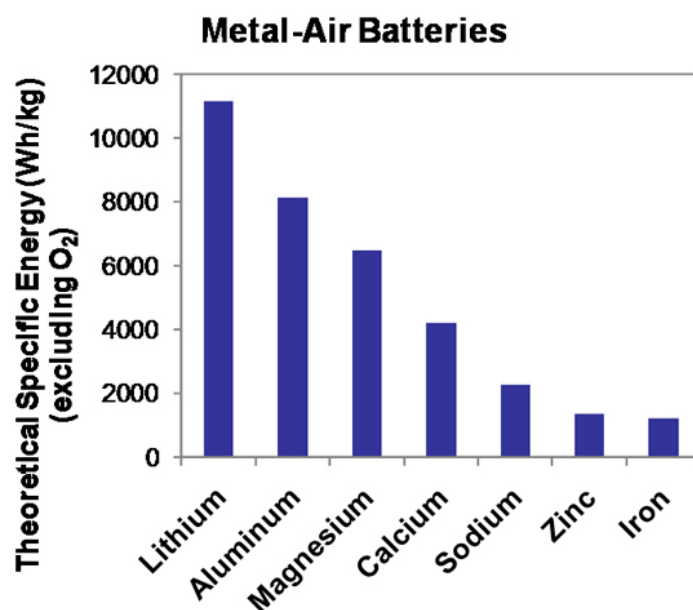


Figure 2: Theoretical energy density of various metal-air battery systems. (<https://electrochemistry.grc.nasa.gov/current-projects/batteries-for-o2-concentrators/>)

Among the different metal systems, Lithium-air batteries (LAB) have drawn increasing attention and are under intensive investigation both experimentally and theoretically over the recent two decades, owing to their extremely high theoretical specific energy density. Thanks to the lightweight of lithium metal, the theoretical specific energy density of LAB calculated according to the oxidation of pure lithium metal is as high as 11430 Wh/kg, which is comparable to that of gasoline.<sup>2</sup> This makes LAB a promising alternative of gasoline for the ultimate long distance EVs.

However, despite the increasing research interests focused on LAB, there are still many severe technical challenges before the commercial adoption of LAB, including the high charge/discharge over potential, large charge/discharge polarization, low energy efficiency, electrolyte side reactions, and so on. These existing problems are believed to be close related to the limited charge transfer process during batteries operation. Unlike mechanism of ion migration in LIB, the redox reaction in LAB requires an efficient charge transport. Especially, due to the insulating nature of the discharge product lithium peroxide ( $\text{Li}_2\text{O}_2$ ), the charge transfer within  $\text{Li}_2\text{O}_2$  becomes a rate limiting factor of the batteries performance.

In this thesis, a fundamental investigation of the charge transport properties in lithium peroxide is performed by applying first principles calculations. The bulk, defective as well as interfacial properties of  $\text{Li}_2\text{O}_2$  with relevant to its charge conductivity are calculated and discussed in detail.

The contents of this thesis are organized as follows:

Chapter 1: The background including literature review and the motivation as well as objectives of this study are explained;

Chapter 2: A brief illustration of the many-body problem, density functional theory (DFT) together with the different forms of exchange correlation approximations including LDA, GGA and Hybrid DFT theory, as well as the many body GW approximation are presented. The supercell method for charged point defects calculations and the slab method for interfacial calculation are explained.

Chapter 3: Bulk properties especially the electronic structure and bandgap of  $\text{Li}_2\text{O}_2$  are calculated by applying different methods of DFT, hybrid DFT and GW approximation.

Chapter 4: Intrinsic point defects in  $\text{Li}_2\text{O}_2$  including different types of small polarons and vacancies are calculated in detail, and the defects induced conductivity is evaluated.

Chapter 5: Extrinsic doping effect in  $\text{Li}_2\text{O}_2$  including metal/semimetal doping and hydrogen impurity are systematically investigated.

Chapter 6: Interfacial properties between  $\text{Au}/\text{Li}_2\text{O}_2$  in the coherent and semicoherent ranges are calculated and discussed in detail.

Chapter 7: Final conclusion of this study is summarized.

## REFERENCES

1. BP, *Statistical Review of World Energy*, 2014, 1–48.
2. G. Girishkumar, B. McCloskey, A. C. Luntz, S. Swanson, and W. Wilcke, *J. Phys. Chem. Lett.*, 2010, **1**, 2193–2203.
3. J. M. Tarascon, *Philosophical Transactions of the Royal Society a-Mathematical Physical and Engineering Sciences*, 2010, **368**, 3227–3241.
4. J. Wang, Y. Li, and X. Sun, *Nano Energy*, 2013, **2**, 443–467.



## Chapter 1 Background and Motivation

### 1.1 Background

#### 1.1.1 Mechanism of LAB

LAB was initially proposed by Littauer and Tsai in 1970s,<sup>1,2</sup> and Abraham and Jiang demonstrated the first experimentally rechargeable non-aqueous Li-air batteries in 1996.<sup>3</sup> Then over the past two decades, Li-air batteries have drawn increasing attention and are under intensive investigations by both experimentalists and theorists due to their extremely high theoretical specific energy density. Fig. 1.1 gives a schematic draw of one LAB battery cell during discharge and recharge.

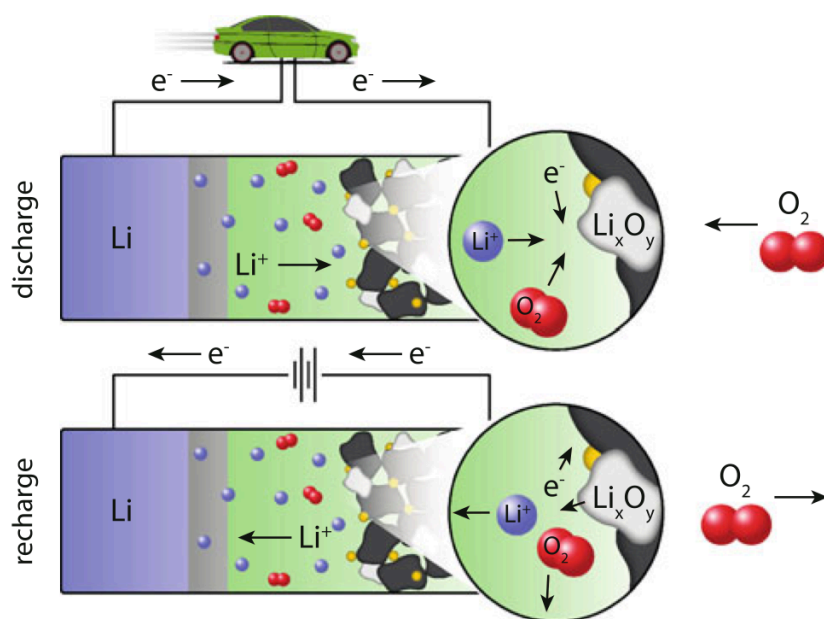
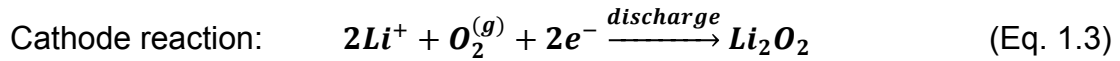
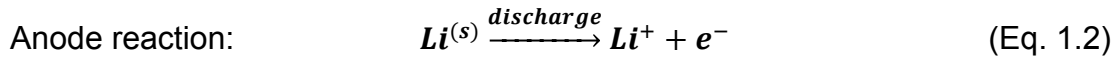
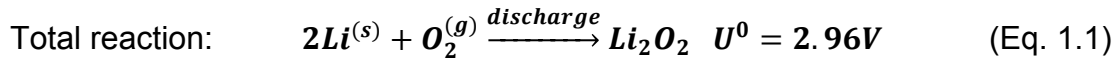


Fig. 1.1: Schematic draw of one rechargeable LAB battery cell during discharge and recharge.<sup>4</sup>

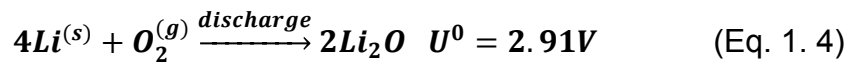
The architecture of LAB is composed of bulk metallic lithium as anode, porous air-breathing electrode as cathode and an electrolyte. In most of the current research, pure oxygen instead of air is used as cathode given the fact that  $CO_2$  and  $H_2O$  in air will interfere the battery behavior. So sometimes, the item 'Li- $O_2$  battery' rather than LAB is used. Depending on the different states of

electrolyte, LAB can be classified into four different types: aprotic/non-aqueous, aqueous, mixed aqueous-protic, as well as solid state LAB. And the battery reactions in different chemical architectures are depended on the electrolyte around the cathode. For non-aqueous and solid state electrolyte, the discharge products are the insoluble lithium oxide,  $\text{Li}_2\text{O}_2$  and possibly  $\text{Li}_2\text{O}$ ; in contrast, for aqueous and mixed electrolyte, the discharge products are the soluble  $\text{LiOH}$  or other lithium salts. Since until now only the non-aqueous LAB is demonstrated to be rechargeable,<sup>5</sup> it has become the worldwide most widely investigated version.

The electrochemical reaction in non-aqueous LAB during discharge is the oxidation of lithium to form  $\text{Li}_2\text{O}_2$ , and during recharging  $\text{Li}_2\text{O}_2$  will undergo a reverse decomposition at the applied recharge voltage. The anode reaction is the oxidation of lithium metal upon discharging, and the cathode reactions are the oxygen reduction reaction (ORR) and oxygen evolution reaction (OER) respectively during discharge and recharge. The reaction equations are listed as following:



Some experimental observations also proposed the mechanism of the formation of  $\text{Li}_2\text{O}$  as the discharge product:<sup>6</sup>



As indicated by the above reactions, both the formation of  $\text{Li}_2\text{O}_2$  and  $\text{Li}_2\text{O}$  are thermodynamically possible and have quite close potentials. However the actual product are strongly depended on the cathode catalysts.<sup>7</sup> Even though the formation of  $\text{Li}_2\text{O}$  will theoretically increase the stored energy (twice the Li per O),<sup>8</sup> but it may be difficult to be recharged. According a recent theoretical calculation, the stable surfaces of  $\text{Li}_2\text{O}_2$  are half-metallic, while that of  $\text{Li}_2\text{O}$  are



insulating the same as the bulk.<sup>9</sup> The reversibility of the different  $\text{Li}_2\text{O}_2$  and  $\text{Li}_2\text{O}$  related systems are supposed to be explained by the above conductivity. The equilibrium potential of the above discharge reaction is calculated based on NIST-JANAF thermochemical table according to the Nernst equation:<sup>10-12</sup>

$$U_0 = -\Delta G/nF \quad (\text{Eq. 1.5})$$

where,  $\Delta G = -5.91\text{eV}$  is the experimental Gibbs free energy of  $\text{Li}_2\text{O}_2$ ,  $n=2$  is the number of electrons transferred during the discharge reaction per mole reactant, and  $F=96500\text{C/mol}$  is the Faraday constant, which is the magnitude of the electric charge per mole of electrons.

One of the key criteria to evaluate the battery systems is their energy density. The gravimetric and volumetric energy densities are defined as the energy provided per unit weight (Wh/kg) and per unit volume (Wh/L) respectively. The theoretical specific energy density of  $\text{Li}_2\text{O}_2$  can be calculated based on the oxidation energy of pure lithium metal:<sup>13</sup>

$$\text{Spec. } E. = \frac{U_0 \times F}{M_{\text{Li}}} = \frac{2.96\text{V} \times 96500\text{C/mol}}{3600\text{C/Ah} \times 6.941\text{g/mol}} = 11430\text{Wh/kg} \quad (\text{Eq. 1.6})$$

This theoretical energy density is based on the mass of Li only, and is comparable to that of gasoline, which is 13000 Wh/kg.

For gasoline used in automotive applications, due to the energy loss from tank to wheel, currently the usable energy density is around 1700 Wh/kg. For LAB, due to until now the technology is still under investigation and there are no realistic prototypes to rely on, we can only estimate its practical energy density based on the existing metal-air battery systems. For Zn-air battery, the average energy efficiency is 40%-50%, and LAB is supposed to have a much reduced efficiency due to the light weight of lithium. The adding of oxygen, electrolyte, packing and so on will surely lower the energy density of LAB. For example, if we include the mass of oxygen, its theoretical energy density will be reduced to the range of around 3500Wh/kg. However even by considering all the above factors, the advantage of using LAB for the application of long distance EVs is still very promising. A very safe estimating made by Peter G.

Bruce et al gave a practical energy density in the range of 500~900Wh/kg, which is at least 2~3 times greater than the current LIB, and can deliver a driving distance of more than 550km.<sup>8</sup>

### 1.1.2 Challenges and problems related to LAB

However, despite all these significant advantages and considerable research efforts devoted to the develop of LAB, there are still many severe technical and scientific challenges exist towards the practical application of LAB batteries.<sup>14,15</sup> Fig. 1.2 plots a typical charge-discharge curve for one aprotic rechargeable LAB battery cell.

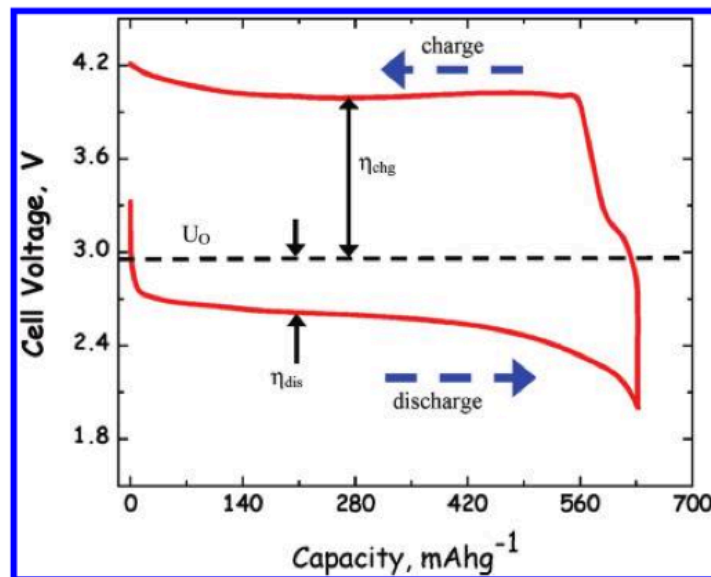


Fig. 1.2: A single measured charge-discharge curve for one aprotic rechargeable LAB battery cell at an operating current density of  $\sim 0.1$  mA/cm<sup>2</sup>.<sup>14</sup>

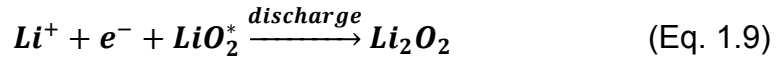
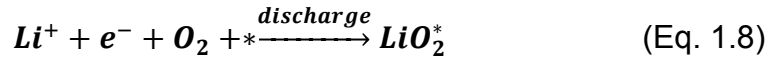
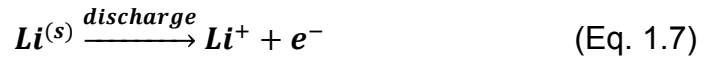
This curve shows the cell output voltage during discharge and the necessary applied voltage during recharge as a function of the cell capacity at a given current density. The capacity is calculated as the charge per unit weight of the cathode material.

From this curve we clearly see both the working voltages during discharge and charge are largely different from the thermodynamic potential of  $\text{Li}_2\text{O}_2$ .

The difference between working voltages and equilibrium potential is defined as the discharge and charge overpotential ( $\eta_{dis}$  and  $\eta_{chg}$ ) respectively. And the ratio between discharge and charge overpotential  $\eta_{dis}/\eta_{chg}$  is called the electrical energy efficiency. As the charge overpotential is much higher than the discharge one, the electrical energy efficiency is also greatly reduced. In addition, the cell capacity is also much lower than the theoretical value.

The high overpotential, low electronic energy efficiency, low rate capability as well as side reactions related to electrolyte decomposition and oxidation *etc* are all the key challenges that hinder the development of practical LAB.

The exploration of the origin of these existing problems suggests that except for O<sub>2</sub> mass transport, electron transport limitation is also a very important factor that determines the battery performance. A possible reaction path suggested by both experimental observations and theoretical calculations<sup>16</sup> is that during discharge Li<sub>2</sub>O<sub>2</sub> is formed on the surface of preformed Li<sub>2</sub>O<sub>2</sub> deposits, which can be described by the following reaction equations:



where \* denotes the surface position on Li<sub>2</sub>O<sub>2</sub>.

Based on this reaction scenario, the electron conductivity from the surface of electrode and that of Li<sub>2</sub>O<sub>2</sub> is essential to support the continuous growth of Li<sub>2</sub>O<sub>2</sub>. However previous literature study already demonstrated that bulk Li<sub>2</sub>O<sub>2</sub> is an insulator. As the discharge reaction proceeds Li<sub>2</sub>O<sub>2</sub> is formed on the surface of cathode, and once a Li<sub>2</sub>O<sub>2</sub> film layer fully covers the cathode surface, the poor conductivity of Li<sub>2</sub>O<sub>2</sub> becomes the rate limiting factor of the battery performance and finally lead to the death of the battery.

The first in situ TEM observation of the recharge process in LAB by Li Zhong et al found that the electron transport rather than the Li<sup>+</sup> transport within Li<sub>2</sub>O<sub>2</sub> is the limiting factor of the oxidation of Li<sub>2</sub>O<sub>2</sub> particles (see Fig. 1.3).<sup>17</sup>

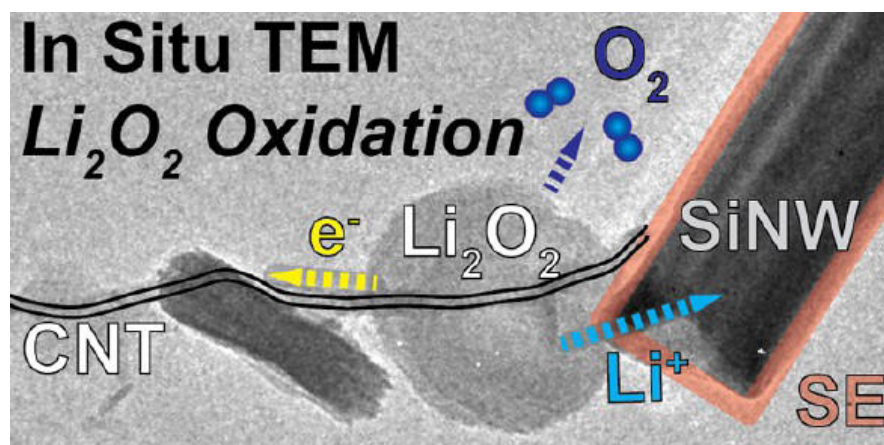


Fig. 1.3: In situ TEM observation of the electron and  $\text{Li}^+$  transport processes during oxidation of  $\text{Li}_2\text{O}_2$  particles at recharge.

Inspired by the above conclusions, not only an experimental design of porous electrode with large surface area and high electronic conductivity is desirable, but also the theoretical investigation of charge transport mechanism within  $\text{Li}_2\text{O}_2$  is also important.

### 1.1.3 Literature review about the charge transport mechanism of $\text{Li}_2\text{O}_2$

Unit now direct experiment measures regarding the conductivity of  $\text{Li}_2\text{O}_2$  are still quite limited. The first experimental measurement was given in last year, and the electronic and ionic transport in  $\text{Li}_2\text{O}_2$  was determined by ac impedance spectroscopy and dc conductivity measurements.<sup>18</sup>

The major transport mechanism was demonstrated to be ionic conductivity, with perceptible electronic contribution. The conductivities measured for ion and electron are in the order of  $10^{-10}$ - $10^{-9}$  S/cm and  $10^{-12}$ - $10^{-11}$  S/cm respectively. Another very recent paper in this year investigated the ionic transport in nanocrystalline  $\text{Li}_2\text{O}_2$  by conductivity and temperature variable  $^7\text{Li}$  NMR spectroscopy.<sup>19</sup> Consistent results with the above experiment were found in this study for the conductivity of microcrystalline  $\text{Li}_2\text{O}_2$ , that the overall conductivity is very low. And both the short-range and long-range Li ion transport was probed for the high energy ball milling  $\text{Li}_2\text{O}_2$ .

Both of these two experiments provide important information about the charge

transfer mechanism in  $\text{Li}_2\text{O}_2$ . However due to the fact that, both of the  $\text{Li}_2\text{O}_2$  materials measured in these experiments are subjected to various types of defects and impurities, which are uncontrollable by experimental processes. For a more detailed understanding of the effects of different charge transport mechanisms in  $\text{Li}_2\text{O}_2$ , theoretical investigation is quite necessary.

In contract to the very few experimental measurements, there have been different theoretical proposes for the conducting mechanism in  $\text{Li}_2\text{O}_2$ . Prior theoretical works have discussed several charge transfer mechanisms that might contribute to the conductivity of  $\text{Li}_2\text{O}_2$ .

V. Viswanathan et al pointed out a critical thickness of  $\text{Li}_2\text{O}_2$  film for electron tunneling to be around 5~10nm, over which the insufficient of electron tunneling within  $\text{Li}_2\text{O}_2$  would lead to the sudden death of the battery cell based on a dense thin film model.<sup>20</sup> Even though other calculations also demonstrated the metallic property of  $\text{Li}_2\text{O}_2$  surface,<sup>4</sup> the grain boundaries induced conductivity,<sup>21</sup> as well as the conducting interface states between  $\text{Li}_2\text{O}_2$  and cathode substrate( including carbon, gold *etc.*),<sup>22,23</sup> with the increase in particle size and film thickness, charge transport within bulk  $\text{Li}_2\text{O}_2$  is still essential. All the above mechanisms would only take effect within a limited depth, which is not sufficient to explain the experimentally observed conductivity.

Some of the recent theoretical studies have proposed polaron hopping to account for charge transfer within  $\text{Li}_2\text{O}_2$ .<sup>24-27</sup> Electron or hole polaron is formed when an electron is injected or removed from stoichiometric  $\text{Li}_2\text{O}_2$ , then it is stabilized by the local lattice distortion, featured by an elongation or contraction of O-O bond length within an oxygen peroxide pair. Then the hopping of these small polarons between neighboring oxygen peroxide pairs are supposed to result in electron conductivity (See Fig. 1.4). And a more detailed study by using PBE+U recalculated the migration barrier for both polarons. The result show that for electron polaron, the barrier is more than 1eV, which is too high to happen, while for hole polaron, the barrier is around 0.4~0.5eV.<sup>26</sup> The calculated low hopping rate of polarons are corresponding to the low conductivity in  $\text{Li}_2\text{O}_2$ .

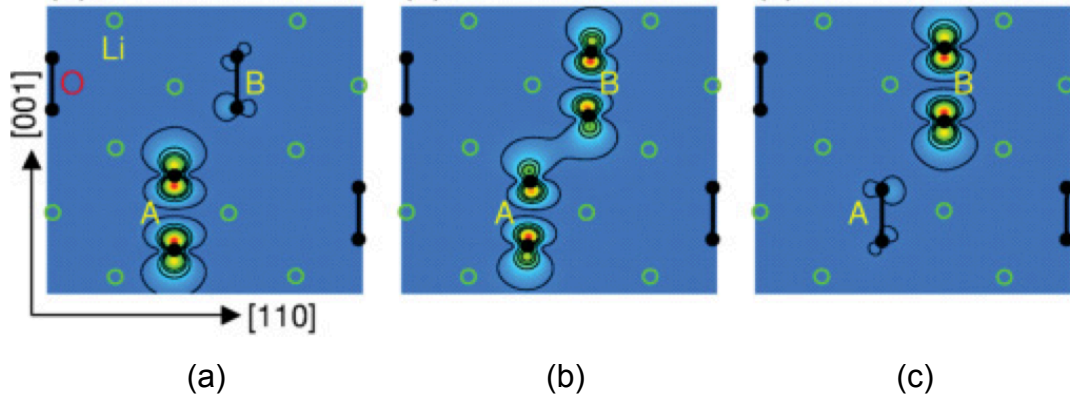


Fig. 1.4: Atomic structure and associated electron density distributions for interlayer electron polaron hopping.<sup>24</sup>

Regarding the ionic conductivity, recently there are two papers systematically investigated the native point defects in  $\text{Li}_2\text{O}_2$  to see their role in conductivity.<sup>28,29</sup> One of them calculated that both hole polaron and Li vacancy are relevant to the conductivity of  $\text{Li}_2\text{O}_2$ , and gave similar results to the experimental one.<sup>28,30</sup> However the other one argues that the existence of positively charged point defects will scatter the dominant hole tunneling.<sup>29</sup> In addition, Vladimir Timoshevskii et al. proposed an alternative way to dope  $\text{Li}_2\text{O}_2$  with Si impurity to improve its conductivity.<sup>31</sup> In their study they found substitution of Li with Si atom will lead to the formation of additional conducting states right above the valence band maximum (VBM), and the Si doped  $\text{Li}_2\text{O}_2$  is expected to have much improved electron mobility than stoichiometric  $\text{Li}_2\text{O}_2$ . Whereas, one previous papers has estimated that doping might not be a viable way to improve the conductivity due to the formation of localized polarons.<sup>26</sup>

## 1.2 Motivation and objectives

Based on the above background introduction and literature review, we know that the charge transport mechanism of  $\text{Li}_2\text{O}_2$  in LAB is one of the most important factors that determine the battery performance and the future development in LAB for long distance electric vehicles. However, despite the existing theoretical works regarding the conductivity of  $\text{Li}_2\text{O}_2$ , there is still not a well accepted theory about the conducting mechanism of  $\text{Li}_2\text{O}_2$ . And there

are even few direct experimental measurement about the conductivity. Thus this current Ph.D thesis study was motivated by the above consideration. We employed the first principles approach to investigate the charge transport mechanism of  $\text{Li}_2\text{O}_2$  as a discharge product of LAB. We focused on the defective and interfacial properties relevant to the conductivity of  $\text{Li}_2\text{O}_2$ .

The intrinsic and extrinsic defects including intended doping and hydrogen impurities were calculated in details. The Au and  $\text{Li}_2\text{O}_2$  interfacial properties in both the coherent and semicoherent configurations were evaluated. Finally the mechanism of the defect and interface induced conductivity in  $\text{Li}_2\text{O}_2$  is expected to be obtained.

**REFERENCES**

1. E. L. Littauer and K. C. Tsai, *J. Electrochem. Soc.*, 1976, **123**, 771–776.
2. E. L. Littauer and K. C. Tsai, *J. Electrochem. Soc.*, 1976, **123**, 964–969.
3. K. M. Abraham and Z. Jiang, *J. Electrochem. Soc.*, 1996, **143**, 1–5.
4. M. D. Radin, F. Tian, and D. J. Siegel, *J Mater Sci*, 2012, **47**, 7564–7570.
5. T. Ogasawara, A. Débart, M. Holzapfel, P. Novák, and P. G. Bruce, *J. Am. Chem. Soc.*, 2006, **128**, 1390–1393.
6. J. Read, *J. Electrochem. Soc.*, 2002, **149**, A1190–A1195.
7. Y.-C. Lu, H. A. Gasteiger, M. C. Parent, V. Chiloyan, and Y. Shao-Horn, *Electrochem. Solid-State Lett.*, 2010, **13**, A69–A72.
8. P. G. Bruce, S. A. Freunberger, L. J. Hardwick, and J.-M. Tarascon, *Nat Mater*, 2011, **11**, 19–29.
9. M. D. Radin, J. F. Rodriguez, F. Tian, and D. J. Siegel, *J. Am. Chem. Soc.*, 2012, **134**, 1093–1103.
10. C. MW Jr, *Sign in - Google Accounts*, J. Phys. Chem. Ref. Data. Monograph, 1998.
11. J. S. Hummelshøj, J. Blomqvist, S. Datta, T. Vegge, J. Rossmeisl, K. S. Thygesen, A. C. Luntz, K. W. Jacobsen, and J. K. Nørskov, *J. Chem. Phys.*, 2010, **132**, 071101.
12. Y.-C. Lu, H. A. Gasteiger, E. Crumlin, R. McGuire, and Y. Shao-Horn, *J. Electrochem. Soc.*, 2010, **157**, A1016–A1025.
13. C.-X. Zu and H. Li, *Energy Environ. Sci.*, 2011, **4**, 2614–2624.
14. G. Girishkumar, B. McCloskey, A. C. Luntz, S. Swanson, and W. Wilcke, *J. Phys. Chem. Lett.*, 2010, **1**, 2193–2203.
15. J. Christensen, P. Albertus, R. S. Sanchez-Carrera, T. Lohmann, B. Kozinsky, R. Liedtke, J. Ahmed, and A. Kojic, *J. Electrochem. Soc.*, 2012, **159**, R1–R30.
16. J. S. Hummelshøj, J. Blomqvist, S. Datta, T. Vegge, J. Rossmeisl, K. S. Thygesen, A. C. Luntz, K. W. Jacobsen, and J. K. Nørskov, *J. Chem. Phys.*, 2010, **132**, 071101.
17. L. Zhong, R. R. Mitchell, Y. Liu, B. M. Gallant, C. V. Thompson, J. Y.



- Huang, S. X. Mao, and Y. Shao-Horn, *Nano Lett.*, 2013, **13**, 2209–2214.
18. O. Gerbig, R. Merkle, and J. Maier, *Advanced Materials*, 2013, **25**, 3129–3133.
19. A. Dunst, V. Epp, I. Hanzu, S. A. Freunberger, and M. Wilkening, *Energy Environ. Sci.*, 2014, **7**, 2739–2752.
20. V. Viswanathan, K. S. Thygesen, J. S. Hummelshøj, J. K. Nørskov, G. Girishkumar, B. D. McCloskey, and A. C. Luntz, 2011, **135**, 214704.
21. W. T. Geng, B. L. He, and T. Ohno, *J. Phys. Chem. C*, 2013, **117**, 25222–25228.
22. Y. Zhao, C. Ban, J. Kang, S. Santhanagopalan, G.-H. Kim, S.-H. Wei, and A. C. Dillon, *Appl. Phys. Lett.*, 2012, **101**, 023903.
23. J. Chen, J. S. Hummelshøj, K. S. Thygesen, J. S. G. Myrdal, J. K. Nørskov, and T. Vegge, *Catalysis Today*, 2011, **165**, 2–9.
24. J. Kang, Y. S. Jung, S.-H. Wei, and A. C. Dillon, *Phys. Rev. B*, 2012, **85**, 035210.
25. S. P. Ong, Y. Mo, and G. Ceder, *Phys. Rev. B*, 2012, **85**, 081105.
26. J. M. Garcia-Lastra, J. S. G. Myrdal, R. Christensen, K. S. Thygesen, and T. Vegge, *J. Phys. Chem. C*, 2013, **117**, 5568–5577.
27. A. C. Luntz, V. Viswanathan, J. Voss, J. B. Varley, J. K. Nørskov, R. Scheffler, and A. Speidel, *J. Phys. Chem. Lett.*, 2013, **4**, 3494–3499.
28. M. D. Radin and D. J. Siegel, *Energy Environ. Sci.*, 2013, **6**, 2370–2379.
29. J. B. Varley, V. Viswanathan, J. K. Nørskov, and A. C. Luntz, *Energy Environ. Sci.*, 2014, **7**, 720.
30. O. Gerbig, R. Merkle, and J. Maier, *Advanced Materials*, 2013, **25**, 3129–3133.
31. V. Timoshevskii, Z. Feng, K. H. Bevan, J. Goodenough, and K. Zaghib, *Appl. Phys. Lett.*, 2013, **103**.



## Chapter 2 Theoretical background

### 2.1 Introduction

Physical problems related to condensed matter systems are ultimately the many body problems. The emergence of quantum mechanics in the early 1900s provides a key solution to the many-body problem. Then with the progress in computational hardware, computational physics also experienced a rapidly development. Nowadays, first principles calculations have been proved to be a very successful method to study the geometric, energetic, electronic and many other properties of materials. The concept of ‘first principles’ means the calculations are started directly from the basic established theories, without any empirical model or fitting parameters. As a complement to experimental studies, first principles calculations provide an approach to understand the physical mechanisms of elemental components. And they can also reach the fields where direct experimental measurements are difficult.

Nevertheless, the main challenges for the modern computational methods to describe the electronic properties of condensed matter are the accurate solution of the underlying many-body problem and the treatment of electron exchange and correlation. Now the density functional theory (DFT) <sup>1,2</sup> and Hedin’s GW approximation (GWA) are demonstrated to be the most successful approaches to treat the ground state and excited state of many-body systems respectively.

In this chapter, we present a brief overview of the theoretical background related to the calculations in this thesis.

### 2.2 Ground state properties

#### 2.2.1 Many-body problem

In quantum mechanisms, the main task is to solve the many-body problem,

alternatively speaking, the electronic structure of the system. Since electron is considered as one wavefunction, all the properties of a given system can be obtained from their wavefunction. The time independent electronic structure can be solved by Schrödinger equation:

$$\hat{H}\Psi = E\Psi \quad (\text{Eq. 2.1})$$

$\hat{H}$  is the Hamiltonian and  $E$  is the eigenvalue of the system. The Hamiltonian is determined by the following formula:

$$\hat{H} = -\frac{\hbar^2}{2m_e} \sum_i \nabla_i^2 - \sum_{i,I} \frac{Z_I e^2}{|r_i - R_I|} + \frac{1}{2} \sum_{i \neq j} \frac{e^2}{|r_i - r_j|} - \sum_I \frac{\hbar^2}{2M_I} \nabla_I^2 + \frac{1}{2} \sum_{I \neq J} \frac{Z_I Z_J e^2}{|R_I - R_J|} \quad (\text{Eq. 2.2})$$

where, the kinetic energies of electron and nuclei are the first and fourth term respectively, the repulsion between electron-electron and nuclei-nuclei are the third and fifth term respectively, and the second term is the attraction between electron-nuclei. In the solid material, the number of electron and nuclei is in the order of  $10^{23}$ , exact solution of Hamiltonian is impossible. Approximations are needed to solve the above equation.

Then the Born-Oppenheimer approximation<sup>3</sup> was proposed in 1927, and it states that the kinetic part of nuclei can be omitted from the above Hamiltonian, given the fact that nuclei move much slower than electrons.<sup>4</sup> The new expression of Hamiltonian becomes:

$$\hat{H} = -\frac{\hbar^2}{2m_e} \sum_i \nabla_i^2 + \frac{1}{2} \sum_{i \neq j} \frac{e^2}{|r_i - r_j|} + V_{R\alpha}^{ext}(r_i) \quad (\text{Eq. 2.3})$$

where,  $V_{R\alpha}^{ext}(r_i)$  is the external potential for electrons. However the resulted Hamiltonian is still impossible to solve exactly. Further approximations are necessary.

### 2.2.2 Density function theory (DFT)

Density function theory (DFT) based on W. Kohn theorems<sup>5</sup> is the simplest

and most effective quantum mechanical modeling methods available in physics and chemistry now. It is used to describe the ground state electronic structure of many-body systems, based on the main idea that the properties of many-body system can be determined via its spatially dependent electron density (namely through the functional of the electron density), instead of many-body wave function, which is the starting point of classical methods for electron structure calculation. Now the DFT method has been widely used in condensed states physics, computational quantum chemistry and computational materials science.

#### *2.2.2.1 Thomas-Fermi-Dirac approximation*

Other than the Hartree-Fock method, which uses the wave function as the basic variable of a system, Thomas and Fermi first proposed that charge density uniquely determines the energy of a many-body system in 1920s, setting up the conceptual roots of modern DFT. As a make up for the lack of exchange and correlation effects in the Thomas-Fermi model, Dirac introduced exchange phenomena to this model under the local approximation condition. The resulting Thomas-Fermi-Dirac approximation gives a relatively simple solving approach compared with the Schrödinger equations, but it is still too simple to give an accurate result due to its neglecting of electron correlation effects.

#### *2.2.2.2 Hohenberg-Kohn theorem*

The situation changed dramatically as the appearance of a more exact proposal and prove given by Hohenberg and Kohn in 1960s, that the ground state properties of a non-degenerate many-body system is determined by its ground state charge density, the so called Hohenberg-Kohn theorems, which put the DFT on a firm theoretical footing. The two theorems included are stated as bellow:

**(1) Under a given external potential, the ground state properties of an interacting many-body system is uniquely determined by the non-degenerate ground state electron density that depends only on three spatial coordinates.**

A proof of this theorem is given as that under a given external potential, the Hamiltonian of the system is determined, thus in principle the ground state wave function is also determined; once the wave function is known, we can further get all the properties of the system. Since ground state electron density is also uniquely determined by the external potential, the above conclusion can be expressed as that once the ground state electron density is known, all the properties of the system are determined, which means the properties are functional of the electron density. The theorem can also be demonstrated in another way that the electron density determines the positions and charges of the nuclei and thus determines the Hamiltonian.

The ground state energy of the system has the form:

$$\begin{aligned}
 E[n] &= \langle \Psi[n] | T + V_{ee} + V_{ext} | \Psi[n] \rangle \\
 &= T[n] + V_{ee}[n] + \int d^3r V_{ext}(r) n(r) \\
 &= F[n]_{HK} + \int d^3r V_{ext}(r) n(r)
 \end{aligned} \tag{Eq. 2.4}$$

where,  $n(r)$  is the ground state electron density,  $V_{ext}$  is the external potential,  $\Psi[n]$  is the ground state wave function,  $T$  is ground state kinetic energy and  $V_{ee}$  is the electron interaction energy.  $V_{ee}$  consists of the classical Coulomb interaction and non-classical electron interactions, including correction to self-interaction, exchange interaction and correlation interaction  $E_{xc}^{GGA}$ . In this expression, only  $F[n]_{HK}$  is a functional of the ground state electron density.

**(2) The energy functional for the system has its minimum at the correct ground state electron density, and this minimum energy is the corresponding ground state energy.**

The second theorem provides us a way to estimate the ground state electron

density, and this can be done through the variational method as bellow:

$$\langle \tilde{\Psi} | H | \tilde{\Psi} \rangle = T[\tilde{n}] + E_{ext}[\tilde{n}] + E_{ee}[\tilde{n}] = E[\tilde{n}] \geq E_0[n_0] = \langle \Psi_0 | H | \Psi_0 \rangle \quad (\text{Eq. 2.5})$$

where,  $n_0$  is the ground state electron density. Only when  $n = n_0$ ,  $E[n]$  reaches its minimum value.

### 2.2.2.3 Kohn-Sham equation

In principle, the ground state electron density and energy can be solved according to Hohenberg-Kohn theorems by minimizing one of the system's universal functional, however this method can not be practically realized due to a lack of the exact form of kinetic and electron-electron interaction functional. Kohn and Sham proposed an approximating approach to solve the ground state electron density in 1965. Within their framework, a fictitious non-interacting electron system with the same charge density as the real system was introduced to replace the intractable interacting electrons. The Hamiltonian of the non-interacting system can be expressed as the sum of the kinetic energy and an effective local potential acting on electrons.

$$H_{aux} = -\frac{1}{2} \sum_{\sigma,i}^{N^\sigma} \nabla_i^2 + \sum_{\sigma,i}^{N^\sigma} \nabla_{eff}^\sigma \quad (\text{Eq. 2.6})$$

The wave function can be determined by the Slater determinant:

$$\Theta_{aux} = \frac{1}{\sqrt{N!}} \begin{vmatrix} \Psi_1^\sigma(r_1) & \Psi_2^\sigma(r_1) & \Psi_3^\sigma(r_1) & \Psi_4^\sigma(r_1) \\ \Psi_1^\sigma(r_2) & \Psi_2^\sigma(r_2) & \Psi_3^\sigma(r_2) & \Psi_4^\sigma(r_2) \\ \vdots & \vdots & \vdots & \vdots \\ \Psi_1^\sigma(r_N) & \Psi_2^\sigma(r_N) & \Psi_3^\sigma(r_N) & \Psi_4^\sigma(r_N) \end{vmatrix} \quad (\text{Eq. 2.7})$$

where,  $\sigma$  is the spin state of electrons and  $\Psi_i^\sigma(r_n)$  is the eigenfunction of the system. The electron density can be obtained from:

$$n(r) = \sum_{\sigma,i}^{N^\sigma} |\Psi_i^\sigma(r)|^2 \quad (\text{Eq. 2.8})$$

The kinetic energy can be expressed as:

$$T_S = -\frac{1}{2} \sum_{\sigma,i}^{N_\sigma} \langle \Psi_i^\sigma | \nabla^2 | \Psi_i^\sigma \rangle = -\frac{1}{2} \sum_{\sigma,i}^{N_\sigma} |\nabla \Psi_i^\sigma|^2 \quad (\text{Eq. 2.9})$$

and the Coulomb interaction of the electron-electron interaction has the form:

$$J[n] = \frac{1}{2} \int d^3r d^3r' \frac{n(r)n(r')}{|r-r'|} \quad (\text{Eq. 2.10})$$

So the total energy of the system can be rewritten as:

$$E_{KS} = T_S[n] + \int d^3r V_{ext}(r)n(r) + J[n] + E_{XC}[n] \quad (\text{Eq. 2.11})$$

where  $E_{XC}[n]$  is the exchange-correlation function and includes the following items:

$$E_{XC} = F_{HK}[n] - (T_S[n] + J[n]) = \langle T \rangle - T_S[n] + \langle V_{ee} \rangle - J[n] = T_C[n] + E_{ncl}[n] \quad (\text{Eq. 2.12})$$

$T_C[n]$  stands for the error caused by using the non-interacting kinetic energy and  $E_{ncl}[n]$  stands for that caused by treating the electron-electron interaction classically. By using the eigenfunction of the system, the energy can be rewritten into another format:

$$\begin{aligned} E[n] = & -\frac{1}{2} \sum_{\sigma,i}^{N_\sigma} \langle \Psi_i^\sigma(r) | \nabla_i^2 | \Psi_i^\sigma(r) \rangle + \frac{1}{2} \sum_{\sigma,i}^{N_\sigma} \sum_{\sigma,i}^{N_\sigma} \int \int d^3r d^3r' |\Psi_i^\sigma(r_i)|^2 \frac{1}{r_{12}} |\Psi_i^\sigma(r_i)|^2 + \\ & E_{XC}[n] - \sum_{\sigma,i}^{N_\sigma} \int d^3r_1 \sum_A^M \frac{Z_A}{r_{1A}} |\Psi_i^\sigma(r_1)|^2 \end{aligned} \quad (\text{Eq. 2.13})$$

Applying the variational theorem combining with the orthogonal restrictions of eigenfunctions, we can deduce the energy into the following format:

$$\left( -\frac{1}{2} \nabla_i^2 + \left[ \int d^3r_2 \frac{n(r_2)}{r_{12}} + V_{xc}(r_1) - \sum_A^M \frac{Z_A}{r_{1A}} \right] \right) \Psi_i^\sigma = \left( -\frac{1}{2} \nabla_i^2 + V_{eff}(r_1) \right) \Psi_i^\sigma = \varepsilon_i \Psi_i^\sigma$$



(Eq. 2.14)

$$V_{eff} \equiv V_{ext}(r) + \frac{\delta J_{Hartree}}{\delta n(r,\sigma)} + \frac{E_{xc}}{\delta n(r,\sigma)} = V_{ext}(r) + V_{Hartree}(r) + V_{xc}^\sigma(r) \quad (\text{Eq. 2.15})$$

where  $V_{xc}$  is the functional derivative of  $E_{xc}$  with respect to  $n$ ,

$$V_{xc} \equiv \frac{\delta E_{xc}}{\delta n(r,\sigma)} = \varepsilon_{xc}([n], r) + n(r) \frac{\delta \varepsilon_{xc}([n], r)}{\delta n(r,\sigma)} \quad (\text{Eq. 2.16})$$

Until now, we have obtained the Kohn-Sham equation for the non-interacting electrons system in an effective local potential. If the exact  $V_{xc}$  format is known, we can get the exact ground state density and energy. However, in the real case, the exchange-correlation interactions are usually unknown, appropriate approximations of the exchange-correlation potential are necessary for the practical application of DFT.

### 2.2.3 Exchange-correlation approximations

#### 2.2.3.1 Local density approximation (LDA)

LDA is the most commonly used approximation and also the basis of all approximate exchange-correlation functional. Its central idea is that the local exchange-correlation energy of an inhomogeneous system can be approximated by that of a homogeneous electron gas with the same local electron density at this particular local point. Later the up and down electron spins are introduced to a modified version, the local spin-density approximation (LSDA).

$$E_{xc}^{LDA}(n^\uparrow, n^\downarrow) = \int d^3r n(r) \varepsilon_{xc}^{homo}(n^\uparrow(r), n^\downarrow(r)) = \int d^3r n(r) [\varepsilon_x^{homo}(n^\uparrow(r), n^\downarrow(r)) + \varepsilon_c^{homo}(n^\uparrow(r), n^\downarrow(r))] \quad (\text{Eq. 2.17})$$

where,  $n^\uparrow(r)$  and  $n^\downarrow(r)$  are the densities of spin-up and spin-down electrons. The exchange energy  $\varepsilon_x^{homo}(n^\uparrow(r), n^\downarrow(r))$  can be obtained from the Hartree-Fock approximation, while the correlation energy  $\varepsilon_c^{homo}(n^\uparrow(r), n^\downarrow(r))$  can

reach a high accuracy by the Monte Carlo method.

Homogeneous electron gas is the system where electrons are subjected to a constant external positive potential with a constant charge density, and it is the only system that we can get near exact results of the exchange-correlation energy. Under the Hartree-Fock approximation, the eigenfunctions are plane waves  $\Psi_k(r) = \frac{1}{\sqrt{\Omega}} e^{ikr}$ , and the exchange energy has its analytic form:

$$\varepsilon_x^\sigma = \frac{E_x^\sigma}{N^\sigma} = -\frac{3}{4\pi} \kappa_F^\sigma = -\frac{3}{4} \left( \frac{6}{\pi} n^\sigma \right)^{1/3} \quad (\text{Eq. 2.18})$$

where,  $\sigma$  is the spin of electrons. The functional of the correlation energy is unknown, but can get essentially exact result by the numerical quantum Monte Carlo calculation, one of the most widely used form, among which we have the VWN approximation proposed by Vosko, Wilkers and Nussair in 1980s.

Since the idea of LDA is based on the consideration that in a system with a slowly changing electron density the exchange-correlation potential is comparable with that of a homogeneous electron gas, it works well in the electron systems with relatively uniform distributions like in solids, but usually fails in atoms and molecules, which have strongly changing charge densities.

### 2.2.3.2 Generalized gradient approximation (GGA)

GGA is the first and natural progression beyond LDA, since it also includes the gradient of the charge density instead of only the density at a particular point in the LDA, in order to account for the non-homogeneous of the true system. Under this approximation, the exchange-correlation energy is the functional of both the electron density and its gradient, and has its form like:

$$E_{xc}^{GGA}(n^\uparrow, n^\downarrow) = \int d^3r n(r) \varepsilon_{xc}(n^\uparrow, n^\downarrow, \nabla n^\uparrow, \nabla n^\downarrow) = E_x^{GGA} + E_c^{GGA} \quad (\text{Eq. 2.19})$$

Many approximations have been made to simulate the exchange energy  $E_x^{GGA}$  and correlation energy  $E_c^{GGA}$  respectively, like the PW91 potential, Perdew-

Burke-Ernzerhof (PBE) potential<sup>6</sup> etc., and different combination of the exchange and correlation can be used. And GGA-PBE is now the simplest and most widely used form.

### 2.2.3.3 Hybrid functional

Due to the problems related with LDA, GGA and PBE functionals, in which the *d* and *f* electrons cannot be treated properly, hybrid exchange-correlation functional has been proposed. Now It has become a very successful approximation for chemical applications, especially for defect calculation. It has the form as bellow:

$$E_{xc}^{HYB} = (1 - \lambda)E_x^{KS} + \lambda E_{xc}^{GGA} \quad (\text{Eq. 2.20})$$

where  $E_x^{KS}$  is the exchange energy of a non-interacting system calculated with the exact Khon-Sham wavefunction, and  $E_{xc}^{GGA}$  is an approximate exchange-correlation energy got from GGA.  $\lambda$  is a coupling constant ranging from 0 to 1: when  $\lambda=0$ , it stands for the non-interacting system, while when  $\lambda=1$ , it's the real interacting system. And this functional has some very accurate forms like B3PW91<sup>7</sup> and B3LYP, which have the follow two forms respectively.

$$E_{xc}^{HYB} = E_{xc}^{LDA} + a(E_{xc}^{\lambda=0} - E_x^{LDA}) + bE_x^B + cE_c^{PW91} \quad (\text{Eq. 2.21})$$

$$E_{xc}^{B3LYP} = (1 - a)E_x^{LDA} + aE_{xc}^{\lambda=0} + bE_x^{B88} + cE_c^{LYP} + (1 - c)E_c^{LDA} \quad (\text{Eq. 2.22})$$

Besides, the Heyd-Scuseria-Ernzerhof (HSE06) hybrid functional<sup>7-9</sup> has also been widely used especially for defect calculations.

## 2.3 Excited state properties

Despite the great success of DFT, there is a well known failure that it's unable

to describe the excited states correctly. Bandgap between the occupied and empty states is significantly underestimated in the framework of DFT. The reason is due to the fact that excitation process will disturb the system by changing the electron density, while in DFT the eigenvalues and excitations energies are determined by the static charge density. The redistribution of electrons can be treated by the many-body perturbation theory, thus an accurate numerical modeling of theoretical quasiparticle bandstructures can be obtained.

### 2.3.1 GW approximation

Now the most successful method used to compute the electronic excited-state properties is based on the GW approximation,<sup>10-12</sup> where G means the Green's function of the system and W denotes the screened Coulomb interaction accounting for both the bare Coulomb interaction and the response to an excitation. This approximation is aimed to calculate the self-energy of a many-body systems of electrons. The self-energy can be expressed in a formal Taylor series in the powers of screened Coulomb interaction:

$$\Sigma = iGW - GWGWG + \dots \quad (\text{Eq. 2.23})$$

In GW approximation, the self-energy is evaluated by only the first term:

$$\Sigma \approx iGW \quad (\text{Eq. 2.24})$$

#### 2.3.1.1 Green's function

The many-body properties of excited state for a system can be approximated by the property of quasiparticles. The concept of quasiparticle describes the bare electron and its positive screening charge surrounded due to other electrons. The properties of quasiparticle can be evaluated by the single-particle Green's function. In equilibrium system, there are different kinds of definitions for the Green's function. The time-ordered Green's function is defined as:

$$\begin{aligned}
 G(r, t, r', t') &= -i \langle \Psi_0 | \hat{T} [\hat{\psi}(r, t) \hat{\psi}^\dagger(r', t')] | \Psi_0 \rangle \\
 &= \begin{cases} -i \langle \Psi_0 | \hat{\psi}(r, t) \hat{\psi}^\dagger(r', t') | \Psi_0 \rangle, & t > t' \\ i \langle \Psi_0 | \hat{\psi}(r, t) \hat{\psi}^\dagger(r', t') | \Psi_0 \rangle, & t' > t \end{cases} \quad (\text{Eq. 2.25})
 \end{aligned}$$

where,  $|\Psi_0\rangle$  is the ground state of Hamiltonian,  $\hat{T}$  is the Wick time-ordering operator,  $\hat{\psi}(r, t)$  and  $\hat{\psi}^\dagger(r', t')$  are the Fermion annihilation operator and corresponding creation operator respectively.

$$\hat{\psi}(r, t) = \exp(i\hat{H}t) \hat{\psi}(r) \exp(-i\hat{H}t) \quad (\text{Eq. 2.26})$$

The definition expresses the propagation of particles. It gives the probability to find the particle at time  $t$  and position  $r$ .

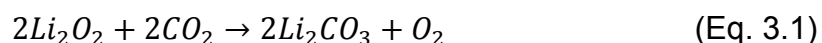
## REFERENCES

1. P. Hohenberg and W. Kohn, *Phys. Rev.*, 1964, **136**, 864–871.
2. W. Kohn and L. J. Sham, *Phys. Rev.*, 1965, **140**, 1133–1138.
3. M. Born and J. R. Oppenheimer, *Ann. Phys.*, 1927, **389**, 457–484.
4. M. Born and R. Oppenheimer, *Ann. Phys.*, 1927, **84**, 457.
5. P. Hohenberg and W. Kohn, *Physical review*, 1964, **136**, 1–8.
6. J. P. Perdew, K. Burke, and M. Ernzerhof, *Phys. Rev. Lett.*, 1996, **77**, 3865–3868.
7. A. D. Becke, *J. Chem. Phys.*, 1993, **98**, 5648.
8. J. Heyd, G. E. Scuseria, and M. Ernzerhof, *J. Chem. Phys.*, 2003, **118**, 8207.
9. A. V. Krukau, O. A. Vydrov, A. F. Izmaylov, and G. E. Scuseria, *J. Chem. Phys.*, 2006, **125**, 224106.
10. M. Shishkin and G. Kresse, *Phys. Rev. B*, 2006, **74**, 035101.
11. M. Shishkin, M. Marsman, and G. Kresse, *Phys. Rev. Lett.*, 2007, **99**, 246403.
12. M. Shishkin and G. Kresse, *Phys. Rev. B*, 2007, **75**, 235102.

## Chapter 3 Bulk properties of Li<sub>2</sub>O<sub>2</sub>

### 3.1 Introduction

Li<sub>2</sub>O<sub>2</sub> has been used as a breathable atmospheres regenerator in spacecraft through the reaction with CO<sub>2</sub> to generate O<sub>2</sub>, benefiting from its light weight:



Now due to the reverse formation and decomposition of Li<sub>2</sub>O<sub>2</sub> in LAB, its has drawn lots of research interests as a discharge product in LAB.

The crystal structure of lithium peroxide was first determined to be in the hexagonal  $P\bar{6}$  space group by experiments using X-ray diffraction in 1950s.<sup>1,2</sup> However due to the fact that lithium is a poor X-ray scatter, the available experimental datas show ambiguous results. Then in 2005, theoretical DFT calculation by Cota and Mora further optimized the structure and a more symmetrical  $P6_3/mmc$  hexagonal crystal structure was proposed together with improved lattice parameters.<sup>3</sup>

Previous electronic properties calculations show that bulk Li<sub>2</sub>O<sub>2</sub> is an insulator,<sup>4</sup> however no experimental measurement of the bandgap value is available until now. Different calculation techniques have been used in the literature studies to predict its bandgap.

In this part of the thesis, as a benchmark calculation, we started from the crystal structure of Li<sub>2</sub>O<sub>2</sub>, following by its electronic structure, especially the evaluation of bulk bandgap. A detailed comparison of the bandgap calculation using different computational methods was carried out, including the standard DFT methods, the hybrid DFT methods as well as the many-body GW approximation.<sup>5-7</sup>

### 3.2 Calculation methods

In this part of calculation,

## 1) For structure optimization:

Both Perdew–Burke–Ernzerhof (PBE) generalized gradient approximation (GGA),<sup>8</sup> and Heyd-Scuseria-Ernzerhof (HSE06) hybrid functional<sup>9,10</sup> were used. Full relaxation of shape, volume and atomic positions of the hexagonal conventional unit cell was performed until the energy difference is less than  $10^{-6}$  eV and force tolerance is within 0.01 eV/Å. Electron occupancies were determined with a Gaussian smearing of width 0.05 eV, and a  $10 \times 10 \times 4$   $\Gamma$ -centered k-point sampling was used. Non-spin polarized calculations were performed for the bulk properties due to  $\text{Li}_2\text{O}_2$  is known to be non-magnetic, and our calculation also showed the magnetic moment is zero if calculated.

## 2) For electronic structure calculation:

Different calculation techniques including the GGA-PBE, HSE06, and many-body GW approximation were used. The GW approximation was performed in the GW0 level with both GGA and HSE06 wavefunction as the starting point. The following shows the calculation procedure for HSE-GW0 calculation. For PBE density of states (DOS) calculation, the tetrahedron method with Blöchl corrections and a  $20 \times 20 \times 8$   $\Gamma$ -centered k-point mesh were used, while HSE06 and GW0 calculation were performed with Gaussian smearing of width 0.05 eV, and a  $10 \times 10 \times 4$   $\Gamma$ -centered k-point sampling. Convergence tests of GW0 approximation with respect to the number of bands were performed to make sure both the calculated bandgap and band edges are well converged. Then as a common practice, the fraction of the exact exchange in HSE functionals is optimized to reproduce the GW-based bandgap.

## 3) For GW calculation:

Different levels of approximation can be performed, including the non-self-consistent/one-shot G0W0, partially self-consistent GW0 with updating of the eigenvalues in the Green's function G only, as well as the self-consistent GW with an update in both the Green's function and the dielectric matrix of the screened potential W. Previous theoretical studies have demonstrated that the trend of the G0W0 approximation is to underestimate the band gaps, while scGW is tend to overestimate. The partially self-consistent GW0 approximation usually gives a better agreement with experimental results,<sup>7</sup>



and is proved to be an efficient method for predicting quasi-particle energies in simple  $sp$ -bonded systems. Besides the different levels of approximation, another important factor that affects the result is the starting point of the GW approximation.<sup>11</sup> Therefore we carried out our GW approximation in the GW0 level based on both GGA and HSE06 wavefunction in order to give a better evaluation of  $\text{Li}_2\text{O}_2$  bandgap.

Procedure for HSE-GW0 bandgap calculation:

- 1) *Standard PBE-GGA calculation to obtain DFT wavefunctions;*
- 2) *Hybrid HSE06 calculation based on preconverged GGA wavefunction with few unoccupied orbitals to obtain HSE06 wavefunctions as an initial step;*
- 3) *DFT virtual band calculation with a large number of unoccupied orbitals to obtain wavefunctions (WAVECAR) and derivative of orbitals (WAVEDER);*
- 4) *GW0 calculation based on the above WAVECAR and WAVEDER files.*

### 3.3 Results and discussion

#### 3.3.1 Crystal structure

##### 3.3.1.1 Symmetric analysis of atomic positions in $\text{Li}_2\text{O}_2$

Fig. 3.1 shows the (a) unit cell and (b)  $2 \times 2$  supercell of  $\text{Li}_2\text{O}_2$ .  $\text{Li}_2\text{O}_2$  crystallizes in  $P6_3/mmc$  space group, and its structure consists of alternating layers of  $\text{LiO}_2^-$  and  $\text{Li}^+$ . The O-O species exists in the form of covalently bonded  $\text{O}_2^{2-}$  dimers with the bonding length of  $\sim 1.5$  Å. The  $\text{O}_2^{2-}$  peroxide anions is surrounded by nine nearest  $\text{Li}^+$  cations. The  $\text{Li}^+$  cations located within one O-O layer and between two O-O layers can be categorized into two symmetric distinguish Li positions. The intra-layer  $\text{Li}^+$  cations, which locate at one half of the trigonal prism centers of O-O dimers, can be labeled as T-site Li, while the inter-layer  $\text{Li}^+$  cations, which locate at the octahedron centers of O-O dimers, is labeled at O-site Li. Next to Li-filled O-O octahedron there is another kind of empty O-O tetrahedrons, filling the spaces between O-O octahedrons (see Fig. 3.1).

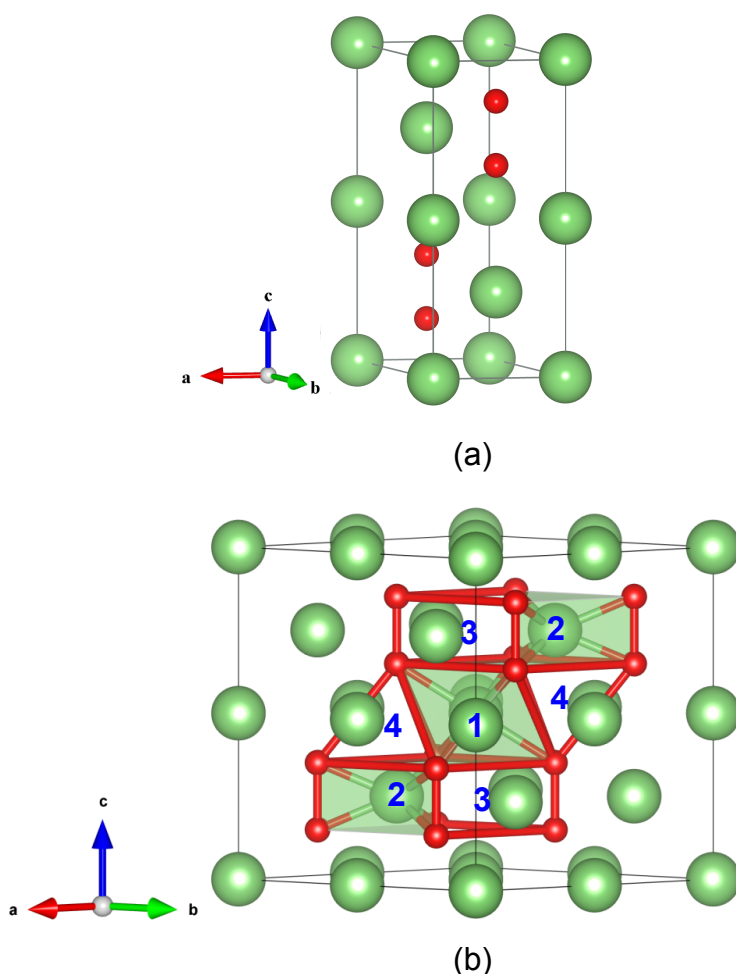


Fig. 3.1: Crystal structure of the (a) hexagonal unit cell and (b)  $2 \times 2$  supercell of  $\text{Li}_2\text{O}_2$ . The numbers indicate the different lattice sites. 1: Li octahedron site (Li-O). 2: Li trigonal prism site (Li-T). 3: Empty trigonal prism. 4: Empty tetrahedron.

### 3.3.1.2 Lattice constants

The calculated lattice constants are shown in Table 3.1. The results of PBE and HSE06 agree very well with experimental values and previous calculations ones. The lattice parameters optimized by HSE06 hybrid functional are  $a = 3.12 \text{ \AA}$  and  $c = 7.61 \text{ \AA}$ , with an O-O bonding length of  $1.50 \text{ \AA}$ . From our calculation, we also found there is  $\sim 1\%$  difference in the optimal lattice constants obtained from PBE and HSE06 structure optimization. This result is consistent with previous theoretical studies that GGA functional generally overestimates the equilibrium volume, whereas hybrid functional tends to give very good estimation of volume within 1% of the experimental data for most systems. A similar result has also been pointed out in the

previous calculations that increasing the mixing parameter  $\alpha$  in HSE calculation from 0.25 to 0.44 will cause <1% smaller of  $a$  and  $c$ .<sup>12</sup>

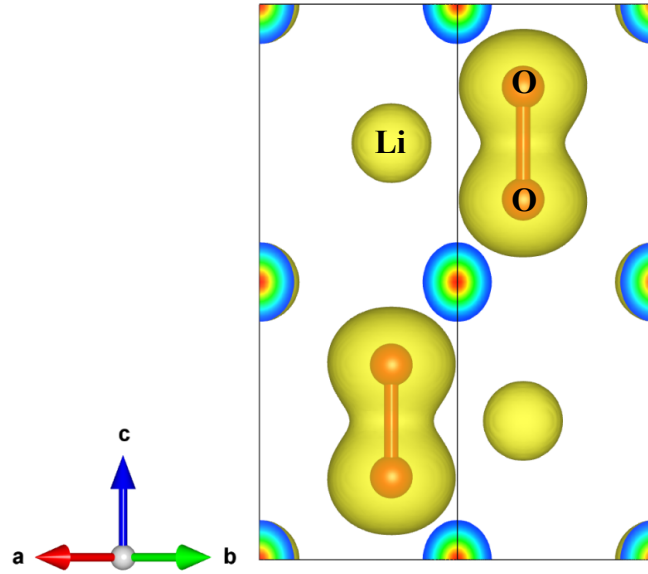
Method	$a/\text{\AA}$	$c/\text{\AA}$	$d_{\text{O-O}}/\text{\AA}$	Ref.
GGA-PBE	3.159	7.677	1.549	This work
	3.16	7.69	1.55	<sup>13</sup>
HSE06	3.119	7.607	1.504	This work
	3.12	7.61		<sup>14</sup>
	3.13	7.62		<sup>12</sup>
	3.13	7.60	1.50	<sup>15</sup>
GGA (WIEN2k)	3.1830	7.7258	1.55	<sup>3</sup>
Expt.	3.142	7.65	1.56	<sup>2</sup>

Table 3.1: Calculated lattice parameters of  $\text{Li}_2\text{O}_2$ .

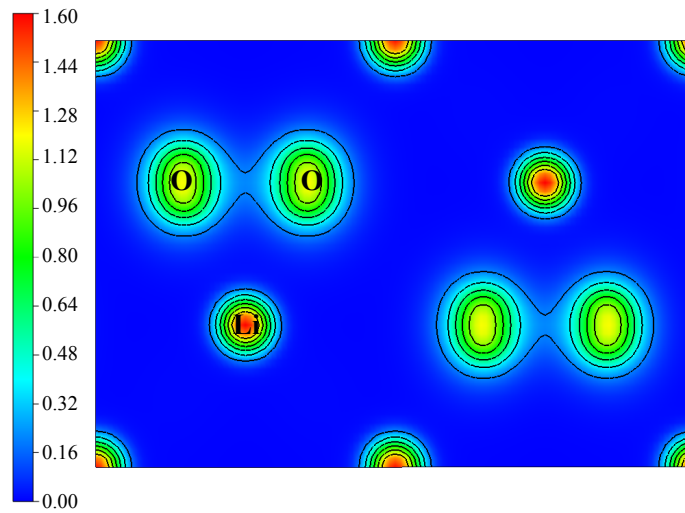
This ~1% different in lattice constants calculated by different methods indicates that in the following calculations, there would be a minimal strain effect introduced by changing the percentage of HF mixing in HSE while keeping the same geometric parameters as that calculated from HSE06 geometry optimization. In the following band gap calculation, we will continue to show that this strain will further give rise to a difference in the calculated band gap of about 0.3~0.4 eV using the same computational technique. This also explains the different band gap values of  $\text{Li}_2\text{O}_2$  in the literatures.

### 3.3.2 electron density distribution

Fig. 3.2 shows the calculated electron density distribution in  $\text{Li}_2\text{O}_2$ . The results indicate that the oxygen atoms form highly covalent O-O bond within  $\text{O}_2^{2-}$  peroxide anion. And the oxygen peroxide species located within the  $\text{Li}^+$  cation matrix, forming ionic bonds between  $\text{O}_2^{2-}$  and  $\text{Li}^+$ .



(a)



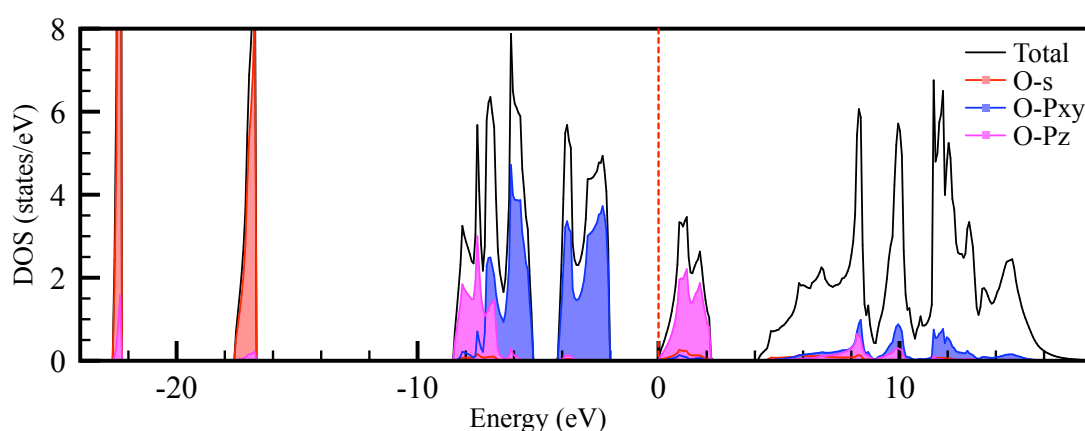
(b)

Fig. 3.2: (a) Electron density distribution in  $\text{Li}_2\text{O}_2$  with an isosurface level of  $1.60 \text{ a}_0^{-3}$  and (b) (11-20) slice illustrating electron density distribution in  $\text{Li}_2\text{O}_2$ . Contours are plotted up to  $1.60 \text{ a}_0^{-3}$  with an interval of  $0.32 \text{ a}_0^{-3}$ . ( $a_0$  : Bohr radius)

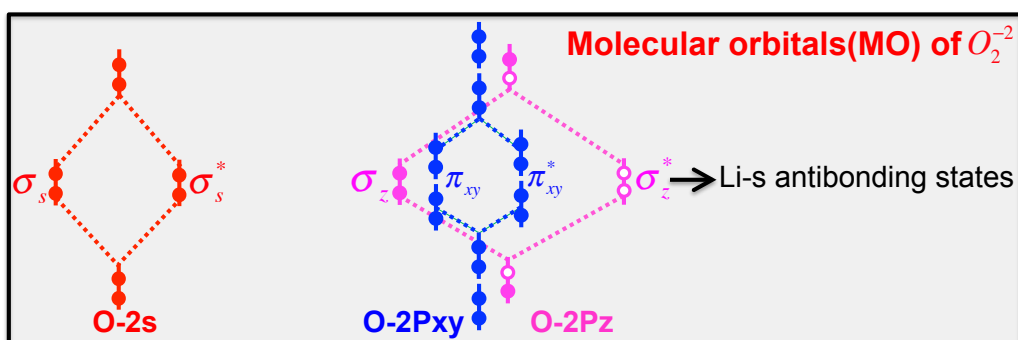
### 3.3.3 Electronic structure

#### 3.3.2.1 Density of states (DOS)

Fig. 3.3 plots the density of states (DOS) and corresponding molecular orbitals (MO) of  $\text{Li}_2\text{O}_2$  calculated by PBE. From this result, we can easily see that the electronic structure of  $\text{Li}_2\text{O}_2$  is dominated by the MO of  $\text{O}_2^{-2}$  peroxide anion. The valence band maximum (VBM) is composed of the fully occupied antibonding  $\pi_{xy}^*$  states from the oxygen  $p_x$ ,  $p_y$  orbitals, and the conduction band minimum (CBM) is formed by the unoccupied antibonding  $\sigma_z^*$  states from the  $p_z$  orbitals, resulting from the binding between two oxygen atoms. This molecular nature of O-O species in  $\text{Li}_2\text{O}_2$  is quite important for the other properties that will be discussed in the following parts of this thesis.



(a)



(b)

Fig. 3.3: (a) Density of states calculated by GGA-PBE and the (b) corresponding molecular orbitals of  $\text{Li}_2\text{O}_2$ . The energy is referred to the Fermi level. The dashed line indicated the position of Fermi level.

### 3.3.2.2 Bandgap calculation

The calculated bandgap values of  $\text{Li}_2\text{O}_2$  in this study together with the

literature ones are listed in Table 3.2.

From the study of literature, we found there is a slight difference among the bandgap obtained by different groups using the same calculation method. And a further investigation confirmed that this difference is due to the different treatment of bulk lattice parameters of  $\text{Li}_2\text{O}_2$ . Bandgap calculated based on PBE optimized geometry are generally  $\sim 0.4$  eV smaller than those based on HSE06 optimized structure. Therefore in this study, we performed the bandgap calculation based on both sets of lattice constants.

Both of these two sets calculation results are summarized in the left and right column of Table 3.2 respectively. We can clearly see that our PBE and HSE06 calculated bandgap based on both two sets of lattice constants agree quite well with previous literature results. This result not only explains the different existing in literature values, but also gives us information about that changing of  $\text{Li}_2\text{O}_2$  lattice constants upon different calculation methods will result in a change of bandgap. This strain induced bandgap change may deserve a detailed studied somewhere else.

From these results, we can clearly see the bandgaps calculated at both PBE and HSE06 lattices are gradually opened from PBE to HSE06, and finally GW approximation. PBE predicts the bandgap to be around 2.0 eV, and HSE06 gives the gap value more than 4.0 eV, while GW approximation calculated results are ranged from 5.0 to 7.0 eV.

By comparing our GW approximation results with literature ones, we found for PBE optimized lattices, our GGA based GW0 (GGA-GW0) calculation gives a bandgap value just lying in between the literature G0W0 and scGW predicted ones. This result is consistent with previous theoretical predictions. By using HSE wavefunction as the starting point of GW0, the calculated bandgap is further increased. Finally we obtained the HSE-GW0 bandgap value of  $\text{Li}_2\text{O}_2$  to be 6.50 eV and 6.85 eV for PBE and HSE06 optimized geometry respectively.

Method	GGA-PBE*	Ref.	HSE06*	Ref.
GGA-PBE	1.95	This work	2.35	This work
	1.99	<sup>16</sup>	2.35	<sup>14</sup>
HSE06	4.05	This work	4.45	This work
	4.19	<sup>16</sup>	4.57	<sup>14</sup>
			4.50	<sup>12,17</sup>
GGA-GW	5.70 (GW0)	This work	-	-
	5.15 (G0W0)	<sup>16</sup>	5.70 (G0W0)	<sup>14</sup>
	6.37 (scGW)	<sup>16</sup>	7.76 (scGW)	<sup>14</sup>
HSE-GW	6.50 (GW0)	This work	6.85 (GW0)	This work

Table 3.2: Comparison of  $\text{Li}_2\text{O}_2$  bandgap calculated by difference methods.

\* GGA-PBE or HSE06 optimized lattice constants.

In Fig. 3.4, we summarized the calculation results of the band edges and bandgaps of  $\text{Li}_2\text{O}_2$  by using different calculation methods. In addition to the results of gradually opened bandgap, the shift of the band edges is also obvious. By using the different calculation methods from PBE, HSE06 and to GW0, the band edges are also shifted as VBM moves to lower energy and CBM to higher energy levels respectively.

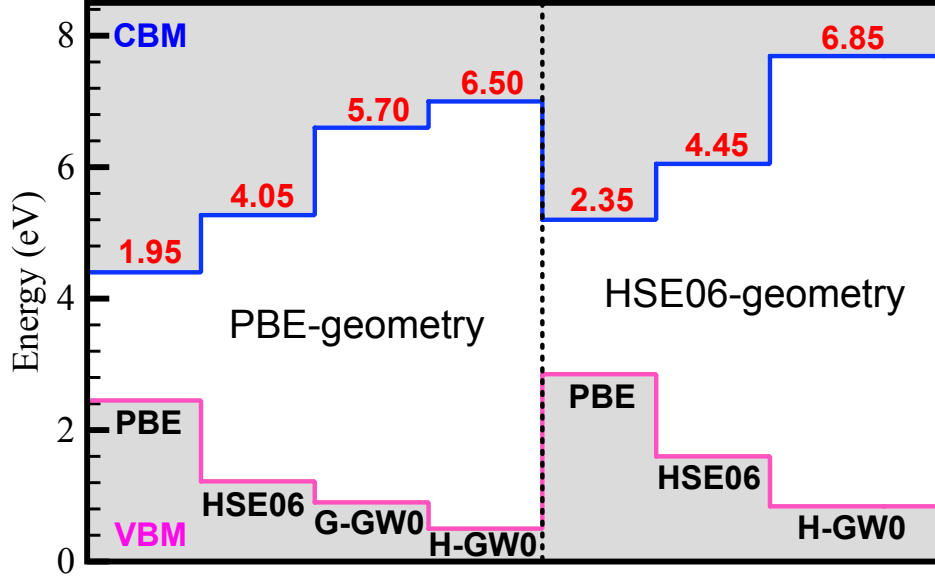


**Fig. 3.4:** Comparison of band edges and bandgaps calculated using different methods. The left and right columns indicate the calculation are performed based on PBE and HSE06 calculated lattice constants respectively. The number in red gives the bandgap values. The pink and blue lines draw the positions of VBM and CBM respectively.

In GW approximation, one of the most important points is the convergence of the results with respect the number of bands used in the calculation. Here in Table 3.3 and Fig. 3.5 we summarized the results of the convergence tests of bandgaps and band edges with respect to the number of bands. The default values of bands in  $\text{Li}_2\text{O}_2$  is 32, and we used to different values of 160 and 256, with are five and right times of the default value respectively. The results show that the bandgaps calculated using these two values are well converged to 0, and the band edges are also converged to 0.2 eV. All these results agree quite well with the available literature results.

NBANDS	160/256
$\Delta\text{bandgap}$	0 eV
$\Delta\text{VBM}$	0.2 eV
$\Delta\text{CBM}$	0.2 eV

Table 3.3: Energy difference in bandgap and band edges (VBM and CBM) calculated with the number of bands equals to 160 and 256 respectively in GW calculation.



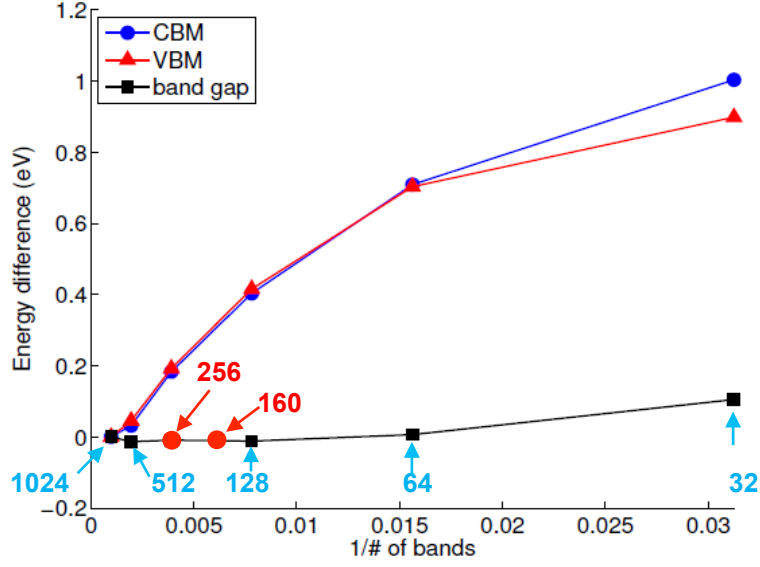


Fig. 3.5: Convergence tests of the bandgap and bandedges (VBM and CBM) with respect to the number of bands in GW calculation, as compared to the available literature values.<sup>14</sup> The red solid circles indicate our calculated results and the black solid squares are the data from the literature.

We further obtained the band structure of  $\text{Li}_2\text{O}_2$  in GW approximation by applying wannier90 calculation, and the result based on the HSE06-GW0 method of the PBE geometry is plotted in Fig. 3.6. From this result we can clearly see that  $\text{Li}_2\text{O}_2$  is a direct bandgap insulator. The minimum gap between the VBM and CBM occurs on the  $\Gamma$  point of the Brillouin zone.

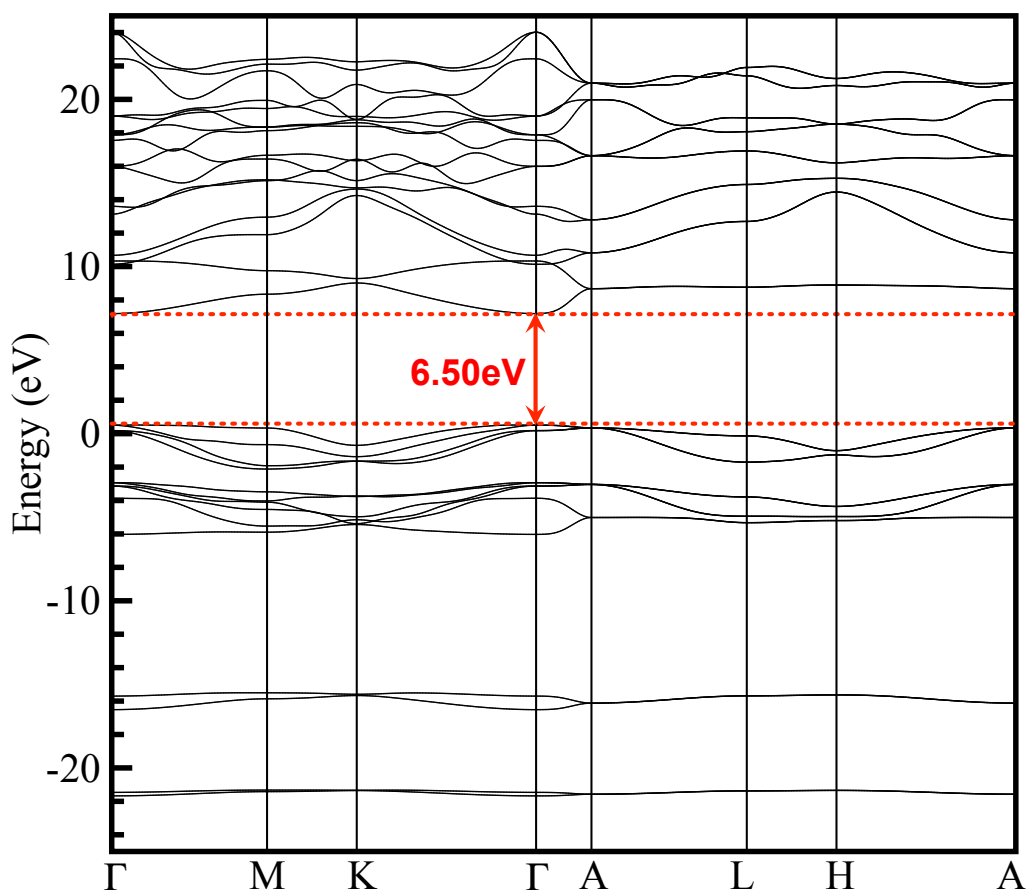


Fig. 3.6: HSE06-GW0 calculated band structure of  $\text{Li}_2\text{O}_2$  based on the PBE resulted geometry. The red dashed line represents the VBM and CBM, and the value gives the calculated band gap.

As in HSE calculation, partial semi-exchange is replaced by the Hartree-Fock (HF) exact exchange to compensate for the self-interaction error, here as a common practice,<sup>14</sup> we also adjusted the fraction of exact exchange used in HSE calculation to reproduce the GW calculated bandgap.

The fraction of exact exchange is determined by the mixing parameter  $\alpha$ . In Fig. 3.7 we summarized the calculation results for the optimization of mixing parameter  $\alpha$ . The results show a very good linearity of the bandgap with respect to mixing parameter. This is consistent with the theoretical basis of the functional form of the HSE family, which determines that if the atomic geometry and wavefunction of systems do not change with  $\alpha$ , energy will vary linearly with  $\alpha$ . Thus increasing the fraction of exact exchange mixing parameter will shift the partially occupied orbitals to higher energy levels. And at a particular value of  $\alpha$ , the self-interaction error from the semilocal

exchange will be exactly compensated, and a ‘correct’ bandgap will be obtained. And this method is now widely used in semiconductor calculations for bandgap prediction, because the defect properties in semiconductor, especially the defect levels are greatly affected by the value of bandgap.<sup>14</sup>

In the following part of this thesis, for the defect properties in  $\text{Li}_2\text{O}_2$ , we adapted the lattice constants calculated by HSE06, and adjusted the mixing parameter  $\alpha$  to be 0.5 in order to get a bandgap value of 6.50 eV, which is close to our HSE06-GW0 related results and also comparable to previous treatment of the bandgap.<sup>12,14</sup>

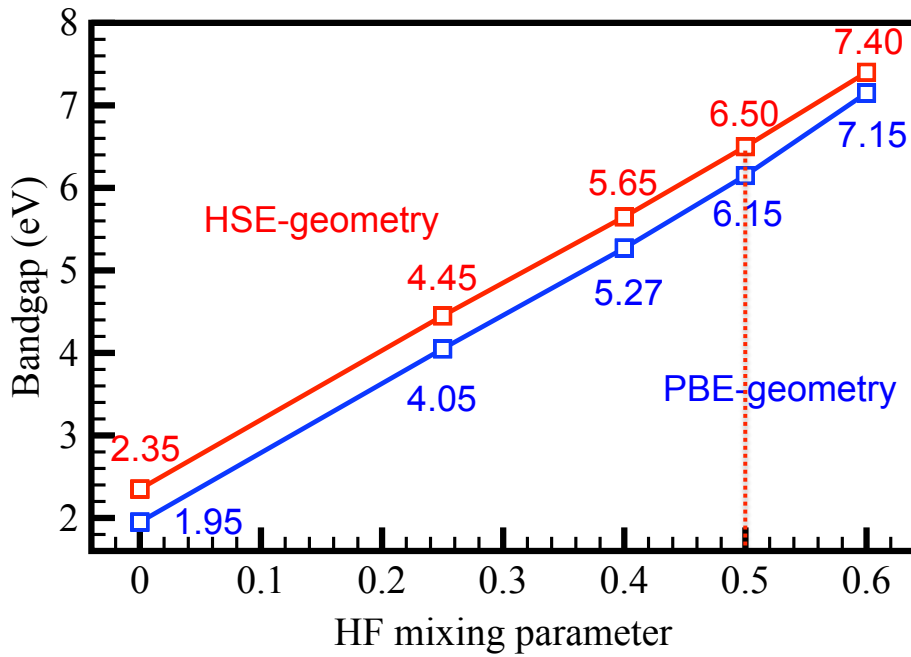


Fig. 3.7: HSE bandgap results calculated as a function of the HF mixing parameter. The red and blue lines indicate the results are calculated based HSE06 and PBE resulted lattice constants respectively.

### 3.4 Conclusions

In this part of study, we performed a benchmark calculation about the bulk properties of  $\text{Li}_2\text{O}_2$ . The crystal structure, electron density distribution, electronic structure, and very importantly the bulk bandgap were calculated and discussed in detail. From the results we know that:

- 1) The structure of bulk  $\text{Li}_2\text{O}_2$  contains an array of highly covalent  $\text{O}_2^{-2}$  molecular anions and a matrix of  $\text{Li}^+$  cations.
- 2) The electronic structure of  $\text{Li}_2\text{O}_2$  is mainly dominated by the molecular orbital of  $\text{O}_2^{-2}$  peroxide anion.
- 3) The PBE, HSE06 and GW calculation result in quite different bandgap values. And our HSE06-GW0 result gives a bandgap value of more than 6.50 eV.

These results demonstrate the insulating nature of  $\text{Li}_2\text{O}_2$ , thus due to the large bandgap of bulk  $\text{Li}_2\text{O}_2$ , the possibly existing defects are supposed to be important to improve the conductivity of  $\text{Li}_2\text{O}_2$ . Besides, our calculation also indicates that a careful treatment of the bulk bandgap will be important for the further calculations.

## REFERENCES

1. F. Fehér, I. Von Wilucki, and G. Dost, *Chemische Berichte*, 1953, 86, 1429–1437.
2. H. Föpl, *Zeitschrift für anorganische und allgemeine Chemie*, 1957, 291, 12–50.
3. L. G. Cota and P. de la Mora, *arXiv*, 2005, physics.atm-clus.
4. H. Wu, H. Zhang, X. Cheng, and L. Cai, *Philosophical Magazine*, 2007, 87, 3373–3383.
5. M. Shishkin and G. Kresse, *Phys. Rev. B*, 2006, 74, 035101.
6. M. Shishkin, M. Marsman, and G. Kresse, *Phys. Rev. Lett.*, 2007, 99, 246403.
7. M. Shishkin and G. Kresse, *Phys. Rev. B*, 2007, 75, 235102.
8. J. P. Perdew, K. Burke, and M. Ernzerhof, *Phys. Rev. Lett.*, 1996, 77, 3865–3868.
9. J. Heyd, G. E. Scuseria, and M. Ernzerhof, *J. Chem. Phys.*, 2003, 118, 8207.
10. A. V. Krukau, O. A. Vydrov, A. F. Izmaylov, and G. E. Scuseria, *J. Chem. Phys.*, 2006, 125, 224106.
11. F. Fuchs, J. Furthmüller, F. Bechstedt, M. Shishkin, and G. Kresse, *Phys. Rev. B*, 2007, 76, 115109.
12. J. B. Varley, V. Viswanathan, J. K. Nørskov, and A. C. Luntz, *Energy Environ. Sci.*, 2014, 7, 720.
13. M. D. Radin, J. F. Rodriguez, F. Tian, and D. J. Siegel, *J. Am. Chem. Soc.*, 2012, 134, 1093–1103.
14. M. D. Radin and D. J. Siegel, *Energy Environ. Sci.*, 2013, 6, 2370–2379.
15. S. P. Ong, Y. Mo, and G. Ceder, *Phys. Rev. B*, 2012, 85, 081105.
16. M. D. Radin, F. Tian, and D. J. Siegel, *J Mater Sci*, 2012, 47, 7564–7570.
17. J. Kang, Y. S. Jung, S.-H. Wei, and A. C. Dillon, *Phys. Rev. B*, 2012, 85, 035210.



## Chapter 4 Intrinsic point defects in $\text{Li}_2\text{O}_2$

### 4.1 Introduction

Different to the structure of perfect lattices, in real materials there are always various kinds of defects. Point defects occur at or around a single lattice point, and their range are usually limited to only a few atoms. Except for impurities, the intrinsic point defects in solid include vacancies, self-interstitials and antisite defects. The latter is formed by exchanging the positions of different types of atoms. The electronic charge state and lattice positions of point defects can be described by the Kröger-Vink Notation, which is proposed by F. A. Kröger and H. J. Vink.<sup>1</sup> According to this notation, point defects can be denoted in the way of  $M_S^C$ . Here ***M*** indicates the species, including atoms (e.g., C, O), vacancies (V), electrons (e) and holes (h). ***S*** denotes the lattice sites of the species, including the original atomic sites (e.g., C, O) and lattice interstices (i). ***C*** is the electronic charge states of point defects related to the original site. This charge state is obtained by the current charge minus the original one. Usually  $\times$  denotes for null charge,  $\bullet$  indicates a single positive charge and two means two positive charge. The negative charge is presented by  $'$ , with one corresponding to one single charge and two corresponding to two charges. However in this study, for clarity we will use the numbers directly to denote the charge states.

The existence of point defects in solids significantly affects their physical properties, and plays a decisive role in their applications. They are important conductive and reactive centers in materials. Especially for semiconductors, the incorporation of even a small fraction of point defects will greatly change their electronic conductivity. In order to understand the fundamental mechanism of effect of point defects in controlling the properties, first principles studies are essential. This is because experimental direct identification of point defects is rather difficult, while first principles calculation has found their success in increasing different fields and become more and more accurate as the development of the computational science.

From the bulk calculation of Li<sub>2</sub>O<sub>2</sub>, we found that Li<sub>2</sub>O<sub>2</sub> bulk is a wide bandgap insulator. Here in this part of study, we investigate the possible intrinsic point defects in Li<sub>2</sub>O<sub>2</sub>, including the formation energy, electronic structure, defect levels as well as binding between different defects.

## 4.2 Calculation methods

### 4.2.1 Defect types

In this part of calculation, we calculated the native vacancy including lithium ( $V_{Li}^q$ ), oxygen ( $V_O^q$ ) and di-oxygen vacancies ( $V_{O_2}^q$ ) at different charge state  $q$  ( $q = -1/0/+1$ ) as well as electron ( $e_p^-$ ) and hole ( $h_p^+$ ) polarons. According to the previous calculation that self-interstitials in Li<sub>2</sub>O<sub>2</sub> usually have high formation energies,<sup>2</sup> we will not consider this type of defects. And also due to our bulk calculation results, we now that the oxygen atoms form highly covalent bond with each other, the antisite type is also not likely to happen.

### 4.2.2 Modeling methods

A 3×3×2 supercell including 72 Li and 72 O atoms was used for all the defective calculations (see Fig. 4.1). The Li, O and O di-vacancies were simulated by removing one Li atom, one O atom, and one O-O pair from the supercell, respectively. As there are two symmetrically distinguishing Li sites, we considered two different Li vacancies at the O and T-sites ( $V_{LiO}^q$  and  $V_{LiT}^q$ ) respectively. The hole and electron polarons were formed by introduce an initial lattice distortion in the bulk as proposed in other works.<sup>2-4</sup> For hole polarons, the O-O bond length was initially shorten by 10%, and the 9 nearest Li<sup>+</sup> cations are shifted a little bit away from this O-O pair. For electron polarons, the O-O bond length is elongated by 20%.



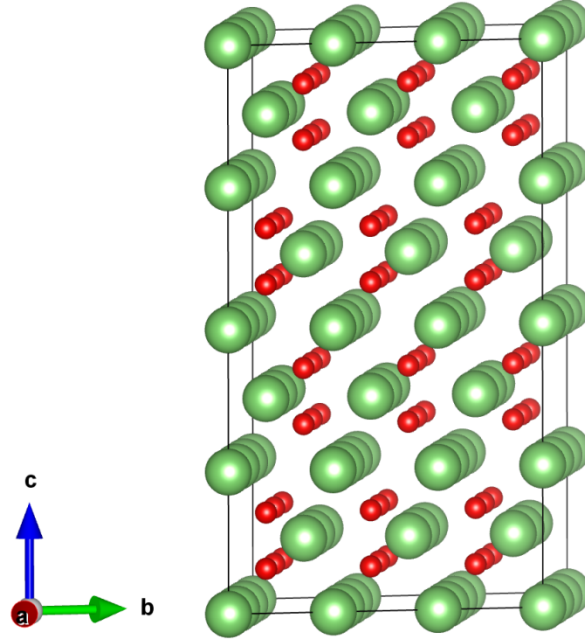


Fig. 4.1: A  $3 \times 3 \times 2$  supercell used for the calculation of intrinsic point defects in  $\text{Li}_2\text{O}_2$ .

#### 4.3.3 Calculation parameters

All the calculations were calculated based on HSE06 optimized geometry, and the  $\Gamma$  point only k-point mesh was used. During structure relaxation, the lattice constants were kept as constants, and only the atomic positions are allowed to relax by HSE06 until the force is within  $0.01\text{eV}/\text{\AA}$  and energy difference is less than  $10^{-6}\text{eV}$ . Due to the change of local spin states upon formation of charged point defect, spin polarized calculations were applied. All the charged point defects were calculated with a compensating homogeneous background charge.

The Freysoldt correction scheme<sup>5</sup> was applied for the corrections to Coulomb interaction between the charged point defect and its imaging charge as well as the electrostatic potential alignment. A Gaussian model charge with a width of 1 Bohr was used. In order to evaluate this finite size correction, we calculated the dielectric constants of  $\text{Li}_2\text{O}_2$  by using the density functional perturbation theory as well as the responds to the finite electric fields<sup>6</sup> for the electronic part as implemented in VASP. We got the three components of the dielectric constants as  $\epsilon_{xx} = 7.56$ ,  $\epsilon_{yy} = 7.55$ ,  $\epsilon_{zz} = 11.65$ , which is in good agreement with previous calculations.<sup>2</sup> Then an average value of 10 was used

for the Freysoldt correction.

In addition, in order to evaluate the influence of the fraction of exact exchange in the calculated results, we carried out the same calculation at two different  $\alpha$  values, 0.25 and 0.5. A careful comparison between the results was performed.

## 4.3 Results and discussion

### 4.3.1 Formation energy

The formation energy of different charge point defects was calculated by using the following formula:

$$E_f(X_q) = E_{tot}(X_q) - E_{tot}(bulk) - \sum_i n_i \mu_i + q(\epsilon_F + \epsilon_{VBM}) + \Delta_q \quad (\text{Eq. 4.1})$$

where,  $E_{tot}(X_q)$  and  $E_{tot}(bulk)$  are the total energies of the defective supercell containing a defect  $X$  in the charge state  $q$  and the perfect bulk supercell respectively.  $n_i$  and  $\mu_i$  are the number and chemical potential of the species that forms the defect. For vacancy  $n_i$  is negative, and for interstitials it is positive.  $\epsilon_F$  is the Fermi level referenced to the valence band maximum  $\epsilon_{VBM}$  of the bulk phase Li<sub>2</sub>O<sub>2</sub>. The last term is the Freysoldt correction to the charge-imaging interaction and potential alignment.

It is worth mentioning that these chemical potentials depend on experimental conditions during growth or annealing. In this part of calculation, the chemical potential of Li is referred to the calculated energy of bulk lithium metal, and O is referred to that of oxygen gas. Considering the real experimental condition, in our calculation of the formation energy, the chemical potential of Li is further related to the operation potential of the battery.

$$\mu_{Li}^{cathode} = \mu_{Li}^{bulk} - eU \quad (\text{Eq. 4.2})$$

The oxygen chemical potential is calculated as the one half of the free energy of oxygen at 300K and a pressure of 1 Bar.

$$G(300K, O_2) = E_0(O_2) + k_b T - TS_{\text{expt}} \quad (\text{Eq. 4.3})$$

where,  $E_0(O_2)$  is the calculated total energy of Li<sub>2</sub>O<sub>2</sub>,  $k_b T$  indicates the pV contribution, and  $S_{\text{expt}}$  is the experimental entropy.

The binding energy, which is defined as the difference in formation energies of independent defects and their complexes, can be calculated to evaluate the interaction between different defects. The calculation formula is as below:

$$E_b(AB) = E_f(A) + E_f(B) - E_f(AB) \quad (\text{Eq. 4.4})$$

Generally for  $E_b(AB) > 0$ , a complexes between A and B is favorable, whereas for  $E_b(AB) < 0$ , a separated configuration is more stable.

Another important quantity determines the defect behavior is the electronic transition level,  $\varepsilon_D(q/q')$ , which is defined as the Fermi-level position for which the formation energies of two different charge states are equal for the same defect type,<sup>7</sup>

$$\varepsilon_D(q/q') = [E_{\text{tot}}(D^q) - E_{\text{tot}}(D^{q'})]/(q' - q) \quad (\text{Eq. 4.5})$$

where, D indicates the defect type.

The relative stability of different charge states within the Fermi-level range defines the defect behavior in the host material.

In Fig. 4.2, we summarized the as calculated formation energy of all the defects at different charge states as a function of Fermi level related to VBM at the equilibrium potential  $U_0 = 2.64\text{eV}$ .

From the comparison of these two results, we can clearly see that by increasing the exact exchanging fraction in the hybrid functional, the electron and hole polarons are stabilized respect to the fully delocalized distribution.

Especially for hole polaron, the HSE-0.25 calculation gives almost identical results for localized and delocalized charge distribution, while HSE-0.5 predicts the hole polaron is about 1eV stable than the full distribution configuration. Due to the decrease in  $\text{O}_2$  total energy, the oxygen related defects also stabilized. For Li vacancy, the formation energy is decreased by the experimental operating potential. And the calculation show that the formation energy of Li vacancy at the T-site is slightly smaller than that of the O-site, and this result is consistent with the other literature ones.<sup>2</sup> So we only plot the result for  $V_{\text{Li}_T}^-$ . The slope corresponds to the charge state of each defect, and the intersection indicated the transition levels. From this result, we found the dominating charge state for Li, O and di-O vacancies are the negative, neutral, and +2 charge states respectively.

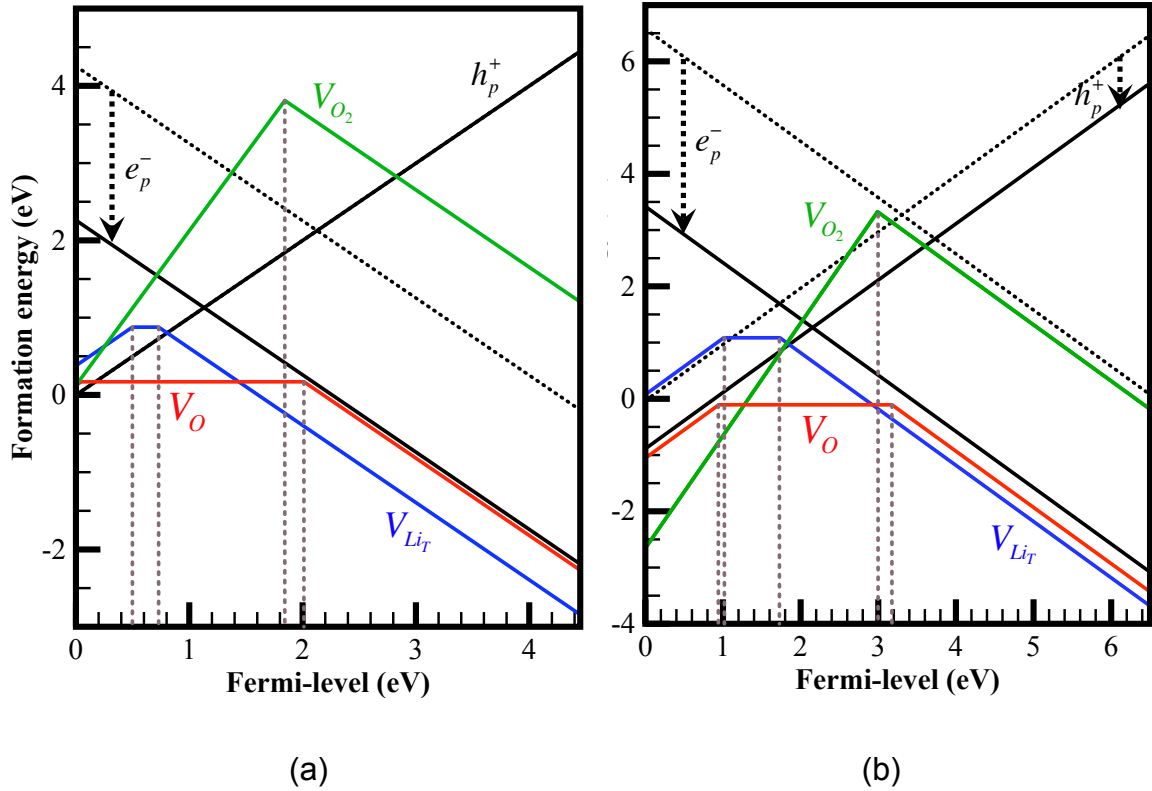


Fig. 4.2: Calculated formation energy of the intrinsic charged point defects in  $\text{Li}_2\text{O}_2$ , at (a)  $\alpha = 0.25$  and (b)  $\alpha = 0.5$ . Oxygen chemical potential is calculated at 300K and a pressure of 1 Bar. Li potential is calculated at the equilibrium voltage of 2.64eV. The black dashed line indicated the fully delocalized electron and hole in the system.

### 4.3.2 Electronic structure

#### 4.3.2.1 *Electron and hole polarons.*

For electron and hole polarons studied in this thesis, they are different from the electrons and holes fully distributed in the system, but they are the electron or hole centers that stabilized by the surrounding atomic distortion. From the result of formation energy, we know that the formation of polarons is energetically state compared to a delocalized distribution of the charge in the system. In Fig. 4.3, we summarized the molecular orbitals and the local atomic structure of hole and electron polarons as compared to that of the bulk  $\text{Li}_2\text{O}_2$  and oxygen molecule. The results demonstrated that upon formation of polarons, a pronounced change in the O-O bond length can be observed, together with some distortion in the surrounding  $\text{Li}^+$  cations. In bulk  $\text{Li}_2\text{O}_2$ , the O-O bond length is around 0.5 Å, while in hole and electron polarons, the bond length is either shortened or elongated to 1.37 Å and 2.16 Å respectively. And in oxygen molecule, the bond length is only 1.21 Å.

The change of bond length can be attributed to the change in molecular orbitals between the two oxygen atoms in different species. From Fig. 4.3, the difference in molecular orbitals is obvious. Compared to neutral oxygen molecule, the other species have more electrons in the orbitals, and the additional electron repulsion resulting in longer O-O bond length. And compared to bulk  $\text{Li}_2\text{O}_2$ , the formation of hole/electron polarons is corresponding to removing/adding one electron to the full-occupied oxygen  $P_{xy}$ /unoccupied oxygen  $P_z$  states respectively. Then the Coulomb interaction between the two oxygen atoms induces the change of O-O bond length for different polarons.

In Fig. 4.4 we plotted the calculated partial density of states (PDOS) of the hole and electron polarons as projected on the O-O polarons, together with the band decomposed charge density corresponding to the gap states. The PDOS shows clearly the polaron related gap states. For hole polaron, the gap state is from O- $P_{xy}$  and relatively near to the VBM ( $>2.0$  eV); while for electron polaron, it is from O- $P_z$  and relatively close to CBM ( $\sim 1.0$  eV). And the corresponding decomposed charge density of the gap states further

confirmed the shape of the defect states. These component and orbital shape of the gap states agrees with the above discussion of the molecular orbitals.

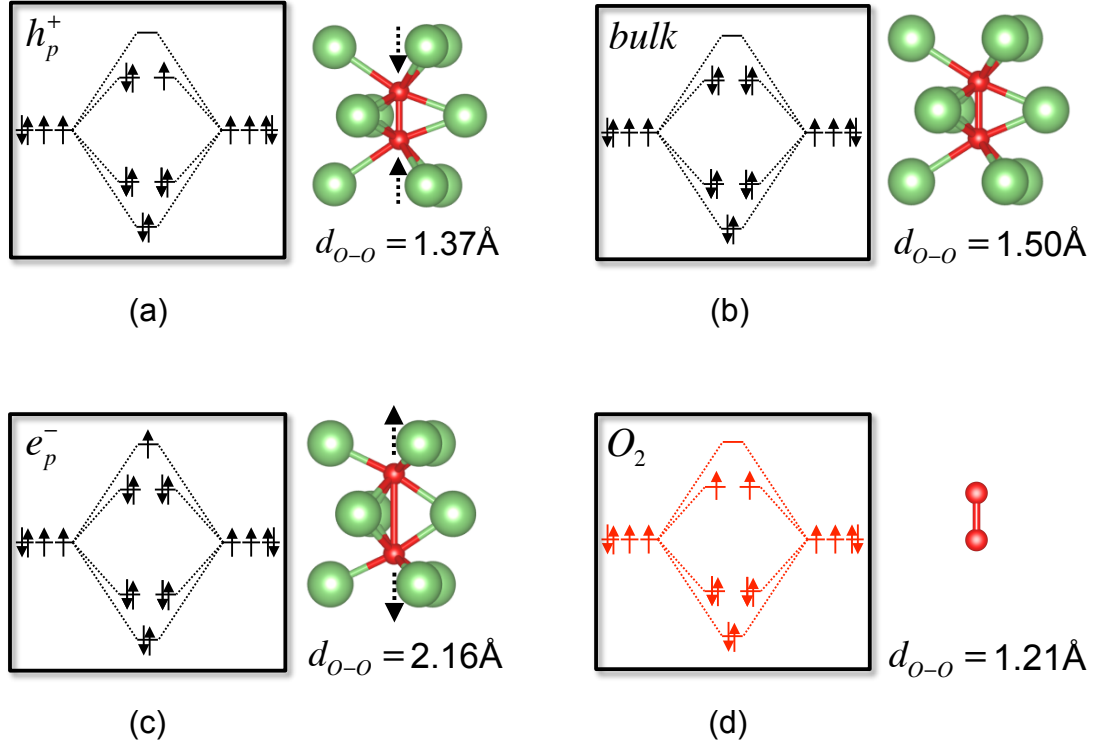


Fig. 4.3: Schematic draw of the molecular orbital and atomic structure for (a) hole and (c) electron polarons, as compared to the (b) bulk  $\text{Li}_2\text{O}_2$  and (d)  $\text{O}_2$  molecule. The red atoms are oxygen, and green ones are lithium.

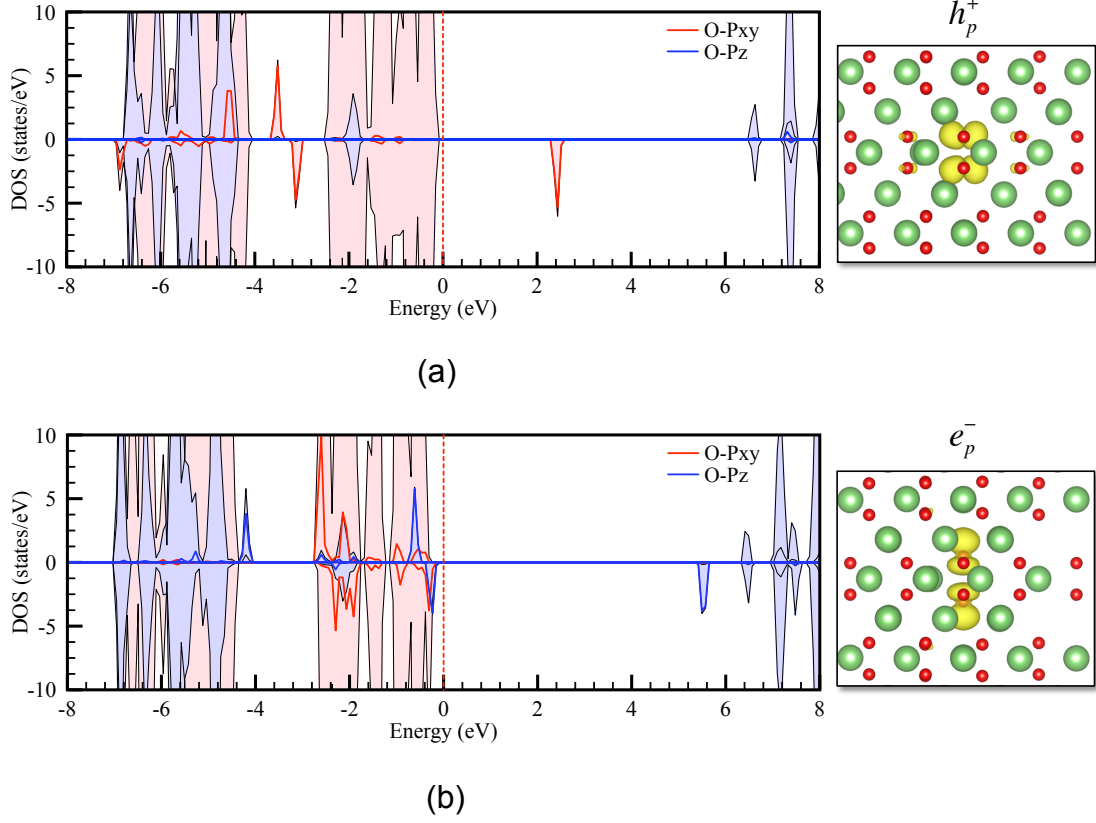


Fig. 4.4: The calculated PDOS and band decomposed charge density corresponding to the gap states for (a) hole and (b) electron polarons respectively. The red and blue lines are the DOS projected on the two oxygen atoms that forming the polarons. The pink and light-blue ranges indicate the DOS from all the oxygen atoms in the system.

#### 4.3.2.2 Li vacancy

For Li vacancy, from the result of formation energy, the dominating charge state is the negative charge state, which is formed by directly remove one  $\text{Li}^+$  from the system. Due to the fact that the electron structure of bulk  $\text{Li}_2\text{O}_2$  is determined by that of the oxygen peroxide anion, for  $V_{\text{Li}}^-$ , there is almost no change in the DOS and no defect levels are introduced.

The formation of neutral and negative charge states corresponds to the formation of one and two hole polarons within the surrounding O-O species due to Coulomb attraction. Fig. 4.5 gives a schematic draw of the atomic configuration for  $V_{\text{Li}_T}^q$  at different charge states. For Li vacancy at O-site, the similar results can be obtained. The binding energy between  $V_{\text{Li}_T}^-$  and  $h_p^+$  are calculated to be 0.85 eV and 0.12 eV for  $V_{\text{Li}_T}^0 \rightarrow V_{\text{Li}_T}^- + h_p^+$  and  $V_{\text{Li}_T}^+ \rightarrow V_{\text{Li}_T}^0 + h_p^+$

respectively, indicating a binding configuration between  $V_{Li_T}^-$  and  $h_p^+$  is stable. Moreover we also did the calculation for Li vacancy at -2 charge state, in which case, a separated configuration between  $V_{Li_T}^-$  and  $e_p^-$  was observed. This can be easily understood by the Coulomb repulsion.

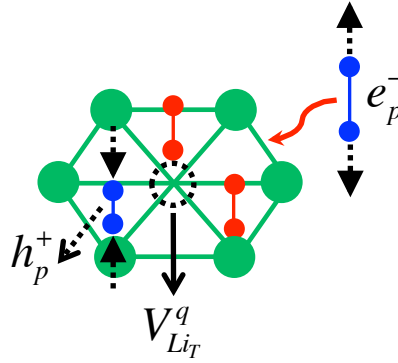


Fig. 4.5: Schematic draw of the atomic configuration of  $V_{Li_T}^q$ , indicating the formation of additional electron and hole polarons. The red and blue atoms are oxygen, and green ones are lithium. The black dashed circle means a lithium vacancy. The red curved arrowheads denote the electron polarons separated to the vacancy.

#### 4.3.2.3 O vacancy

For O vacancy, from the formation energy we know the neutral charge state is the most stable neutral defect in  $\text{Li}_2\text{O}_2$ . This result also agrees with the previous calculations.<sup>2</sup> This is explained by the following defect reaction:



This reaction process can be understood as that when one neutral oxygen is removed from the oxygen peroxide anion, the remaining oxygen atom becomes in -2 charge state, which is the most stable negative charge oxygen species. This conclusion is further confirmed by the results of changing the charged states of oxygen vacancy. Fig. 4.6 plots the atomic configuration of the oxygen vacancy at different charge states. The calculation shows that changing the charge states will not result in a direct change of this  $O^{-2}$ , but the formation of additional hole and electron polarons are observed. This



result further confirmed the ultra stability of  $\text{O}^{-2}$  against to further lose or gain electrons.

Different to the case of Li vacancy, this  $\text{O}^{-2}$  does not tend to bind with either electron or hole polarons, and a separated configuration is more energetically favorable.

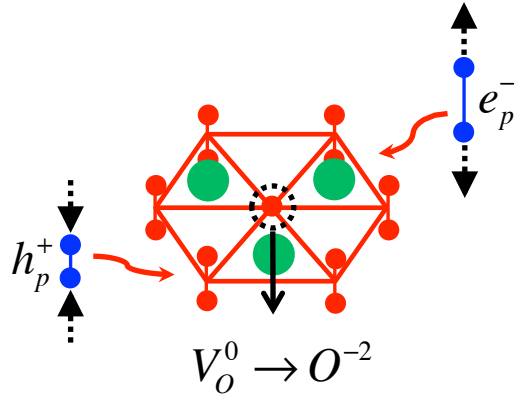


Fig. 4.6: Schematic draw of the atomic configuration of  $V_O^q$ , indicating the formation of additional electron and hole polarons. The red and blue atoms are oxygen, and green ones are lithium. The black dashed circle means an oxygen vacancy. The red curved arrowheads denote the electron and hole polarons separated to the vacancy.

#### 4.3.2.4 Di-O vacancy

For di-O vacancy, Fig. 4.2 shows the +2 charge state is the most stable one, and there is only one transition level  $\varepsilon(+2/-1)$ . This result indicates the +1 and 0 charge states are never stable for di-O vacancy. Then we plotted the charge density distribution of the neutral state in Fig. 4.7. From this electron density results, we can clearly see that when the neutral O-O was removed from the bulk, these two additional electrons associated with  $\text{O}_2^{-2}$  will remain at the vacancy site, surrounding by nine nearest  $\text{Li}^+$  cations. This process can be expressed by the following defect reaction equation:



Due to the local charge neutrality, there is almost no change in the local configuration of the nine surrounding  $\text{Li}^+$  cations. However this configuration

of coupled vacancy electrons is quite unstable with high formation energy. The high symmetric nine surrounding  $\text{Li}^+$  cations make it a metastable state. And the decrease of formation energy with respect to the positive charge states also indicates the two vacancy electrons tend to be removed. For  $V_{\text{O}_2}^0$ , the two vacancy electrons form a localized double occupied ( $S=1$ ) state. For  $V_{\text{O}_2}^{+1}$ , one of the electrons was removed resulting in a single occupied state ( $S=1/2$ ), and the two defect levels are splitted in energy. For  $V_{\text{O}_2}^{+2}$ , both two of the electrons are removed forming two unoccupied defect states (see Fig. 4.8). Upon changing the charge state, the local neutrality is also destroyed, accompanied by the nine surrounding  $\text{Li}^+$  cations removing away from the O-O center.

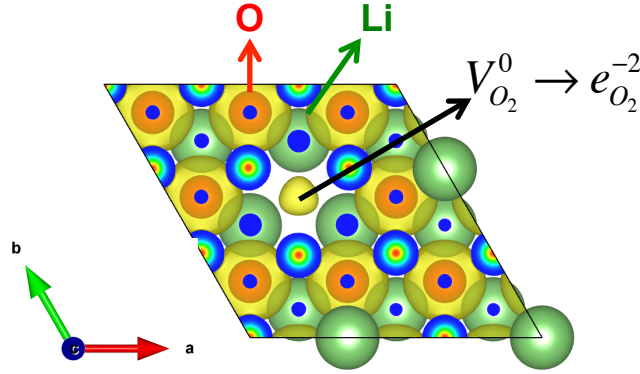


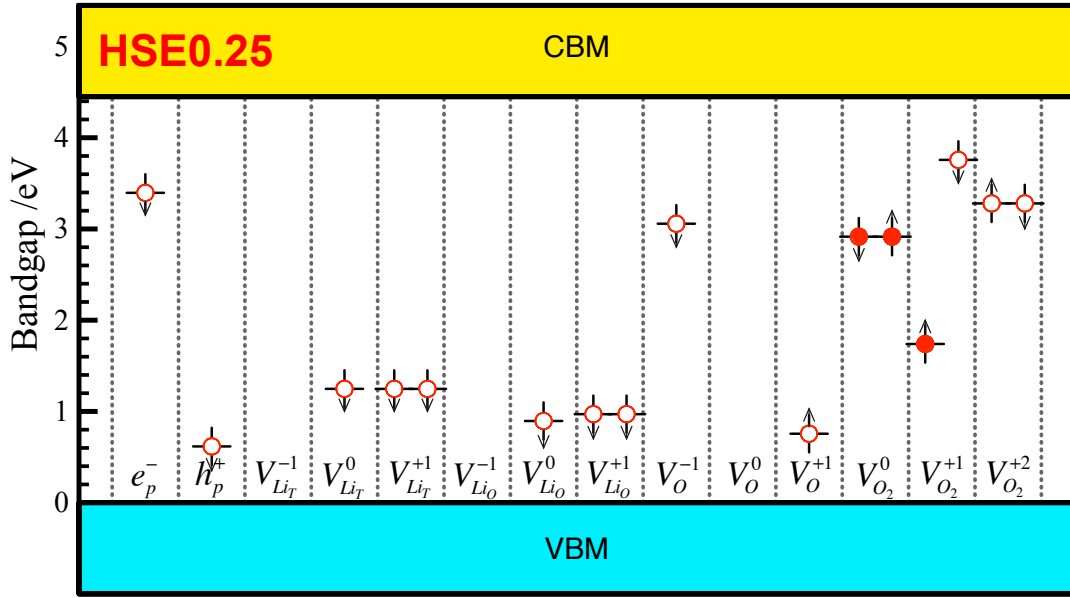
Fig. 4.7: Top view of the charge density of  $V_{\text{O}_2}^0$  indicating the vacancy electrons  $e_{\text{O}_2}^{-2}$  located at the original O-O site. The red atoms are oxygen, and green ones are lithium.

### 4.3.3 Defect levels

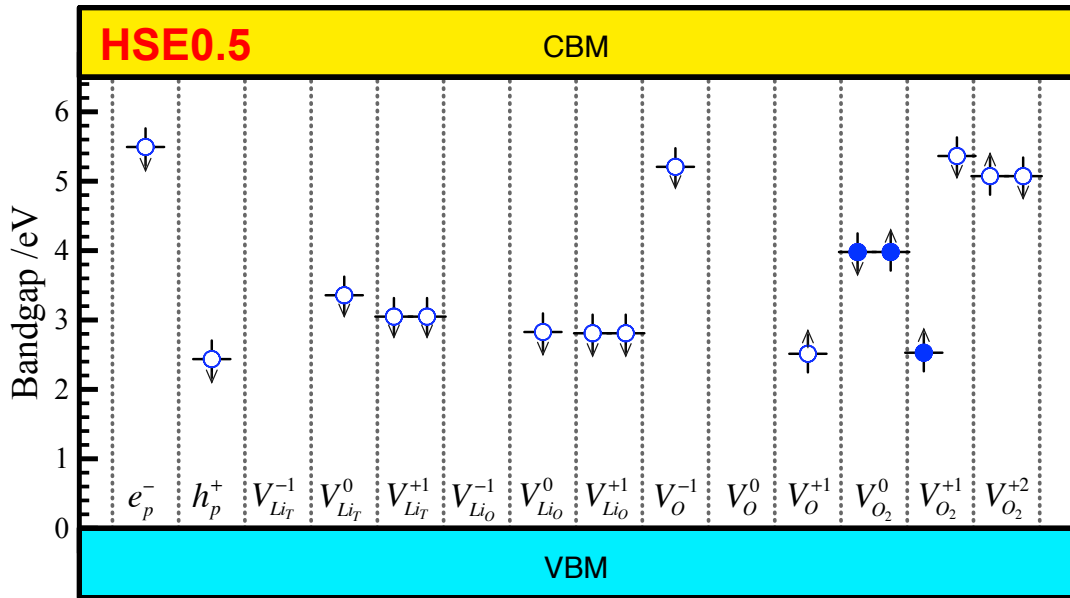
Fig. 4.8 presents a comparison of the defect levels calculated at different mixing parameters of the HSE calculation, and Table. 4.1 gives the energy levels of the defect levels referred to the VBM corresponding to the different mixing parameters. From a glance of these defect levels, we can see both two calculations give qualitatively consistent results. The unoccupied defect levels near to CBM and VBM for  $e_p^-$  and  $h_p^+$  are consistent with the results of DOS for both in the above discussion. For Li and O vacancies, the energy levels of the defect levels also agree with the above analysis of the formation of additional electron ( $V_{\text{O}}^{-1}$ ) and hole polarons ( $V_{\text{LiT}}^0/V_{\text{LiO}}^0$ ,  $V_{\text{LiT}}^{+1}/V_{\text{LiO}}^{+1}$  and  $V_{\text{O}}^{+1}$ ). For

di-O vacancy, we can clearly see the gradually change of the occupation of the defect states at the vacancy site. Upon the formation of positive charge states, the electrons at the vacancy site are also removed. This is also consistent with our above discussion about defect reaction.

However, by comparing the results in (a) and (b) together with the exact values of the energy levels listed in Table. 4.1, we also found when the bandgap is opened by increasing the fraction of exact exchange in HSE calculation, the defect levels also shifted to deep within the bandgap. Especially for the hole polaron-related defect levels, in HSE0.25 calculated results, they are around 1 eV near to the VBM, whereas in HSE0.5 calculated results, they shifted to around 3 eV in the bandgap. In this way, upon the increasing of mixing parameter, the hole polaron-related defects states become quite deep acceptor levels, which will be hardly effective for the conductivity of  $\text{Li}_2\text{O}_2$ . This conclusion demonstrates that the calculated defect levels are highly depended on the bandgap calculation.



(a)



(b)

Fig. 4.8: Defect levels for each defect species at different charge states calculated at (a)  $\alpha = 0.25$  and (b)  $\alpha = 0.5$  respectively. The bandgap of bulk  $\text{Li}_2\text{O}_2$  is 4.45 eV and 6.5 eV respectively for (a) and (b). The open circles indicate the unoccupied states, and the solid circles indicate the occupied states. The arrowheads show the spin-up and spin-down states.

Defect type	HSE-0.25/eV	HSE-0.5/eV
$e_p^-$	3.40	5.49
$h_p^+$	0.62	2.44
$V_{Li_T}^{-1}$	-	-
$V_{Li_T}^0$	1.25	3.36
$V_{Li_T}^{+1}$	1.25/1.25	3.05/3.05
$V_{Li_O}^{-1}$	-	-
$V_{Li_O}^0$	0.90	2.83
$V_{Li_O}^{+1}$	0.97/0.97	2.81/2.81
$V_O^{-1}$	3.06	5.21
$V_O^0$	-	-
$V_O^{+1}$	0.76	2.51
$V_{O_2}^0$	2.92/2.92	3.98/3.98
$V_{O_2}^{+1}$	1.74/3.76	2.53/5.36
$V_{O_2}^{+2}$	3.28/3.28	5.07/5.07

Table. 4.1. Energy levels of the defect levels referred to the VBM of bulk Li<sub>2</sub>O<sub>2</sub> as calculated by HSE hybrid DFT method with 25% and 50% exact exchange respectively.

#### 4.4 Conclusions

In this part of study, we performed the calculation for intrinsic point defects in Li<sub>2</sub>O<sub>2</sub>, including the electron and hole polarons, Li, O and di-O vacancies. The formation energy, transition levels, atomic configuration as well as the electronic structures of each defect type were calculated and discussed in detail. The results demonstrated that:

- 1) The intrinsic defect properties of Li<sub>2</sub>O<sub>2</sub> are controlled by the ability of  $O_2^{-2}$  peroxide anion to change its charge states through the formation of electron and hole polarons.

- 2) The most stable neutral and negative defects in  $\text{Li}_2\text{O}_2$  are the neutral O vacancy and negative Li vacancy respectively. Other charge states of these two vacancies are corresponding to formation of additional electron and hole polarons.
- 3) Polaron hopping and Li vacancy migration are supposed to be the dominating charge transfer mechanisms related to intrinsic  $\text{Li}_2\text{O}_2$ . This is consistent with other literature works.

By calculating the diffusion barrier, the conductivity related the Li vacancy migration and polaron hopping mechanisms is estimated to be in the order of  $10^{-19}$  S/cm to  $10^{-20}$  S/cm respectively,<sup>2</sup> which is quite low compared to other battery materials as well as the experimental measured results.<sup>8</sup>

Thus expect for only the intrinsic point defect in  $\text{Li}_2\text{O}_2$ , the effects of extrinsic defect on the conductivity of  $\text{Li}_2\text{O}_2$ , including the intended doping as well as the unavoidable impurity, are worth investigating.

## REFERENCES

1. F. A. Kröger and H. J. Vink, Elsevier, 1956, vol. 3, pp. 307–435.
2. M. D. Radin and D. J. Siegel, *Energy Environ. Sci.*, 2013, **6**, 2370–2379.
3. J. Kang, Y. S. Jung, S.-H. Wei, and A. C. Dillon, *Phys. Rev. B*, 2012, **85**, 035210.
4. S. P. Ong, Y. Mo, and G. Ceder, *Phys. Rev. B*, 2012, **85**, 081105.
5. C. Freysoldt, J. Neugebauer, and C. Van de Walle, *Phys. Rev. Lett.*, 2009, **102**, 016402.
6. I. Souza, I. Souza, J. Íñiguez, J. Íñiguez, D. Vanderbilt, and D. Vanderbilt, *Phys. Rev. Lett.*, 2002, **89**, 117602.
7. C. G. Van de Walle and J. Neugebauer, *Annu. Rev. Mater. Res.*, 2006, **36**, 179–198.
8. O. Gerbig, R. Merkle, and J. Maier, *Advanced Materials*, 2013, **25**, 3129–3133.





## Chapter 5 Extrinsic doping effect in $\text{Li}_2\text{O}_2$

### 5.1 Introduction

Except for intrinsic point defects in solid, the presence of foreign atoms, namely impurities, in the lattice will also significantly alternate the properties of materials. All the real solids are imperfect. Some of the impurities are added on purpose, in order to improve the properties of host materials. And some are ineluctable impurities that will be introduced to the solids during crystal growth or annealing processes.

From the calculation in the previous parts, we already know that bulk  $\text{Li}_2\text{O}_2$  is an insulator with a large band gap. And the intrinsic defect properties of  $\text{Li}_2\text{O}_2$  show that the Li vacancy migration and hole polaron hopping are the most important defect conducting mechanisms. The calculated conductivity corresponding to these two mechanisms is consistent with the low conductivity of  $\text{Li}_2\text{O}_2$ . However they are still much lower than the other battery materials and the experiment measured values. So the effect of the possibly existing impurities is quite worth investigating.

Recently, Vladimir Timoshevskii et al. proposed an alternative way to use Si as a dopant to improve the conductivity.<sup>1</sup> In their study they found substitution of Li with Si atom will lead to the formation of additional conducting states right above the valence band maximum (VBM), and the Si doped  $\text{Li}_2\text{O}_2$  is expected to have much improved electron mobility than stoichiometric  $\text{Li}_2\text{O}_2$ . Here in this part of study, we did a systematic study of the doping effect of different light metals and semimetals in  $\text{Li}_2\text{O}_2$ . A comprehensive calculation and discussion of the effect of doping in  $\text{Li}_2\text{O}_2$  have been carried out.

In addition, despite the intended doping, there is also one type of unavoidable impurity in most of the solids, which is the hydrogen impurity. Due to its abundant existence and its high reactivity with many materials, hydrogen is a very important impurity that affects the electronic structure of semiconductors. And hydrogen also exhibits a number of complex behaviors. For LAB, even in non-aqueous LAB, the residue water within electrolyte as well as the moisture

from air would both introduce hydrogen in the battery system and become hydrogen sources. Due to the complex property of hydrogen and its highly reactivity with other defects in the host, it may greatly affect the electronic conductivity of  $\text{Li}_2\text{O}_2$ . So in this part of calculation, the behavior of hydrogen in  $\text{Li}_2\text{O}_2$  has also been investigated in detail.

## 5.2 Calculation methods

In this part of study, we did two relatively separate calculations including the effect of metal/semimetal doping in  $\text{Li}_2\text{O}_2$  and the behavior of hydrogen impurity in  $\text{Li}_2\text{O}_2$ . For the first part of intended doping in  $\text{Li}_2\text{O}_2$ , Li atoms are substituted by Na, Mg, Al, Si, K, and Ca atoms respectively. The reason of choosing these light elements is mainly due to the realistic consideration that under experimental condition of LAB, these elements other than the heavy transition metals are mostly possible to exist. Moreover, by calculating the doping with these different elements, the effect of changing in valence electrons and atomic radii of doping atoms can be investigated. Thus by choosing the first four elements in the second period, we can easily see the effect of increasing valence electrons on doping, while by comparing the I and II group doping in the second and third period respectively, the atomic radii effect can be concluded. In case of hydrogen impurity in  $\text{Li}_2\text{O}_2$ , both the substitutional and interstitial hydrogen atoms were considered.

We used the same  $3\times3\times2$   $\text{Li}_2\text{O}_2$  supercell and  $\Gamma$  point only k-point mesh as that in the intrinsic defect calculation. The impurity concentration is around 0.7% percent. Spin polarization was taken into account due to the change of local spin states caused by doping. Atomic level structure optimization was performed by HSE06 until forces converged within 0.01 eV/Å and energy converged within  $10^{-6}$  eV, whereas the lattice parameters were kept as constants as that obtained from HSE06 bulk optimization. In order to see the bandgap dependence of defect levels, we carried out the calculation by PBE, HSE with 25% and 50% percent exact exchange respectively.

1) For metal/semimetal doping in  $\text{Li}_2\text{O}_2$ :

One Li atom is substituted by one doping atom. As there are two symmetrically distinguishing Li sites in  $\text{Li}_2\text{O}_2$ , the trigonal prism center (T-site) and the octahedral center (O-site), we did the calculation for both T-site and O-site substitution to compare the stability of these two doping sites (see Fig. 5.1)

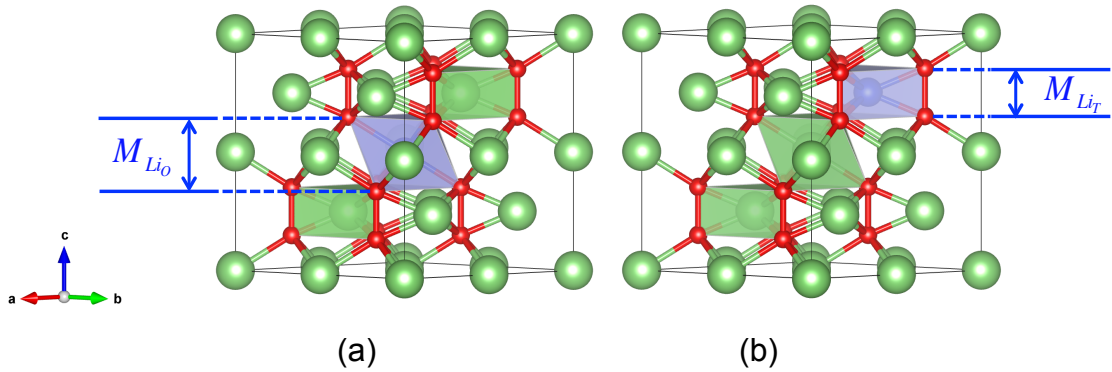


Fig. 5.1: Two distinguishing substitution sites of Li atom in  $\text{Li}_2\text{O}_2$ . Green, red and blue atoms indicate Li, O and doping atoms, respectively.

2) For hydrogen impurity in  $\text{Li}_2\text{O}_2$ :

The interstitial hydrogen ( $H_i$ ) atom can occupy a number of different interstitial positions in  $\text{Li}_2\text{O}_2$ . Since we focus on the effect of hydrogen impurities on the conductivity of  $\text{Li}_2\text{O}_2$ . Therefore, a thorough study of the hydrogen distribution in  $\text{Li}_2\text{O}_2$  is beyond the scope of this work. We first built possible interstitial configurations from the highly symmetric positions in  $\text{Li}_2\text{O}_2$ . As shown in Fig. 5.2a, these configurations include the body center of empty O-O trigonal prism, face-center of O-O trigonal prism, and the top/bottom site of O-O dimer; then we slightly shifted the hydrogen atom to the off-center position of each type in order to eliminate the symmetry effect on the results. After performing structure optimization calculations, we found except locating at the highly symmetric empty triangle prism center, the interstitial hydrogen atom prefers to bind with oxygen rather than lithium atom. Based on this observation, further efforts were attributed to investigate the binding position of hydrogen related to O-O peroxide anion, including

the O-O bond center (BC), O-O antibonding site (AB), as well as the off-center antibonding site (AB') (see Fig. 5.2b). The substitutional hydrogen in  $\text{Li}_2\text{O}_2$  was modeled by replacing one Li atom, one O atom or one O-O dimer with one H atom, forming  $H_{\text{Li}}$ ,  $H_{\text{O}}$  and  $H_{\text{O}_2}$ , respectively.

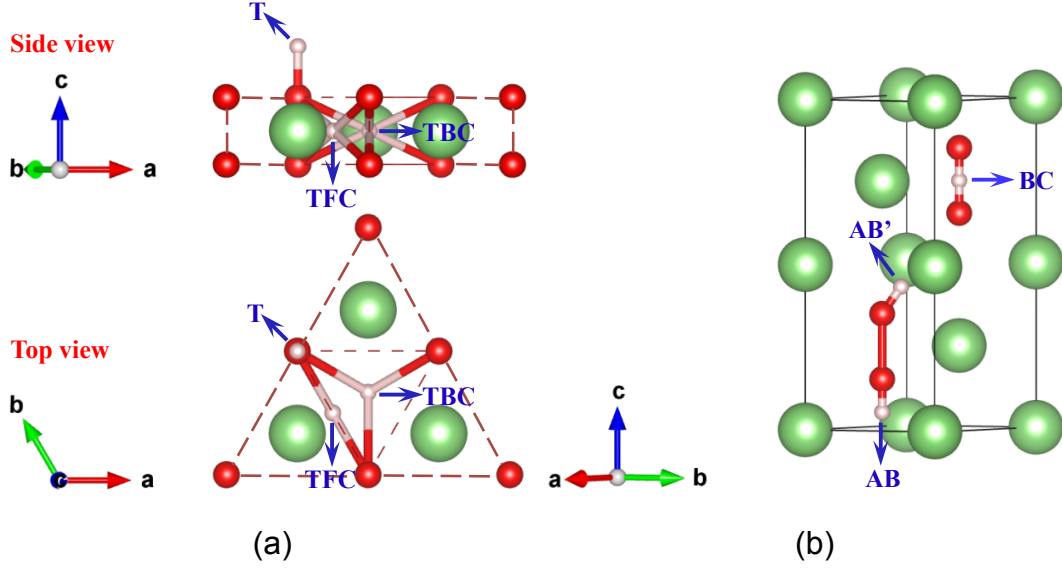


Fig. 5.2: Initial positions of interstitial hydrogen in  $\text{Li}_2\text{O}_2$ . (a) Possible interstitial configurations at the high symmetric sites in  $\text{Li}_2\text{O}_2$ , including the body center of empty O-O trigonal prism (TBC), face-center of O-O trigonal prism (TFC), and the top/bottom site of O-O dimer (T); (b) The bond center (BC) site, the antibonding center (AB) site as well as the off-center AB site (AB') related to O-O peroxide anion. Green, red and pink indicate the Li, O and H atoms respectively.

## 5.3 Results and discussion

### 5.3.1 Metal/semimetal doping in $\text{Li}_2\text{O}_2$

#### 5.3.1.1 Formation energy

The formation energy of metal/semimetal doping in  $\text{Li}_2\text{O}_2$  was calculated using the following formula for neutral charge state only:

$$E_f(M_{\text{Li}}) = E_{\text{tot}}(M_{\text{Li}}) - E_{\text{tot}}(\text{bulk}) - \mu_M + \mu_{\text{Li}} \quad (\text{Eq. 5.1})$$

Here,  $M$  denotes the metal/semimetal atom. The chemical potential of Li and

the dopant are referenced to the as calculated bulk energy.

In Fig. 5.3, we plotted the formation energy for different metal/semimetal doping in  $\text{Li}_2\text{O}_2$ , and the detailed results of the formation energy are listed in Table. 5.1. For comparison, we performed the calculation by both PBE and HSE with 50% percent exact exchange. The figure shows that both calculations gave consistent results. Except for Na and K, other metal/semimetal doping is favorable to be formed with negative formation energies. In addition, by comparing the results from the III period elements, we found that by increasing the valence electrons of the dopant atom, the formation energy decreases. In contrast, comparison between Na and K, together with Mg and Ca, indicates that the formation energy increases upon increase the atomic radius of the dopant. And Si doping results in the lowest formation energy on both T- and O-site Li.

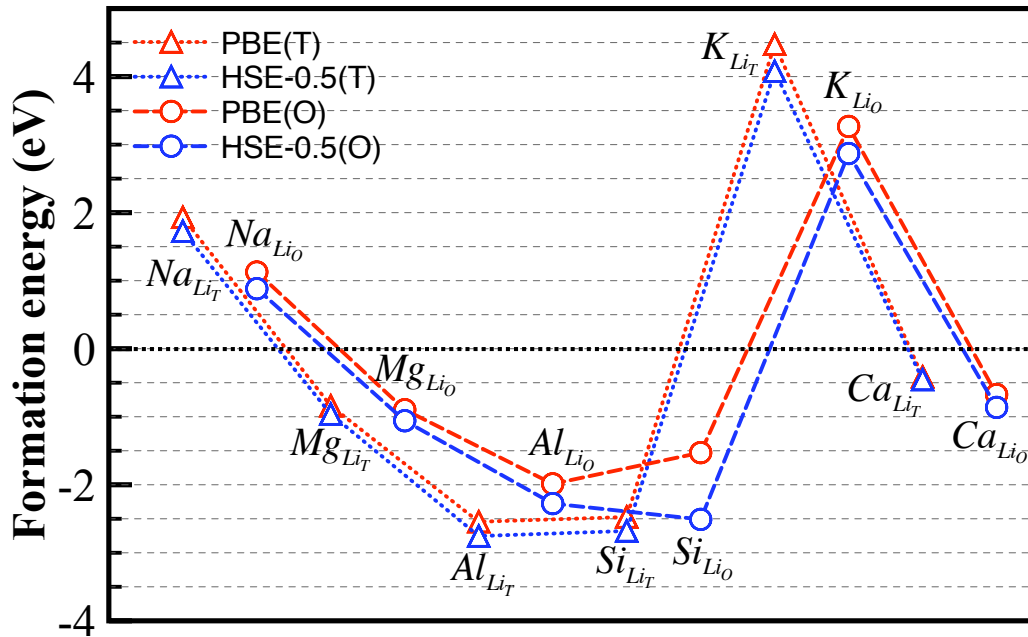


Fig. 5.3: Formation energy of different metal/semimetal doping in  $\text{Li}_2\text{O}_2$  at two systematical distinguishing Li sites. Circle and triangles are the results at T and O-site Li respectively. Red and blue lines indicate the calculation is performed by PBE and HSE with 50% HF exact exchange respectively.

Defects	PBE-GGA/eV	HSE-0.5/eV
$\text{Na}_{\text{Li}_T}$	1.93	1.73
$\text{Na}_{\text{Li}_O}$	1.13	0.88
$\text{Mg}_{\text{Li}_T}$	-0.84	-0.96
$\text{Mg}_{\text{Li}_O}$	-0.90	-1.06
$\text{Al}_{\text{Li}_T}$	-2.54	-2.75
$\text{Al}_{\text{Li}_O}$	-1.99	-2.28
$\text{Si}_{\text{Li}_T}$	-2.47	-2.68
$\text{Si}_{\text{Li}_O}$	-1.53	-2.51
$\text{K}_{\text{Li}_T}$	4.47	4.08
$\text{K}_{\text{Li}_O}$	3.27	2.87
$\text{Ca}_{\text{Li}_T}$	-0.41	-0.46
$\text{Ca}_{\text{Li}_O}$	-0.67	-0.86

Table. 5.1: Formation energies of different metal/semimetal doping in  $\text{Li}_2\text{O}_2$  at two systematical distinguishing Li sites as calculated by GGA-PBE and HSE-0.5 respectively.

### 5.3.1.2 Atomic configuration

Fig. 5.4 gives a schematic draw of the local atomic configuration corresponding to each metal/semimetal doing. Fig. 5.4(a) plots the substitution of T-site Li together with three neighboring O-O peroxide anions and six nearest Li atoms in the same plan, whereas (b) plots the substitution of O-site Li with six surrounding O-O peroxide anions. From this result, we can clearly see that except Na and K, other doing will lead to the formation of electrons polarons within O-O species next to the dopant atom for both T- and O-site substitution. And the number of the polarons are equal to the number of additional valence electron of the doing atom compared to Li. From this point of view, we may guess that the metal/semimetal doing in  $\text{Li}_2\text{O}_2$  will result in donation of additional valence electrons from the dopant to surrounding O-O peroxide anions to form electron polarons. Moreover, together with the conclusion of the formation energy, we may predict that the formation of

addition electron polarons will stabilize the metal/semimetal doing.

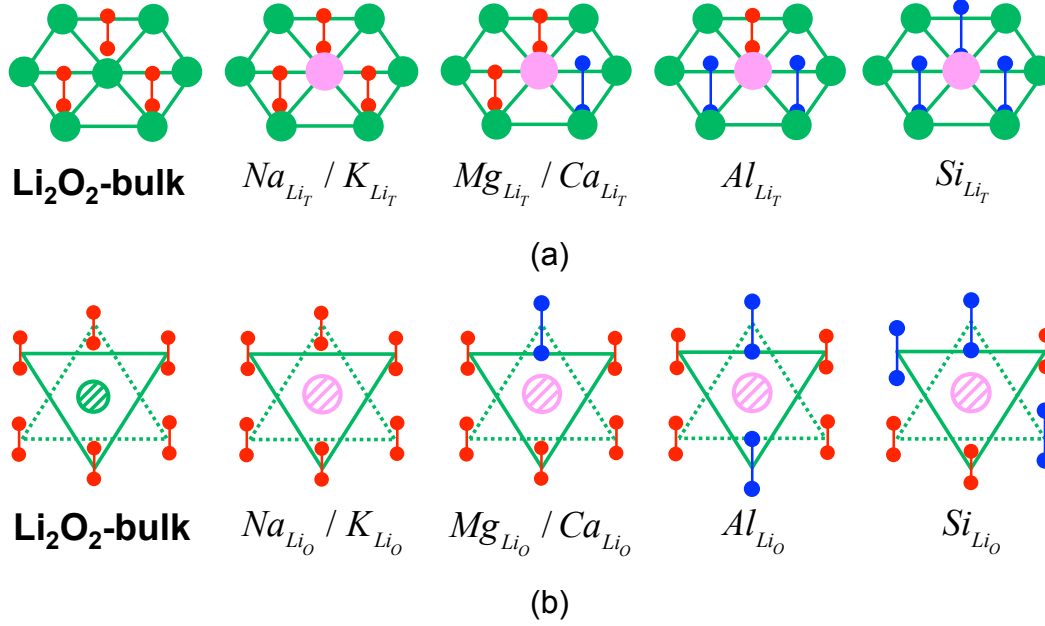


Fig. 5.4: Atomic configuration of different metal/semimetal doping in  $\text{Li}_2\text{O}_2$  at two systematical distinguishing Li sites ((a): T-site, (b): O-site), compared to that of bulk  $\text{Li}_2\text{O}_2$ . Green atoms are Li, pink ones are doping atoms, and red/blue ones are O. The blue O-O indicates the elongation of O-O bond length.

### 5.3.1.3 Defect levels

Fig. 5.5 and Table. 5.2 summarized the calculated defect levels of different metal/semimetal doping in  $\text{Li}_2\text{O}_2$ . The calculation is performed by HSE with 50% exact exchange, resulting in a bandgap of 6.5eV for bulk  $\text{Li}_2\text{O}_2$ . Similar to the case of intrinsic defect levels, we also did a comparison by using different calculation method, and a similar bandgap dependence of the defect levels was obtained. By comparing the doing induced defect levels with that of the intrinsic polarons, we found these defect levels are similar to that of electron polaron. This result agrees with the above observation in atomic configuration, which clearly shows the formation of electron polarons. These unoccupied defect levels are close to CBM, forming deep accepting levels. In addition, the number of defect levels is also consistent with the conclusion of atomic configuration that this number is equal to number of additional valence electrons of the dopant compared to Li atom.

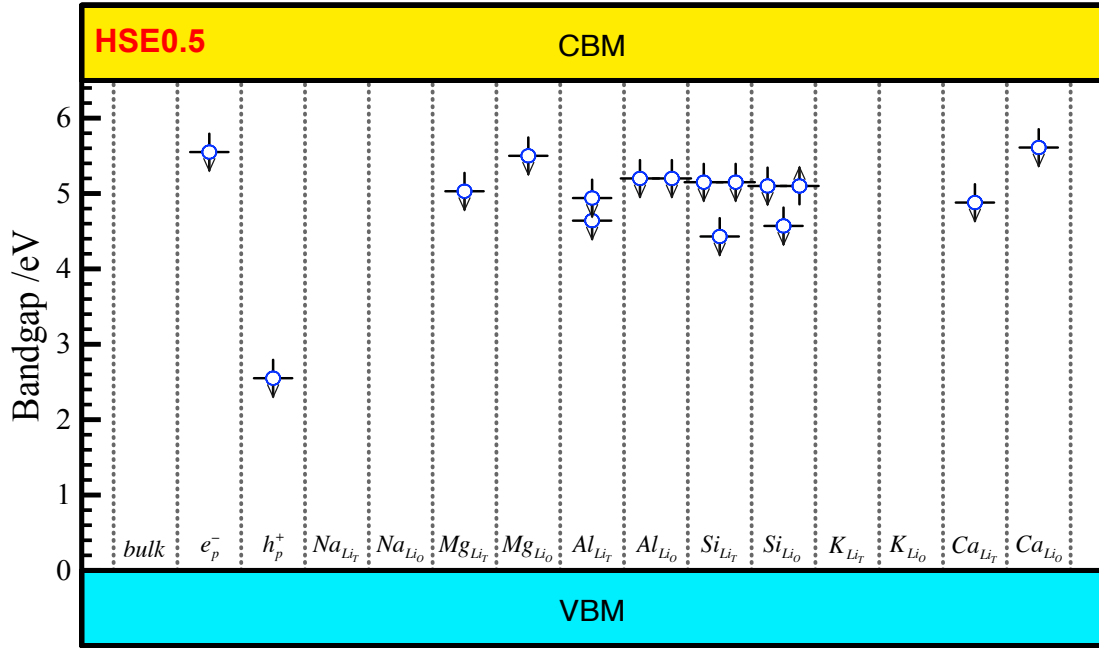


Fig. 5.5: Defect levels of different metal/semimetal doping as compared to the bandgap of bulk  $\text{Li}_2\text{O}_2$ , as well as the defect level of electron and hole polarons. The open circles indicate the unoccupied states. The arrowheads show the spin-up and spin-down states.

Defect type	HSE-0.5/eV
$e_p^-$	5.49
$h_p^+$	2.44
$\text{Na}_{\text{Li}_T}$	-
$\text{Na}_{\text{Li}_O}$	-
$\text{Mg}_{\text{Li}_T}$	5.03
$\text{Mg}_{\text{Li}_O}$	5.50
$\text{Al}_{\text{Li}_T}$	4.64/4.94
$\text{Al}_{\text{Li}_O}$	5.20/5.20
$\text{Si}_{\text{Li}_T}$	4.43/5.15/5.15
$\text{Si}_{\text{Li}_O}$	4.57/5.10/5.10
$\text{K}_{\text{Li}_T}$	-
$\text{K}_{\text{Li}_O}$	-
$\text{Ca}_{\text{Li}_T}$	4.88
$\text{Ca}_{\text{Li}_O}$	5.61

Table. 5.2: Defect levels of different metal/semimetal doping as referred to the VBM of  $\text{Li}_2\text{O}_2$ .



### 5.3.1.4 Si doping

From the above results and discussion, we know that the most important conclusion related to metal/semimetal doping in  $\text{Li}_2\text{O}_2$  is the formation of electron polarons due to electron donation from the additional valence electrons of doping atom to surrounding O-O peroxide anions. Thus from the result of formation energy and defect levels, the most promising doping element in  $\text{Li}_2\text{O}_2$  is Si, which has the lowest formation energy and forms multi-defect levels. In Fig. 5.6 we plotted the band decomposed charge density corresponding to the defect levels of Si doping. From the shape of the defect states, we can clearly see the O  $p_z$  shaped wavefunctions next to the Si atoms. This observation again confirms the electron donation from Si to O  $p_z$  states, thus the remaining unoccupied O  $p_z$  states form the gap states.

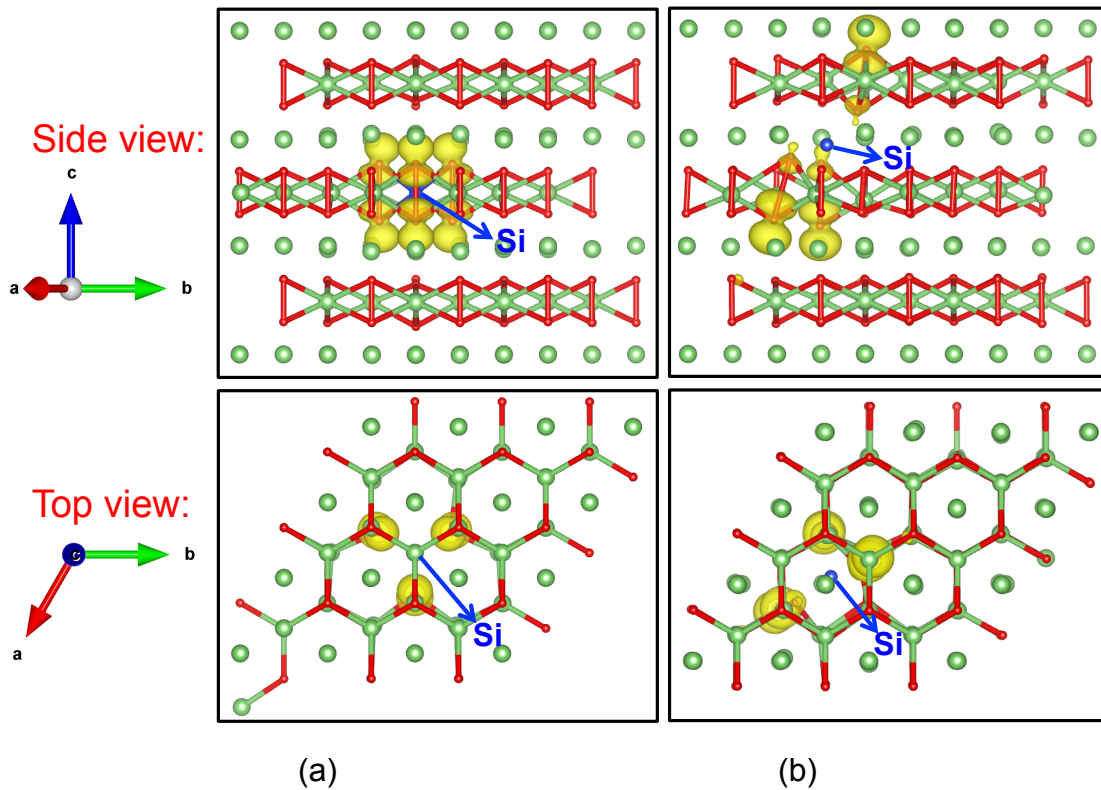


Fig. 5.6: Band decomposed charge density corresponding to the defect levels of Si doping in  $\text{Li}_2\text{O}_2$  at (a) T-site and (b) O-site Li. The blue atom indicates the substitutional Si atom.

Despite the negative formation energy of Si doping, the highly localized defect states as well as the deep acceptor levels suggest that Si doping might not be

an effective way to improve the conductivity of  $\text{Li}_2\text{O}_2$ . However, due to the fact that defect levels highly depend on the calculation method, here we calculation the DOS for Si doing with different methods.

Fig. 5.7 presents a direct comparison by using PBE, and HSE with 25% and 50% exact exchange respectively. This results clearly reveals the bandgap dependence of the doing induced gap states. By PBE, the resulted gap states are just above the valence band, indicating the valence electrons can be easily excited to this conduction band and result in electron conductivity. However, when the bandgap is opened by using HSE, these gap states will gradually shifted to higher energy levels. Under our HSE-GW0 predicted bandgap of more than 6.5eV, these levels becomes too far from the valence band to be able to improve the conductivity.

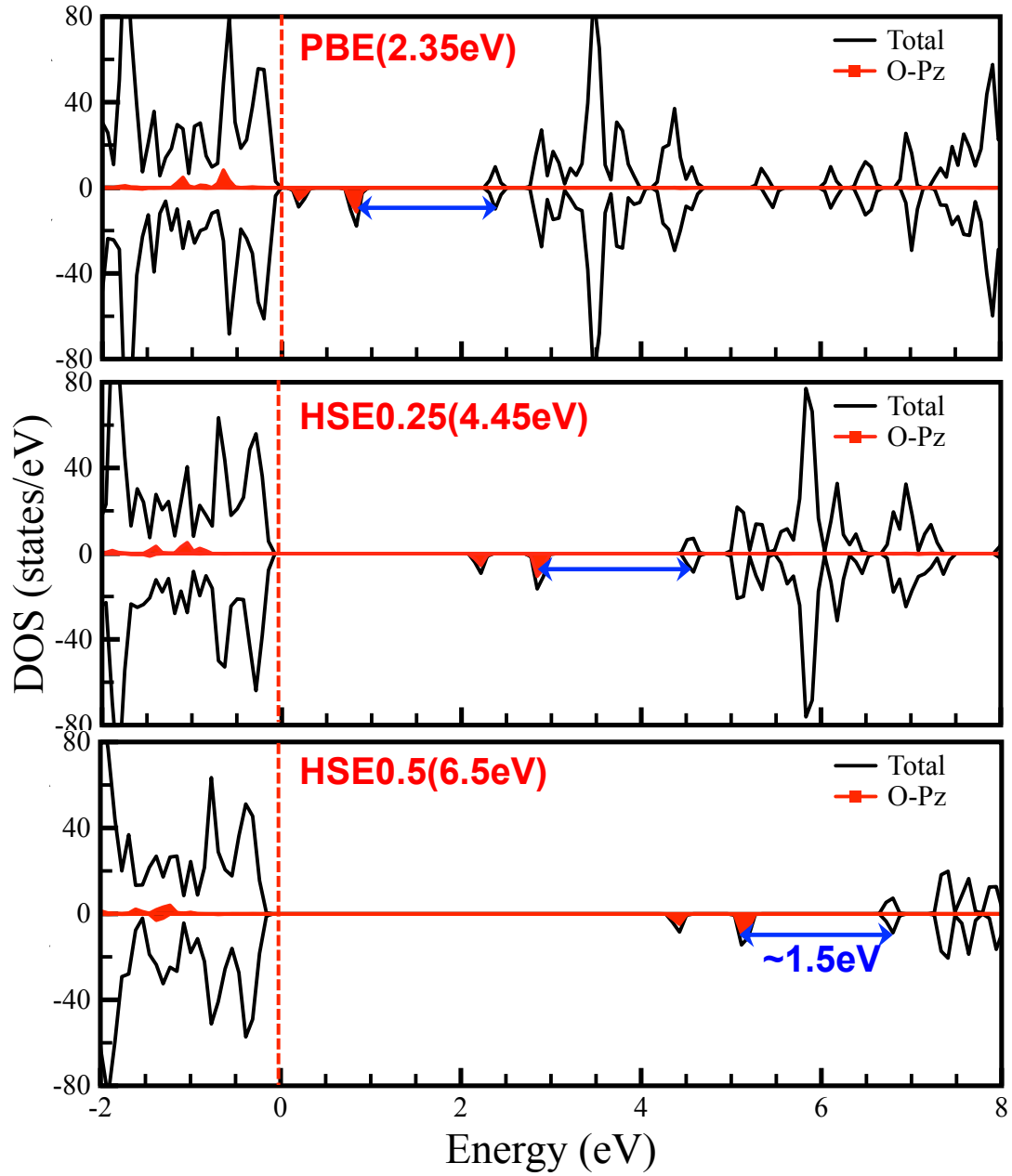


Fig. 5.7: Total and projected DOS for Si doping at T-site Li calculated by using different methods. The red dashed line indicates the position of Fermi level. The black line is the total DOS of the system, and the red line shows the DOS projected on the O pz states of the surrounding electron polarons.

### 5.3.2 Hydrogen impurity in $\text{Li}_2\text{O}_2$

#### 5.3.2.1 Formation energy

The formation energy of interstitial hydrogen in  $\text{Li}_2\text{O}_2$  was calculated as putting one hydrogen atom into a  $3 \times 3 \times 2$   $\text{Li}_2\text{O}_2$  supercell using the following

formula:

$$E_f(H_i^q) = E_{tot}(H_i^q) - E_{tot}(bulk) - \mu_H + q\varepsilon_F, \quad (\text{Eq. 5.2})$$

And the substitutional hydrogen in  $\text{Li}_2\text{O}_2$  was modeled by replacing one Li atom, one O atom or one O-O dimer with one H atom, forming HLi, HO and HO<sub>2</sub> respectively. Their formation energies can be calculated based on the following formulas:

$$E_f(H_{Li}^q) = E_{tot}(H_{Li}^q) - E_{tot}(bulk) + \mu_{Li} - \mu_H + q\varepsilon_F, \quad (\text{Eq. 5.3})$$

$$E_f(H_O^q) = E_{tot}(H_O^q) - E_{tot}(bulk) + \mu_O - \mu_H + q\varepsilon_F, \quad (\text{Eq. 5.4})$$

$$E_f(H_{O_2}^q) = E_{tot}(H_{O_2}^q) - E_{tot}(bulk) + 2\mu_O - \mu_H + q\varepsilon_F, \quad (\text{Eq. 5.5})$$

$\mu_H$ ,  $\mu_{Li}$  and  $\mu_O$  are the chemical potentials of H, Li and O respectively.  $\varepsilon_F$  is the electron chemical potential in referenced to the valence band maximum  $\varepsilon_{VBM}$  of the bulk phase  $\text{Li}_2\text{O}_2$ . Therefore, the  $\varepsilon_F$  can vary from zero to the bandgap of  $\text{Li}_2\text{O}_2$ .

It is worth mentioning that these chemical potentials depend on experimental conditions during growth or annealing. In other words, they are constrained by upper and lower bounds, i.e., ranging from O-rich to O-poor conditions. In this study, the chemical potentials of  $\mu_{Li}$ ,  $\mu_O$  and  $\mu_H$  are referenced to the energy per atom of bulk lithium metal, an isolated oxygen and hydrogen molecule respectively. They are subjected to the upper bounds  $\mu_O \leq 0$  (O-rich limit),  $\mu_{Li} \leq 0$  (O-poor limit) and  $\mu_H \leq 0$  (H-rich limit). The chemical potential of  $\mu_{Li}$  and  $\mu_O$  should satisfy the following expression:

$$2\mu_{Li} + 2\mu_O = \Delta H_f(\text{Li}_2\text{O}_2), \quad (\text{Eq. 5.6})$$

where  $\Delta H_f(\text{Li}_2\text{O}_2) = -6.57 \text{ eV}^2$  is the experimental formation enthalpy of  $\text{Li}_2\text{O}_2$ . In addition, the existence of hydrogen introduces additional constraints to exclude the formation of possible secondary phases  $\text{H}_2\text{O}$ ,  $\text{H}_2\text{O}_2$  and  $\text{LiH}$ :

$$2\mu_H + \mu_O \leq \Delta H_f(\text{H}_2\text{O}), \quad (\text{Eq. 5.7})$$

$$2\mu_H + 2\mu_O \leq \Delta H_f(\text{H}_2\text{O}_2), \quad (\text{Eq. 5.8})$$

$$\mu_{\text{Li}} + \mu_H \leq \Delta H_f(\text{LiH}), \quad (\text{Eq. 5.9})$$

where  $\Delta H_f(\text{H}_2\text{O}) = -2.51 \text{ eV}$ ,  $\Delta H_f(\text{H}_2\text{O}_2) = -1.94 \text{ eV}$  and  $\Delta H_f(\text{LiH}) = -1.20 \text{ eV}$ <sup>3</sup> are the experimental formation enthalpy of  $\text{H}_2\text{O}$ ,  $\text{H}_2\text{O}_2$  in gas phase and bulk  $\text{LiH}$ , respectively. In Fig. 5.8 we plotted the chemical potential region that satisfies the above equations. In the following discussions regarding the formation energies of hydrogen impurities in  $\text{Li}_2\text{O}_2$ , we considered both the O-rich (Li-poor) and O-poor (Li-rich) conditions (A and B points as shown in Fig. 5.8 and the chemical potential of hydrogen was then set to be the highest value possible (H-rich) as calculated according to the constraints of the formation of  $\text{H}_2\text{O}$ ,  $\text{H}_2\text{O}_2$  and  $\text{LiH}$ .

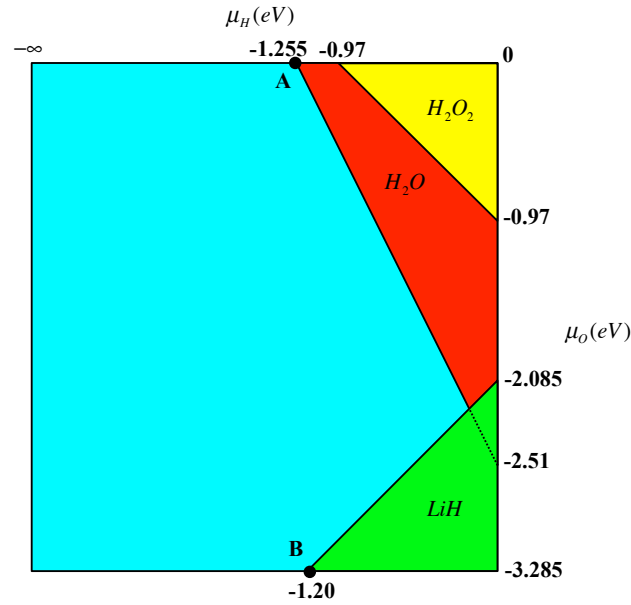


Fig. 5.8: Thermodynamic stable range for  $\text{Li}_2\text{O}_2$  is shown in the cyan region. Outside of this region show the existence of possible secondary phases of  $\text{H}_2\text{O}$ ,  $\text{H}_2\text{O}_2$  and  $\text{LiH}$ . The entire region of  $\mu_O$  is from zero to  $-3.29 \text{ eV}$ , and for  $\mu_H$  is the region below  $-1.20 \text{ eV}$ . The representative points A and B indicate the O-rich and O-poor limits used in our calculation of the formation energy.

In Fig. 5.9, we plotted the formation energies of all the interstitial and substitutional hydrogen in  $\text{Li}_2\text{O}_2$  as a function of Fermi-level under both O-rich and O-poor conditions.

Our calculation results demonstrated that under both conditions, interstitial

hydrogen defects have much lower formation energy than substitutional ones. The negative formation energy of interstitial hydrogen indicates it can be quite easily incorporated into  $\text{Li}_2\text{O}_2$ . The transition levels of  $\varepsilon_{H_i}(+/0)$  and  $\varepsilon_{H_i}(0/-)$  are around 1.52 eV and 1.94 eV above  $\varepsilon_{VBM}$  respectively, which makes  $H_i^0$  only exist in a short energy range around 0.4 eV. Due to large bandgap of  $\text{Li}_2\text{O}_2$  by our hybrid DFT calculation, the above transition levels located quite deep within band gap, resulting in  $H_i$  behaviors as both a deep donor and acceptor, not possible to be an active conductivity source. In contrast, the interstitial hydrogen atom will certainly contribute to compensate the prevailing conductivity of  $\text{Li}_2\text{O}_2$ ; i.e.,  $H_i$  acts as a donor in p-type  $\text{Li}_2\text{O}_2$  and as an acceptor in n-type  $\text{Li}_2\text{O}_2$ . In addition, our calculation also predicts that for  $H_i^0$  and  $H_i^{-1}$  there are two stable configurations for each, and the energy difference is around 40meV as indicated by the dashed line in Fig. 5.9. This result corresponds to the different binding site of hydrogen with  $\text{Li}_2\text{O}_2$ , and would be discussed in detail in the next section.

For substitutional hydrogen in  $\text{Li}_2\text{O}_2$ , under O-rich condition hydrogen substitution of lithium (both  $H_{Li\_T}$  and  $H_{Li\_O}$ ) is much more stable than that of oxygen (both  $H_O$  and  $H_{O_2}$ ), and as the chemical potential of oxygen decreases to O-poor condition the lithium substitution and oxygen single atom substitution are comparable. The extremely high formation energy of oxygen di-atom substitution under both conditions indicates it is hardly to happen. The substitution of lithium at the two symmetric distinguish positions has similar energies, with  $H_{Li\_T}$  is less than 30meV more stable than  $H_{Li\_O}$ , and this result is consistent with the previous calculation of native lithium vacancy.<sup>4</sup> The dominating charge state for both  $H_{Li\_T}$  and  $H_{Li\_O}$  is the neutral state. Note that the formation energy of  $H_{Li}$  gradually decreases when the Fermi-level is close to  $\varepsilon_{VBM}$  and  $\varepsilon_{CBM}$ . This implies that substitution of Li by hydrogen would be a possible source of compensation in both p-type and n-type  $\text{Li}_2\text{O}_2$ , especially in p-type doping case. The neutral charge state of  $H_O$  and  $H_{O_2}$  is never stable within all energy range, resulting in only one transition level from +1 to -1 located around 4.18 eV and 2.97 eV respectively. The origin of this “negative-U” behavior lies in the large differences in local lattice relaxations for different charge states. This result further reveals that substitution of oxygen by

hydrogen will also compensate with the prevailing conductivity of  $\text{Li}_2\text{O}_2$ .

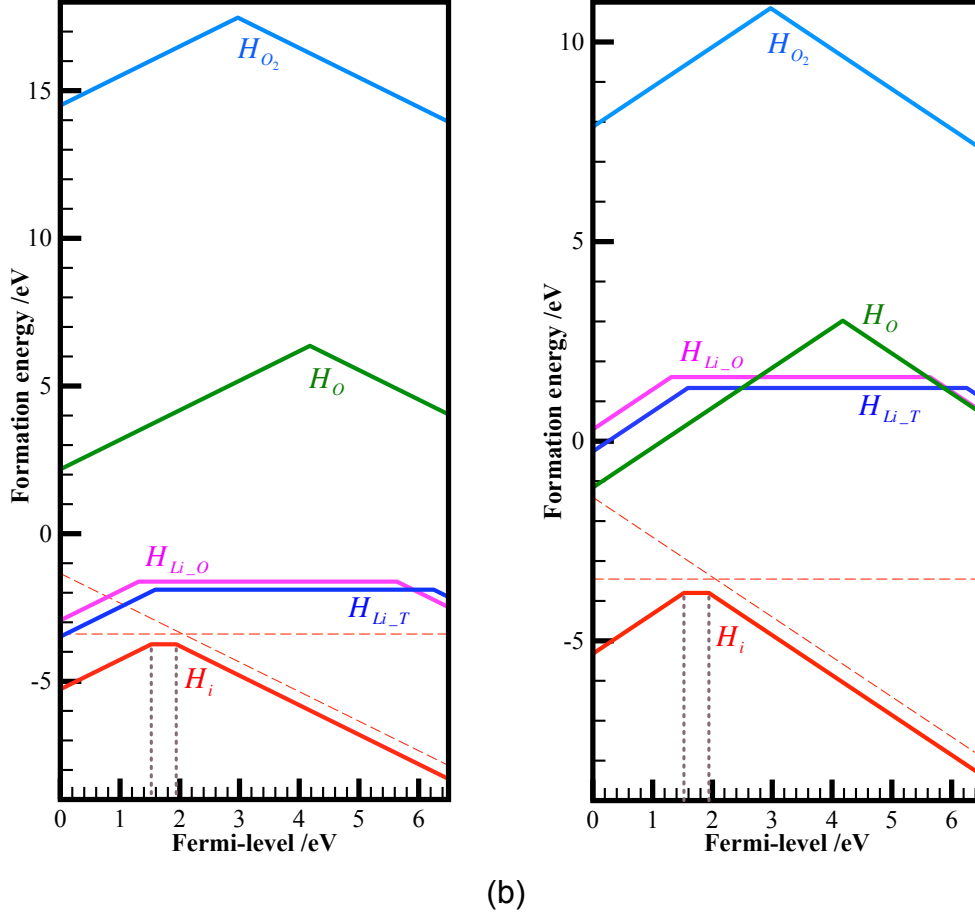


Fig. 5.9: Formation energies of interstitial and substitutional hydrogen in  $\text{Li}_2\text{O}_2$  as a function of Fermi energy under (a) extreme O-rich and (b) extreme O-poor conditions. The dashed lines in both (a) and (b) indicate additional metastable configurations corresponding to neutral and negative interstitial hydrogen in  $\text{Li}_2\text{O}_2$ . The  $\varepsilon_{VBM}$  is set to be zero.

### 5.3.2.2 Atomic bonding configuration

In order to further investigate the bonding between hydrogen and the host material  $\text{Li}_2\text{O}_2$ , we summarized the optimized atomic configurations for interstitial H and H substitution of O in Fig. 5.10, together with the bond length and Bader charge<sup>5</sup> for  $H_i$  and  $H_O$  in Table. 5.3.

From the calculated formation energy and atomic configurations,  $H_i^0$  and  $H_i^-$  have two stable configurations respectively. More specifically, hydrogen may occupy both the BC and AB/AB' sites of  $\text{O}_2^{2-}$  peroxide anion since the calculated formation energies of AB and AB' are quite similar, in this study we

will only talk about AB). This results in three-center bond configurations of O-H-O and O-O-H with an elongated O-O bond length as summarized in Fig. 5.10 and Table. 5.3. For  $H_i^+$ , the bonding between  $O_2^{-2}$  and  $H^+$  forms two quite similar configurations depending on the inter- or intra-layer position of H related to two O-O layers, which can be reflected by the slightly difference in the bond lengths of O-O and O-H as well as the bond angle of O-O-H (see Table. 5.3). Both configurations are similar to that in  $H_2O_2$  molecule. For  $H_O^q$ , the bonding between H and O forms H-O like species at different charge states, and the O-H bond length also varies with respect to the charge states (see Table. 5.3).

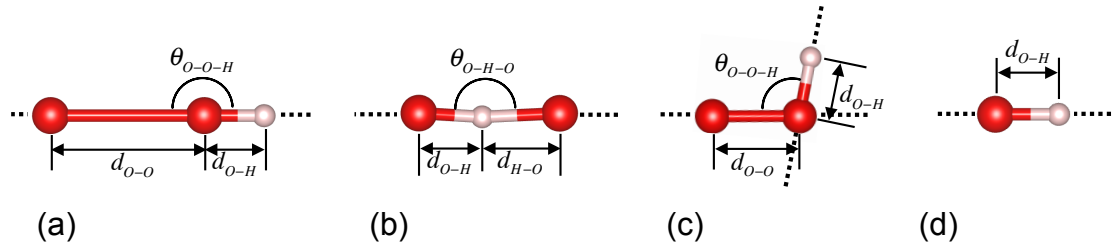


Fig. 5.10: Atomic bonding configuration for neutral and negative interstitial H at (a) O-O antibonding site ( $H_i^0/H_i^{-1}$ -AB) and (b) O-O bonding center site ( $H_i^0/H_i^{-1}$ -BC), (c) positive interstitial H ( $H_i^+$ ) and (d) H substitution at O site ( $H_O^q$ ).



Table. 5.3: Calculated binding site, local atomic configuration and Bader charge for different charge states of  $H_i$  and  $H_o$ . BC/AB/AB' indicate the binding site related to  $\text{O}_2^{-2}$  peroxide anion, and O-H the formation of hydroxyl-like species.  $d_{\text{O-O}}/d_{\text{O-H}}$  denote the O-O/O-H distance, and  $\theta$  is the bond angle of O-H-O or O-O-H depending on the binding site of H. Bader charge gives the charge corresponding to each O/O/H atom.

Defect type	Location	$d_{\text{O-O}}$ /Å	$d_{\text{O-H}}$ /Å	$\theta$ /°	Bader charge /e (O/O/H)
$H_i^+$	AB'	1.47/1.48	0.98/1.00	109.2/101.3	6.73/6.86/0.36
$H_i^0$	BC	2.27	1.26/1.03	166.4	7.02/7.34/0.47
$H_i^0$	AB	2.24	0.96	179.8	6.93/7.47/0.42
$H_i^-$	BC	2.34	1.25/1.09	179.9	7.64/7.61/0.38
$H_i^-$	AB	2.46	0.96	179.9	7.70/7.49/0.43
$H_o^+$	O-H	-	0.97	-	7.47/0.44
$H_o^0$	O-H	-	1.01	-	7.56/0.92
$H_o^-$	O-H	-	2.40	-	7.72/1.82

### 5.3.2.3 Electronic structure

#### 5.3.2.3.1 Interstitial hydrogen ( $H_i^q$ )

The corresponding projected density of states (PDOS) together with the band decomposed charge density for selected energy ranges of  $H_i^0$  and  $H_i^-$  at BC and AB binding sites are plotted in Fig. 5.11. The binding between hydrogen with  $\text{O}_2^{-2}$  peroxide anion in  $\text{Li}_2\text{O}_2$  can be illustrated by the electronic structure. Since the valence and conduction band of  $\text{Li}_2\text{O}_2$  are dominated by the fully occupied antibonding  $\pi^*$  ( $2p_{xy}$ ) orbitals and the empty antibonding  $\sigma^*$  ( $2p_z$ ) orbitals of oxygen respectively,<sup>6</sup> when a hydrogen atom bonds to  $\text{O}_2^{-2}$ , its 1s electron will be donated to O  $\sigma^*$  orbitals. For  $H_i^0$  and  $H_i^-$ , one and two electrons will be transferred from hydrogen respectively, resulting in a partial and full occupation of O  $\sigma^*$  orbitals. This is confirmed by the PDOS of O-H-O and O-O-H configurations as plotted in Fig. 5.11.

In the PDOS of two  $H_i^0$  configurations, we can clearly see that the doping induced empty band gap state of O  $p_z$  orbitals are located around 3.5 eV and 5.0 eV above VBM for each. In the case of  $H_i^-$ , the above empty gap state is further occupied and the shifts to the frontier of valence band. In addition, because the O  $\sigma^*$  orbitals are aligned along the O-O axis, hydrogen will also locate along the O-O axis, either at the BC or AB site, resulting in the configuration of O-H-O or O-O-H. These BC or AB binding position determines electrons from hydrogen will be either shared by both two oxygen atoms or transferred mainly to one of the two oxygen atoms. The partial charge density distribution shown in the inset of Fig. 5.11 clearly reveals these features. In case of O-H-O, the charge densities corresponding to both the unoccupied band gap state in  $H_i^0$  and the fully filled O  $\sigma^*$  orbitals in  $H_i^-$  are located at both of the two oxygen atoms, demonstrating a sharing configuration of electrons. While in case of O-O-H, the charge densities are mainly distributed on the oxygen atom that not directly bonds to H. The stability of these two configurations can be reflected from their formation energy. Since there is only one valence electron for neutral hydrogen atom, a fully donation of this electron to one oxygen atoms to form  $\text{O}^{-2}$ , which is the most stable species of oxygen anion, is supposed to be stable than a partially donation to both two oxygen atoms. In contrast, for hydrogen anion, as two electrons are available, both oxygen atoms have the potential to get one electron and be further reduced to  $\text{O}^{-2}$ . Thus the O-H-O configuration provides a much easier way to donate two electrons to both oxygen atoms than O-O-H does. Given that there is no electron for  $H_i^+$ , the bare proton will bond to  $\text{O}_2^{-2}$  anion, causing a portion of hybridization between hydrogen and  $\text{O}^{-2}$  (see the Bader charge analysis in Table. 5.3). Moreover, due to the proton and  $\text{O}_2^{-2}$  species within  $\text{Li}_2\text{O}_2$  are quite similar to the species in hydrogen peroxide, the bond length and angle of this O-O-H part are also similar to that in  $\text{H}_2\text{O}_2$ .

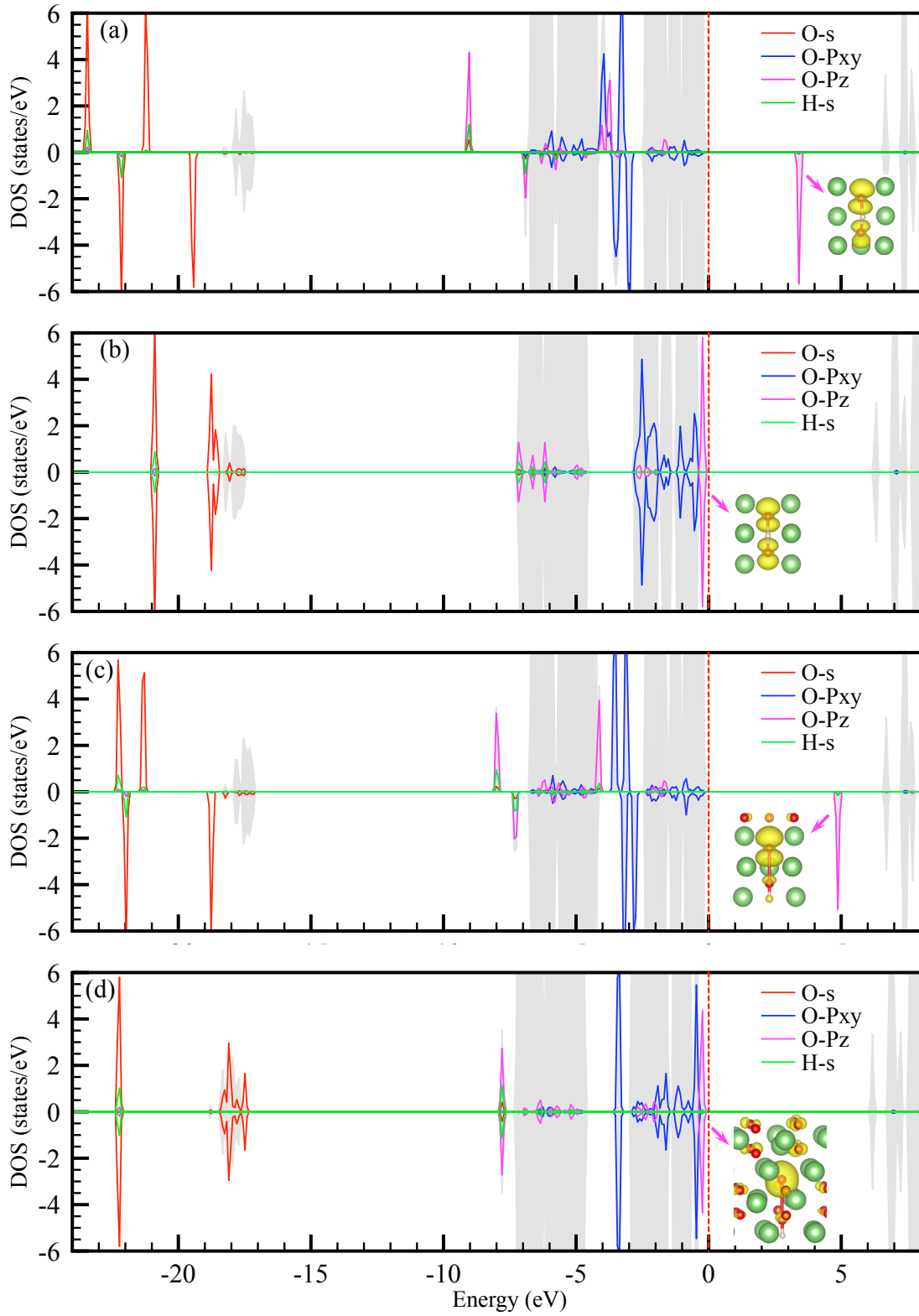


Fig. 5.11: Projected density of states (PDOS) on oxygen and hydrogen atom respectively for  $H_i^0$  and  $H_i^-$  with H atom located at different binding sites: (a)  $H_i^0 - BC$ , (b)  $H_i^- - BC$ , (c)  $H_i^0 - AB$ , (d)  $H_i^- - AB$ . O refers to the two oxygen atoms bonding to H. The shadow parts show the states from all O  $p_{xy}$  and O  $p_z$  in the system as a background to indicate the bulk

band property. The inserts are the corresponding decomposed band charge density for the gap states and the fully filled O  $\sigma^*$  orbitals.

Considering the calculation effect, we compared the defect levels and transition levels calculated by using different methods, and the results are shown in Fig. 5.12. From this figure, it is clearly to see that the transition levels are high depended on the calculation method, while the transition levels between  $H_i^+$  and  $H_i^0$  are almost constant.

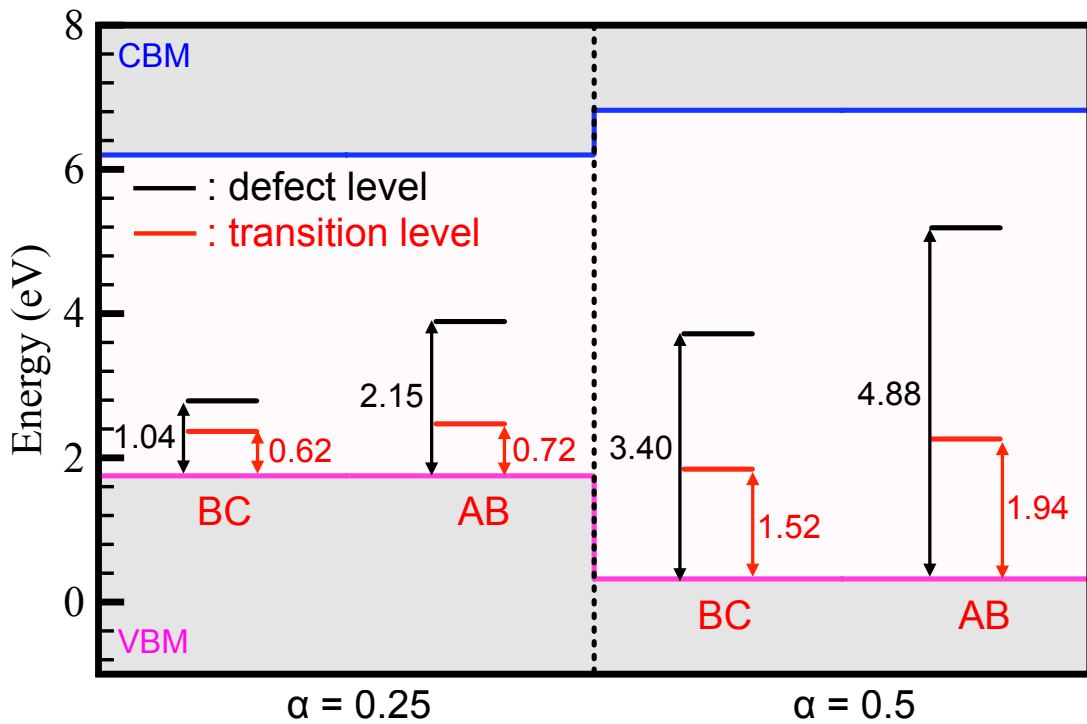


Fig. 5.12: Defect levels for  $H_i^0$  and transition levels  $\epsilon(+/0)$  for interstitial hydrogen at BC and AB bonding site respectively, as calculated by using different fractions of exact exchange in HSE.

#### 5.3.2.3.2 H substitution of Li ( $H_{Li}^q$ )

Previous calculations have found that the dominantly native point defect in  $\text{Li}_2\text{O}_2$  is  $V_{Li}^-$ , and our results show that the atomic configuration of  $H_{Li}^0$  is corresponding to complexes of  $V_{Li}^-$  and  $H_i^+$ , with hydrogen forms the same configuration as that of  $H_i^+$  with one surrounding  $O_2^{-2}$  of Li vacancy. By

defining the binding energy  $E_b$  as the difference in formation energies of the isolated constituents and the complexes,<sup>7</sup> we can obtain the binding energy for  $H_{Li}^0 \rightarrow V_{Li}^- + H_i^+$  using the following formula:

$$\begin{aligned} E_b &= E_f(V_{Li}^-) + E_f(H_i^+) - E_f(H_{Li}^0) \\ &= E_{tot}(V_{Li}^-) + E_{tot}(H_i^+) - E_{tot}(H_{Li}^0) - E_{tot}(bulk) \end{aligned} \quad (\text{Eq. 5.10})$$

We got  $E_b \sim 1.0$  eV and 0.8 eV for T- and O-site substitution respectively, indicating the tightly binding between interstitial hydrogen and lithium vacancy. Similarly, the local atomic structure of positive  $H_{Li}^+$  shows a further binding of  $H_{Li}^0$  with one hole polaron ( $h_p^+$ ).

$$\begin{aligned} E_b &= E_f(H_{Li}^0) + E_f(h_p^+) - E_f(H_{Li}^+) \\ &= E_{tot}(H_{Li}^0) + E_{tot}(h_p^+) - E_{tot}(H_{Li}^+) - E_{tot}(bulk) \end{aligned} \quad (\text{Eq. 5.11})$$

The binding energies are calculated to be  $\sim 0.6$  eV for T-site, and 0.3 eV for O-site, nearly one half of that between pure lithium vacancy and hole polaron,<sup>7</sup> which means that the exists of hydrogen will weaken the interaction between lithium vacancy and hole in  $\text{Li}_2\text{O}_2$ .

#### 5.3.2.3.3 H substitution of O ( $H_O^q$ )

The substitutional hydrogen on a single oxygen site results in the formation of hydroxyl-like defects (H-O) (see Fig. 5.10). Previous studies on the intrinsic defect properties of  $\text{Li}_2\text{O}_2$  have pointed out that neutral oxygen vacancy is the most stable point defect in  $\text{Li}_2\text{O}_2$ . The reason is attributed to that removing one neutral oxygen atom from  $O_2^{-2}$  will result in the formation of  $O^{-2}$  which is energetically favorable.<sup>4</sup> Our Bader charge analyses also reveal that for O-H formed at different charge states, the electron associated with oxygen atom is almost constant and the changing of charge state mainly happens on hydrogen (see **Table. 5.3**). The bonding between  $H^q$  and  $O^{-2}$  can be understood by their molecular orbitals. Fig. 5.13 plotted the molecular orbitals

between the neutral hydrogen atom and the  $\text{O}^{-2}$  species, and the bonding mechanism can be easily understood.

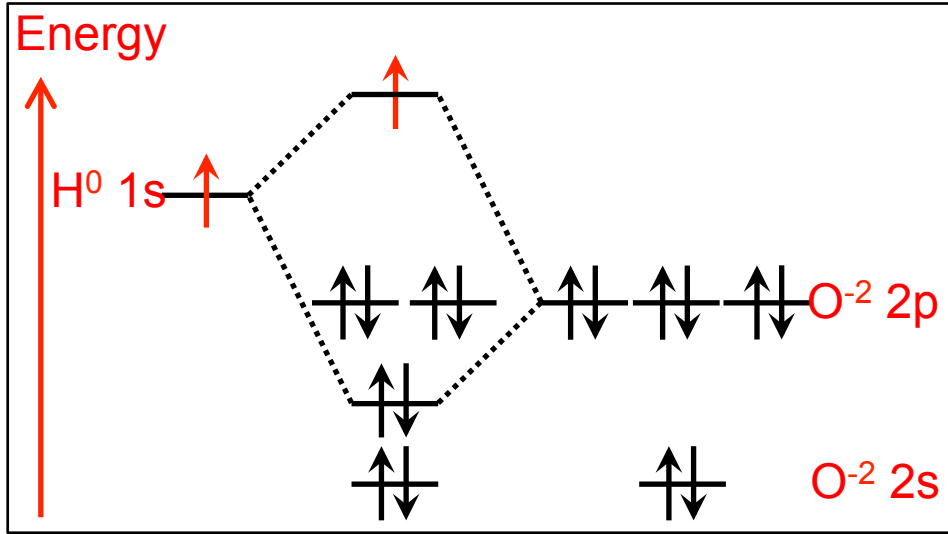


Fig. 5.13: Molecular orbitals between  $\text{H}^0$  and  $\text{O}^{-2}$  illustrating the binding mechanism.

#### 5.3.2.3.4 H substitution of di-O ( $\text{H}_{\text{O}_2}^q$ )

From the previous calculations, we know that the formation of neutral di-O vacancy will lead to the formation of two coupled electrons at the vacancy site. Thus in this part, we found that the substitution of di-O by hydrogen results in the complexes of vacancy electrons with the H. This process can be explained by the following formulas:

$$\text{V}_{\text{O}_2}^0 \rightarrow e_{\text{O}_2}^{-2} \quad (\text{Eq. 5.12})$$

$$\text{H}_{\text{O}_2}^+ \rightarrow e_{\text{O}_2}^{-2} + \text{H}^+ \rightarrow \text{H}_{\text{O}_2}^- \quad (\text{Eq. 5.13})$$

$$\text{H}_{\text{O}_2}^0 \rightarrow e_{\text{O}_2}^{-2} + \text{H}^0 \rightarrow \text{H}_{\text{O}_2}^- + e_p^- \quad (\text{Eq. 5.14})$$

$$\text{H}_{\text{O}_2}^- \rightarrow e_{\text{O}_2}^{-2} + \text{H}^- \rightarrow \text{H}_{\text{O}_2}^- + 2e_p^- \quad (\text{Eq. 5.15})$$

In addition, except for the above configurations, we also find a kind of unstable doping positions with  $\text{H}^0/\text{H}^-$  located at the high symmetric sites in  $\text{Li}_2\text{O}_2$ , including the body center of O-O trigonal prism (in case of  $\text{H}_i^0$ ,  $\text{H}_i^-$  and  $\text{H}_{\text{Li}_T}^-$ ) / O-O octahedral (in case of  $\text{H}_{\text{Li}_O}^-$ ) /  $\text{Li}^+$  trigonal prism (in case of  $\text{H}_{\text{O}_2}$ ).

All these high symmetric sites are found to be capable to hold one neutrally or negatively charged hydrogen, resulting in a metastable hydrogen multiband center. However due to the formation energies of these configurations are quite high, they may not exist under equilibrium conditions.

## 5.4 Conclusions

In this part of study, we performed a systematical calculation for both the effect of metal/semimetal doping and the behavior of hydrogen impurity in  $\text{Li}_2\text{O}_2$ . The calculation results show that:

- 1) For metal/semimetal doping in  $\text{Li}_2\text{O}_2$ ,
  - Multi-electron polarons are formed next to the doping atom due to electron donation from the additional valence electrons to the antibonding O-Pz states of O-O peroxide anion. And the formation of electrons polarons will stabilize the doping system;
  - Highly localized defect levels form deep acceptor levels, and can hardly be effective to improve the conductivity of  $\text{Li}_2\text{O}_2$ ;
  - Defect levels are highly depended on the calculated bandgap. Upon bandgap opening, these states shifted to higher energy levels.
- 2) For hydrogen atom as an impurity in  $\text{Li}_2\text{O}_2$ ,
  - Hydrogen atom can be easily incorporated into  $\text{Li}_2\text{O}_2$  as an interstitial impurity. The bonding between interstitial hydrogen and  $\text{O}_2^{-2}$  peroxide anion results in electron donation from H 1s to O-pz orbital to form a three-center bond of O-H-O or O-O-H.
  - Hydrogen substitution of lithium and oxygen forms complexes of hydrogen with negative lithium vacancy and the hydroxyl-like species, respectively.

- Both types of hydrogen impurities electrically counteract with the prevailing conductivity of  $\text{Li}_2\text{O}_2$ , making it an unwanted impurity in the application of LAB.

Thus so far, our calculation proposed that doing in  $\text{Li}_2\text{O}_2$  will not be a wise strategy to improve its conductivity. Some alternative methods, like the interface induced conductivity, are needed to be further investigated.



## REFERENCES

1. V. Timoshevskii, Z. Feng, K. H. Bevan, J. Goodenough, and K. Zaghib, *Appl. Phys. Lett.*, 2013, **103**.
2. M. D. Radin, J. F. Rodriguez, F. Tian, and D. J. Siegel, *J. Am. Chem. Soc.*, 2012, **134**, 1093–1103.
3. A. Andreasen and R. D. M. R. D. Risø National Lab, *Predicting Formation Enthalpies of Metal Hydrides*, 2004.
4. M. D. Radin and D. J. Siegel, *Energy Environ. Sci.*, 2013, **6**, 2370–2379.
5. G. Henkelman, A. Arnaldsson, and H. Jónsson, *Computational Materials Science*, 2006, **36**, 354–360.
6. J. Kang, Y. S. Jung, S.-H. Wei, and A. C. Dillon, *Phys. Rev. B*, 2012, **85**, 035210.
7. J. B. Varley, V. Viswanathan, J. K. Nørskov, and A. C. Luntz, *Energy Environ. Sci.*, 2014, **7**, 720.



## Chapter 6 Interfacial properties between Au/Li<sub>2</sub>O<sub>2</sub>

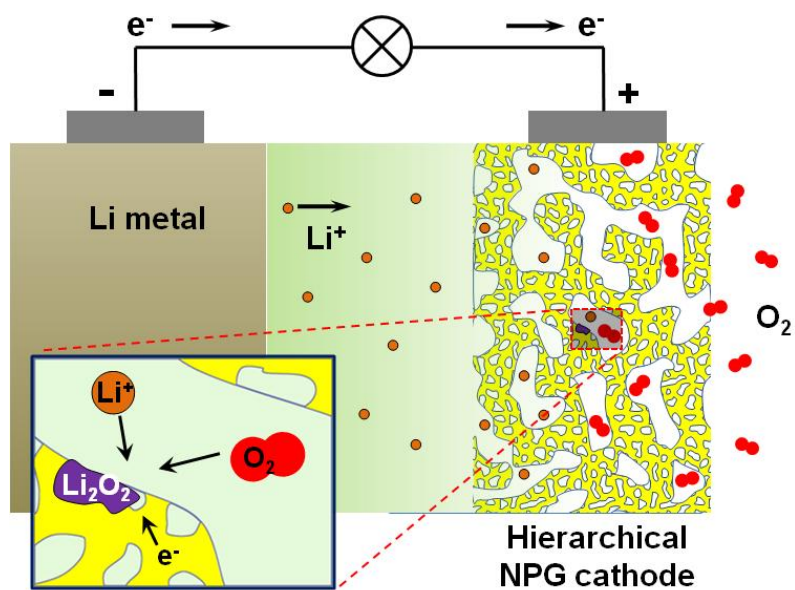
### 6.1 Introduction

#### 6.1.1 Experimental background

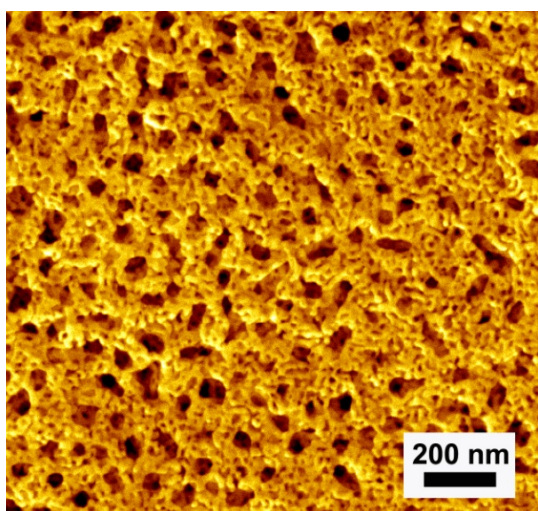
Here as a relatively separate part of study, we present the calculation of interfacial properties between Au and Li<sub>2</sub>O<sub>2</sub>. This study is motivated by the real experimental condition that Au is usually used as the electrode for cathode in LAB.

Fig. 6.1 gives an experimental setup of LAB with hierarchical nanoporous gold (NPG) as the electrode, together with the SEM/TEM characterization of the electrode after discharge and the electrochemical test results of the battery. As we know, during the discharge process, Li<sup>+</sup> and O<sub>2</sub> reacts on the cathode and Li<sub>2</sub>O<sub>2</sub> is formed on the surface of electrode. SEM and TEM results confirmed the formation of Li<sub>2</sub>O<sub>2</sub>. The charge and discharge potentials of this battery indicate a quite low overpotential compared to batteries with other types of electrode. The cycling test also demonstrated that the stability of this battery can maintain this low overpotential for more than 100 cycles.

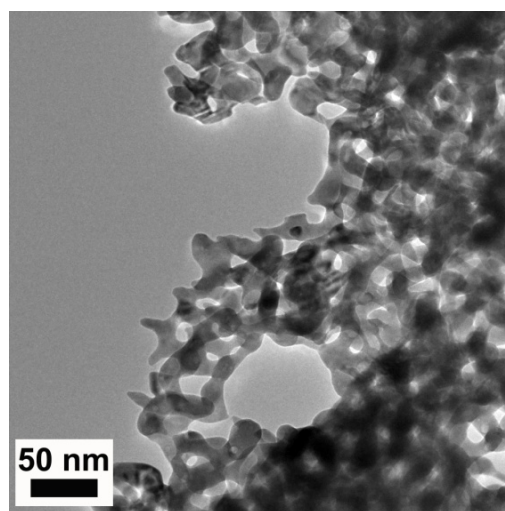
Moreover, based on our background introduction, the performance of LAB is highly controlled by the charge transfer efficiency within the battery. In the previous calculations, we focused on the calculation of charge transport mechanism within bulk Li<sub>2</sub>O<sub>2</sub>. However, except for the bulk conductivity, charge transfer between the electrode and Li<sub>2</sub>O<sub>2</sub> interface is also essential factor that determines the performance of LAB. The low overpotential and long cycling stability of LAB using hierarchical NPG as electrode are supposed to be closely related to the interfacial property between Au and Li<sub>2</sub>O<sub>2</sub>.



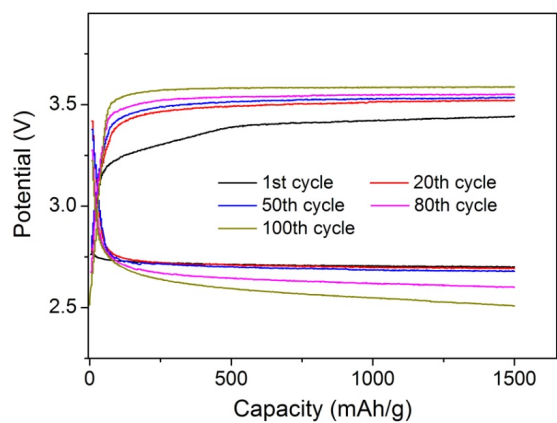
(a)



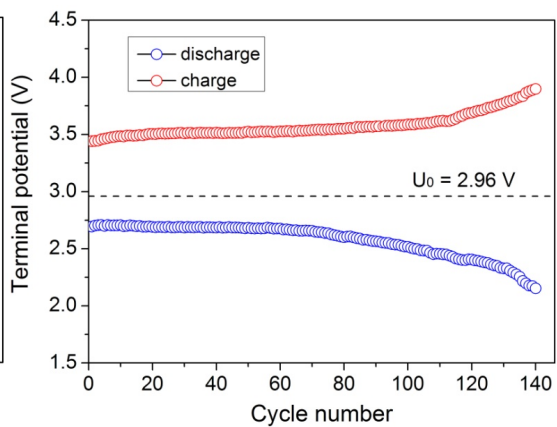
(b)



(c)



(d)



(e)

Fig. 6.1: (a) Schematic draw of the discharge process of LAB using hierarchical nanoporous gold (NPG) as the electrode of LAB. (b) SEM and (c) TEM image of the hierarchical NPG after discharge. Charge and discharge potential of LAB as a function of the (c) operating potential and (d) cycle number of the battery.

## 6.1.2 Interface model between Au and Li<sub>2</sub>O<sub>2</sub>

### 6.1.2.1 Coherent interface model

In the literature studies, there has been some calculation about the contact states induced conductivity in LAB.<sup>1-3</sup> However in these calculations, usually a very simple interface model has been used to discuss the effect of conducting substrate on Li<sub>2</sub>O<sub>2</sub>. The detailed interfacial atomic configuration, charge transfer mechanism, electronic structure as well as the workfunction change upon interface formation, has not yet been systematically investigated. So in this part of study, we will focus on the above interfacial properties between Au and Li<sub>2</sub>O<sub>2</sub>.

As we all know, the most stable surface of Au is the (111) surface, and previous calculations of Li<sub>2</sub>O<sub>2</sub> also proposed that the most stable surface is the (0001).<sup>4,5</sup> So it is straightforward to build the interface structure between Au (111) and Li<sub>2</sub>O<sub>2</sub> (0001) (see Fig. 6.2). From Fig. 6.2, we can see the atomic arrangement on Au (111) and Li<sub>2</sub>O<sub>2</sub> (0001) are identical, showing a typical fcc close packing pattern. Thus a very simple way to build the interface model is to suppose the two phases will form a coherent interface structure. However, expect for the atomic pattern, the lattice misfit is also a very important factor that determines the interface structure. For example, by PBE calculation, the lattice constants of bulk Au and Li<sub>2</sub>O<sub>2</sub> are 4.159 Å and 3.159 Å respectively. The atomic distances between Au and Li atoms, as indicated in Fig. 6.2(b) and (c), are consequently calculated to be  $d_{Au-Au} = 2.94$  Å and  $d_{Au-Au} = 3.16$  Å. Therefore, the misfit is around 7%, which is relatively large for the formation of coherent interface. A more realistic interface model with semicoherent configuration is desired in this study.

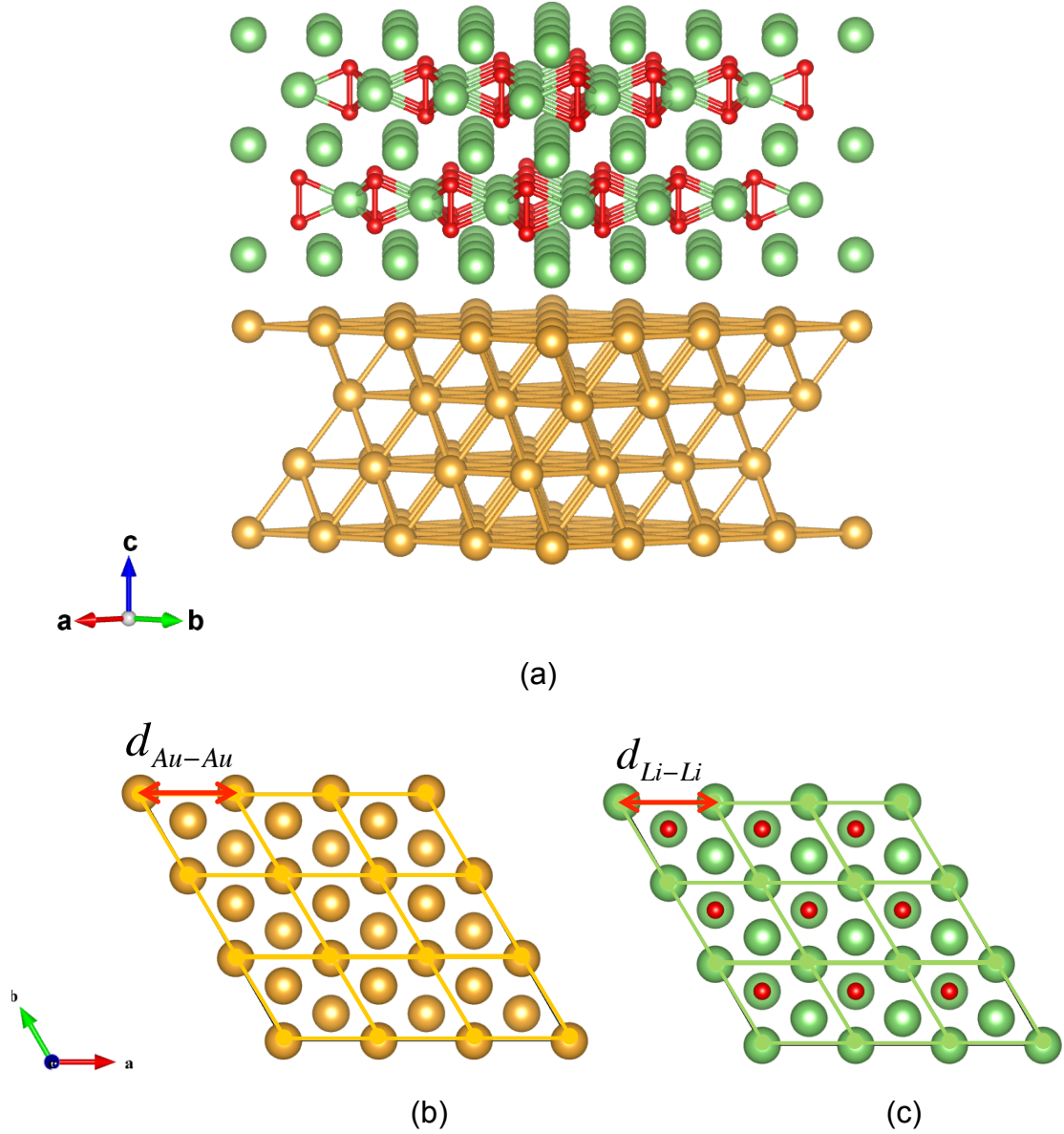


Fig. 6.2: (a) Schematic draw of the interface structure between Au (111) and Li<sub>2</sub>O<sub>2</sub> (0001) surfaces. Atomic pattern on (b) Au (111) and (c) Li<sub>2</sub>O<sub>2</sub> (0001) surfaces.

#### 6.1.2.2 Semicohherent interface model

To describe the semicoherent interface structure formed by two phases, the concept of superlattice can be used. Superlattice means the periodic structure of overlayers, which sit on the surface of the underlying substrate. In order to describe the relative position of overlayer on the surface, the coordination of the overlayer is determined as referenced to the surface unit vectors.

Fig. 6.3 gives an example illustrating the relative orientation of the surface and

superlattice unit vectors. The superlattice can be described by the following matrix notation:

$$\mathbf{a}' = m_{11}\mathbf{a} + m_{12}\mathbf{b} \quad (\text{Eq. 6.1})$$

$$\mathbf{b}' = m_{21}\mathbf{a} + m_{22}\mathbf{b} \quad (\text{Eq. 6.2})$$

$$\mathbf{M} = \begin{pmatrix} m_{11} & m_{12} \\ m_{21} & m_{22} \end{pmatrix} \quad (\text{Eq. 6.3})$$

where,  $\mathbf{a}$  and  $\mathbf{b}$  are the surface unit vectors, and  $\mathbf{a}'$  and  $\mathbf{b}'$  are the unit vectors of the superlattice.

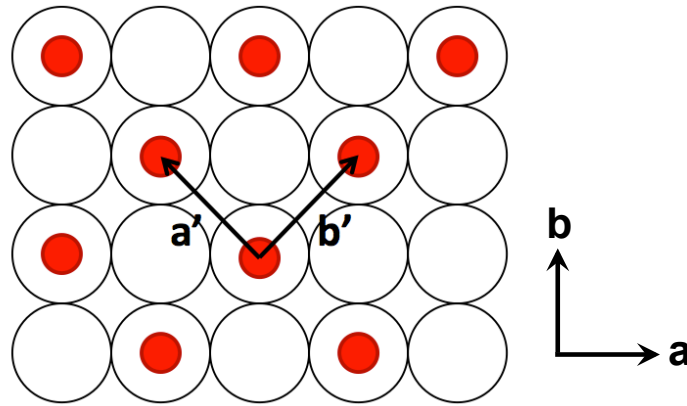


Fig. 6.3: Schematic draw of the overlayer superlattice on a surface. Open circles are the atoms on the surface, and red ones are the atoms on the overlayer.

For the matrix notations, where the diagonal components are zero, we call them primitive overlayers. Then the notation can be simplified to be  $p(m_{11} \times m_{22})$ . And for some other superlattices, the matrix cannot be directly written as primitive notation, but if we rotate the surface unit cell by some degree  $\theta$ , we can get the primitive overlayers. Thus the notation be expressed as  $(m_{11} \times m_{22})R\theta$ .

For the Au/Li<sub>2</sub>O<sub>2</sub> interface system, both of the terminating surfaces of two surfaces have the fcc (111) atomic pattern. So besides the fully coherent interface configuration, rotation between the two phases will result in semicoherent interface configurations, and reduce the interface misfit. In Fig. 6.4, we plotted three types of superlattices for Li<sub>2</sub>O<sub>2</sub> (0001) on top of Au (111), and the corresponding misfit is within 3%.

For superlattice **a**, the matrix notation can be obtained by the following relations:

$$a_1 = 4a - b \quad (\text{Eq. 6.4})$$

$$a_2 = a + 3b \quad (\text{Eq. 6.5})$$

$$M_a = \begin{pmatrix} 4 & -1 \\ 1 & 3 \end{pmatrix} \quad (\text{Eq. 6.6})$$

for **b**,

$$b_1 = 5a - 2b \quad (\text{Eq. 6.7})$$

$$b_2 = 2a + 3b \quad (\text{Eq. 6.8})$$

$$M_b = \begin{pmatrix} 5 & -2 \\ 2 & 3 \end{pmatrix} \quad (\text{Eq. 6.9})$$

and for **c**,

$$c_1 = 6a - b \quad (\text{Eq. 6.10})$$

$$c_2 = a + 5b \quad (\text{Eq. 6.11})$$

$$M_c = \begin{pmatrix} 6 & 5 \\ 1 & 6 \end{pmatrix} \quad (\text{Eq. 6.12})$$

And by using the rotated primitive notation, we can denote the three superlattices as:  $(\sqrt{13} \times \sqrt{13})R13.9^\circ$  for **a**,  $(\sqrt{19} \times \sqrt{19})R23.4^\circ$  for **b** and  $(\sqrt{31} \times \sqrt{31})R8.9^\circ$  for **c**. The corresponding unit cells in Li<sub>2</sub>O<sub>2</sub> is  $(2\sqrt{3} \times 2\sqrt{3})R30^\circ$ ,  $p(4 \times 4)$  and  $(3\sqrt{3} \times 3\sqrt{3})R30^\circ$  respectively (see Fig. 6.5). And the lattice misfit calculated for each is 3.2% for **a**, 1.4% for **b** and 0.2% for **c**. Due the lattice misfit is greatly reduced by formation of superlattices, these three configurations are expected to give a more realistic description of the Au/Li<sub>2</sub>O<sub>2</sub> interface, and will be investigated in detail in the following calculation. Thus in this part of study, we will perform the interface calculation of Au/Li<sub>2</sub>O<sub>2</sub> in the coherent and semicoherent limits respectively, to investigate the interfacial properties related to the conductivity of Li<sub>2</sub>O<sub>2</sub>.



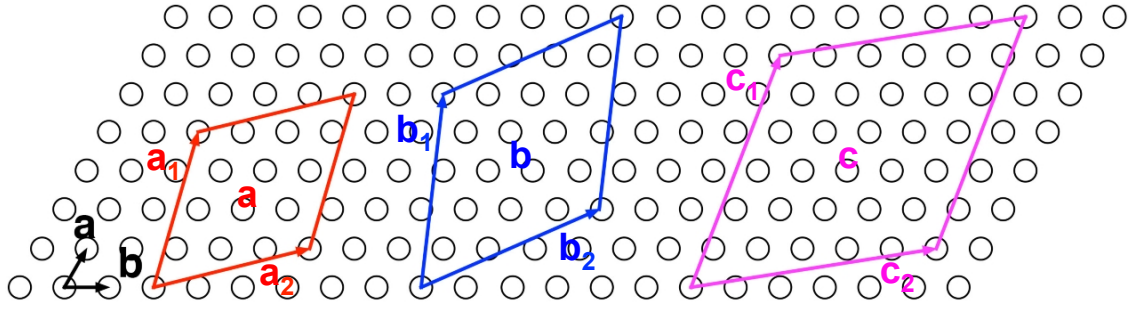


Fig. 6.4: Schematic draw of the top view of three different overlayer superlattices on top of gold (111) surface. The open circles indicate the gold atoms. *a* and *b* are the surface unit vectors of gold (111). *a*, *b* and *c* draw the interfacial unit cell ranges of Li<sub>2</sub>O<sub>2</sub> on top of gold.

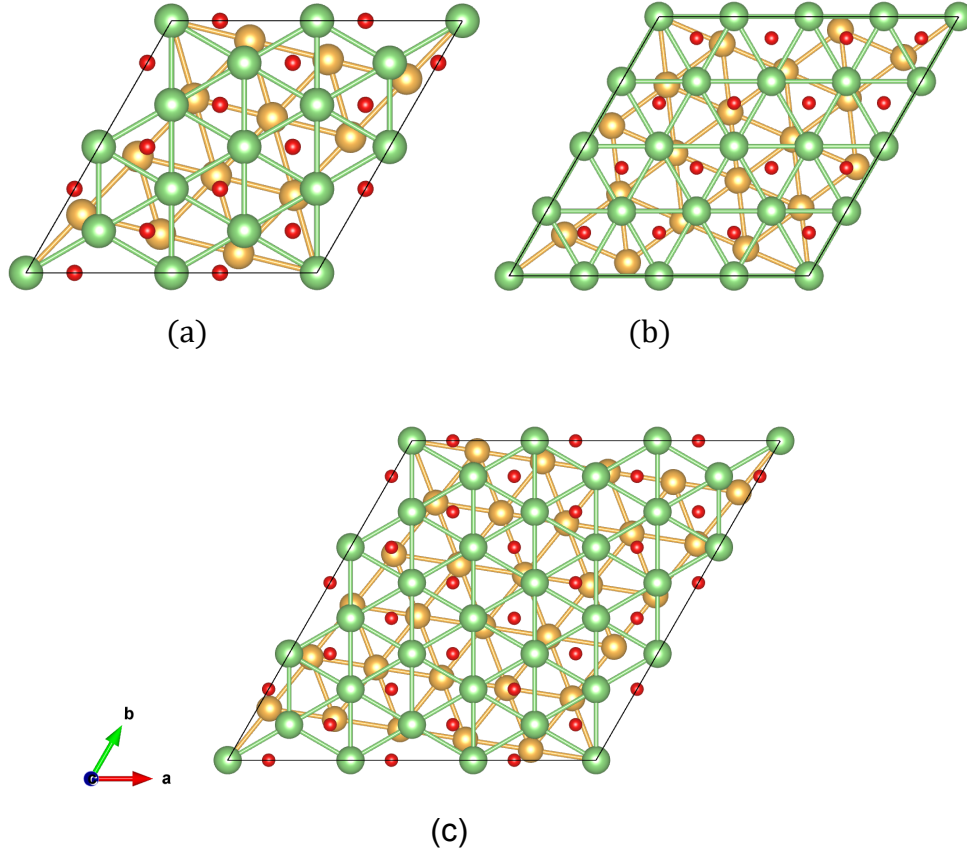


Fig. 6.5: Interfacial atomic configuration between Au (111) and Li<sub>2</sub>O<sub>2</sub> (0001) for different superlattices. (a) Au ( $\sqrt{13} \times \sqrt{13}$ )R13.9°/ Li<sub>2</sub>O<sub>2</sub> ( $2\sqrt{3} \times 2\sqrt{3}$ )R30°, (b) Au ( $\sqrt{19} \times \sqrt{19}$ )R23.4°/ Li<sub>2</sub>O<sub>2</sub> p(4×4) and (c) Au ( $\sqrt{31} \times \sqrt{31}$ )R8.9°/ Li<sub>2</sub>O<sub>2</sub> ( $3\sqrt{3} \times 3\sqrt{3}$ )R30°.

## 6.2 Calculation methods

Periodic supercell method was used for the interface calculation. Since the supercells used in this part of calculation are relatively large, we carried on the structure relaxation by PBE. The lattice constants of bulk Au and Li<sub>2</sub>O<sub>2</sub> are calculated to be 4.16 Å and 3.16 Å. Because of the large lattice misfit between Li<sub>2</sub>O<sub>2</sub> and Au, we performed the interface calculation for both coherent and semicoherent interface configurations. In addition, given the fact that Li<sub>2</sub>O<sub>2</sub> (0001) surface is composed of alternative layers of Li and O atoms, we will consider both the Li-terminating and O-terminating interface structure in the calculation.

### 6.2.1 Coherent interface

For coherent interface, as a common practice, usually gold is treated as the substrate and Li<sub>2</sub>O<sub>2</sub> will adopt the lattice constants of the substrate. However, due to the large lattice misfit, in this way a large in-plan strain of ~ 7% will be introduced into Li<sub>2</sub>O<sub>2</sub> and this will be far from the range of coherent interface. So we compared the elastic properties of Au and Li<sub>2</sub>O<sub>2</sub>, as shown in Fig. 6.6 and Fig. 6.7.

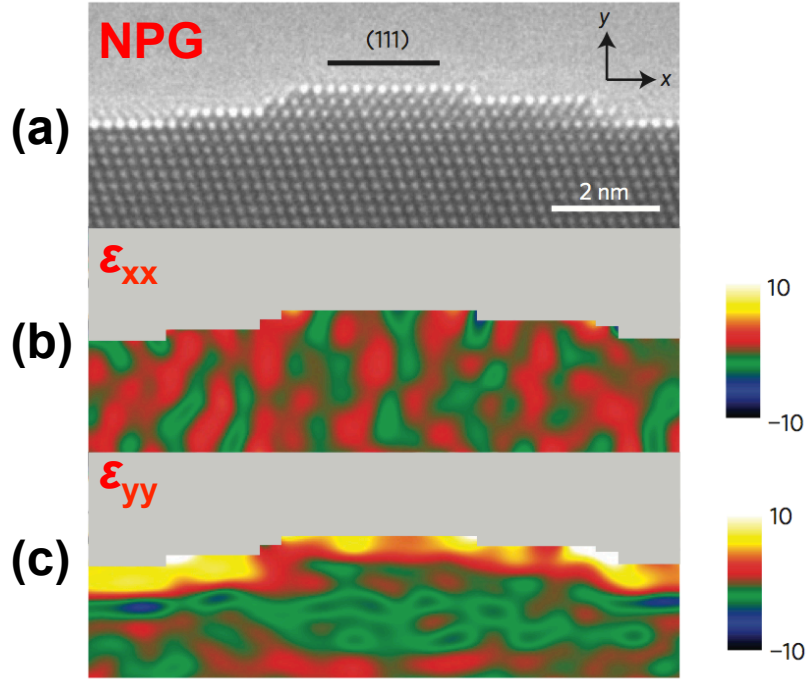


Fig. 6.6: (a) Atomic configuration, surface strain (b) within the plane and (c) out of the plane of gold slab.

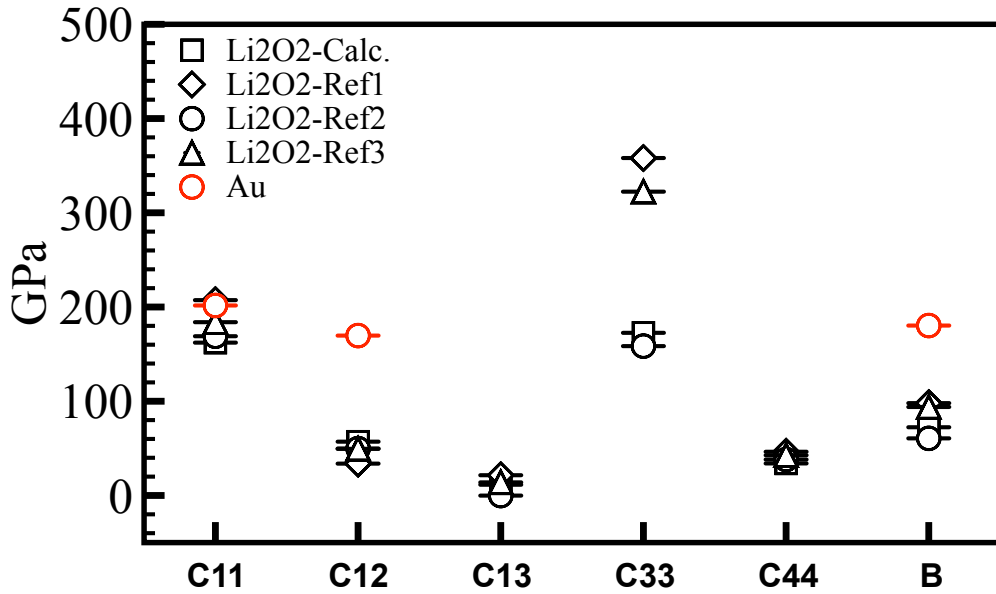


Fig. 6.7: Elastic constants of Li<sub>2</sub>O<sub>2</sub> and Au. The open squares show our calculated values, and others are the results from literature calculations. The red circles are the experimental results of Au.

From the experimental results of Fujita et al in Fig. 6.6, we can find that there exists both in-plane and out-plane strain in Au (111) slab. The out-plane strain

is the dominating strain component and the highest value is around 10% within the top 4 layers of Au. The in-plane component is relatively small than the out-plane one, and an oscillating changing of the strain can be observed.<sup>6</sup> Then from the comparison of elastic constants of Au and Li<sub>2</sub>O<sub>2</sub> in Fig. 6.7, we found both Au and Li<sub>2</sub>O<sub>2</sub> are relatively soft, so it is possible to introduce strain in both phases. Thus in order to reduce the lattice misfit in coherent configuration, we optimized the interface structure by fully relaxing both Au and Li<sub>2</sub>O<sub>2</sub>.

An alternating stacking of Au and Li<sub>2</sub>O<sub>2</sub> slabs without vacuum layer was used in this calculation (see Fig. 6.8). The supercell contains 7 layers of Au atoms, 17 (for O-terminating interface)/19 (for Li-terminating) layers of Li atoms and 9 layers of O-O species, totally 42 (for O-terminating interface)/44 (for Li-terminating) atoms. Two identical interfaces are contained in this supercell structure. A 5×5×1 k-point mesh was used for the calculation. The initial in-plane cell size is set to be 3.05 Å and full relaxation of the cell shape, volume and atomic coordination are performed until the energy is converged within 10<sup>-6</sup> eV, and force converged within 0.02. Moreover, despite the same atomic pattern, there are different binding sites of Li atoms relative to the Au sites, including the top (T) site, bridge (B) site, and hollow (H1/H2) sites. So in this calculation, we also compared the calculation of the different binding sites.

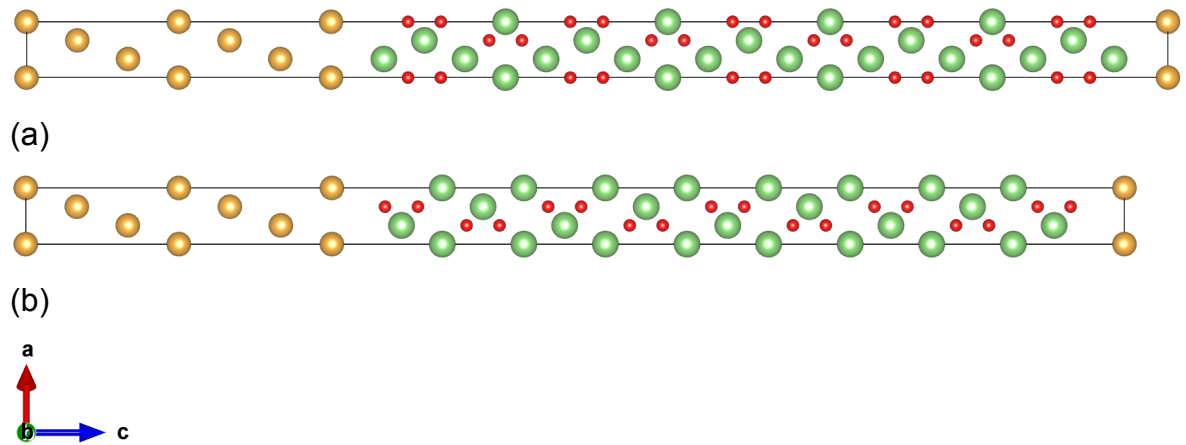


Fig. 6.8: Supercell used for the calculation of coherent interface between Au and Li<sub>2</sub>O<sub>2</sub>. (a) Li-terminating, (b) O-terminating.

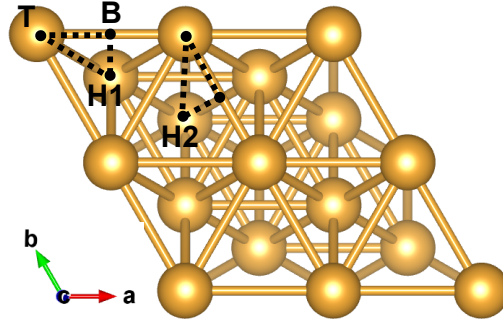


Fig. 6.9: Top (T), bridge (B) and two hollow sites (H1/H2) on the Au (111) surface. H1 and H2 denote two different hollow sites, with H1 showing a ABA stacking pattern of the interfacial Au/Li/O and H2 showing a ABC pattern.

### 6.2.2 Semicohherent interface

For semicoherent interface configuration, we considered the above three different superlattices (see Fig. 6.5) by using a supercell containing 7 layers of Au atoms, 8 (Li-terminating)/7 (O-terminating) layers of Li atoms and 4 layers of O-O species. And a vacuum layer of more than 15 Å was also included in the supercell (see

Fig. 6.10). The total number of atoms of these three different configurations is 283/271, 389/373, 649/622 for the Li- and O-terminating Au ( $\sqrt{13} \times \sqrt{13}$ )R13.9° / Li<sub>2</sub>O<sub>2</sub> ( $2\sqrt{3} \times 2\sqrt{3}$ )R30°, Au ( $\sqrt{19} \times \sqrt{19}$ )R23.4° / Li<sub>2</sub>O<sub>2</sub> p(4×4) and Au ( $\sqrt{31} \times \sqrt{31}$ )R8.9° / Li<sub>2</sub>O<sub>2</sub> ( $3\sqrt{3} \times 3\sqrt{3}$ )R30° interface configuration respectively.

During structure relaxation, the cell shape and volume, together with the bottom layer Au atoms are fixed, while other atoms are allowed to relax until the energy is converged within  $10^{-6}$  eV, and force converged within 0.02. Except for the interface between Au and Li<sub>2</sub>O<sub>2</sub>, there is another free surface of Li<sub>2</sub>O<sub>2</sub>. As the previous calculations demonstrated that the most stable surface of Li<sub>2</sub>O<sub>2</sub> is the O-rich (0001) surface,<sup>4,5</sup> we also constructed this free surface to be the O-rich surface. Given the large supercell used in the calculation, the  $\Gamma$ -point only k-point mesh was used in structure relaxation, and a denser 3×3×1 k-point mesh was used for DOS calculation.

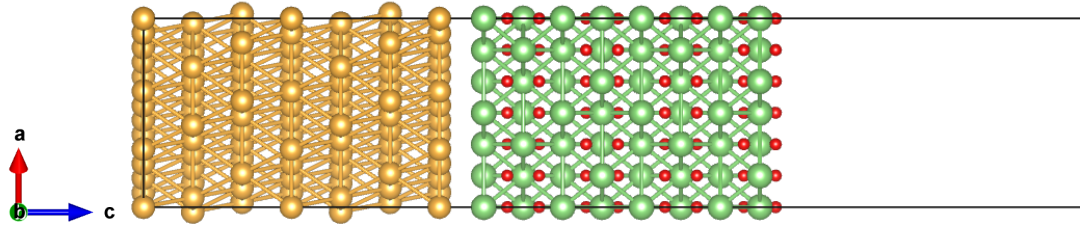


Fig. 6.10: Supercell used for the calculation of semicoherent interface: Li-terminating Au  $(\sqrt{13} \times \sqrt{13})\mathbf{R}13.9^\circ/\text{Li}_2\text{O}_2 (2\sqrt{3} \times 2\sqrt{3})\mathbf{R}30^\circ$ .

## 6.3 Results and discussion

### 6.3.1 Coherent interface

#### 6.3.1.2 Atomic configuration

A fully relaxation of the supercell and atomic coordination was carried for the coherent interface configuration. For both Li-terminating and O-terminating cases, four different binding types, including T, B, H1, and H2, were considered in the calculation. By comparing the total energy of the four binding sites, finally we found that the H2 and H1 binding configurations are the most stable ones for Li-terminating and O-terminating interface respectively.

Here we summarized the atomic bonding distances in

Table. 6.1, and the interfacial atomic configuration in Fig. 6.11.

Interface type	Cell size /Å	Strain (Au)	Strain (Li <sub>2</sub> O <sub>2</sub> )	$d_z(\text{Au} - \text{Li}/\text{O})$ /Å	$d(\text{Au} - \text{Li})$ /Å	$d(\text{Au} - \text{O})$ /Å
Li-term-H2	3.09	5.1%	2.2%	2.23	2.86	3.12
O-term-H1	3.11	5.8%	1.6%	2.32	3.32	2.94

Table. 6.1: The final size, strain and binding distances of the interface structures for both Li- and O-terminating cases.

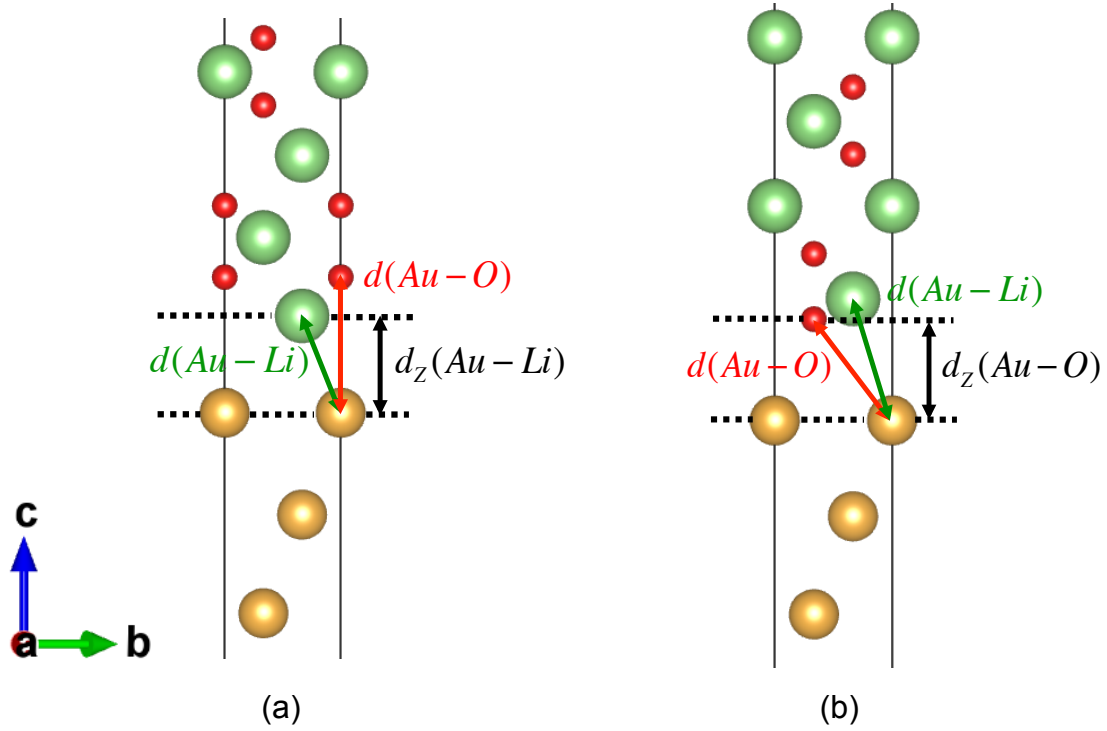


Fig. 6.11: Interfacial atomic configurations and bonding distances for Li-term-H2 and O-term-H1 coherent Au/Li<sub>2</sub>O<sub>2</sub> interfaces.

From the results we found that after structure relaxation, the cell size is 3.09 Å and 3.11 Å respectively for Li- and O-terminating cases. Thus the strain is introduced into Au mainly. However, this result is kindly artificial, because in our interface model, the composition of Li<sub>2</sub>O<sub>2</sub> phase is larger than that of Au. And the binding distance between Au-Li and Au-O to be 2.86 and 2.94, respectively, namely the Li-terminating surface is closer to Au. This result can be easily understood by the surface dipole of Au (111) and Li<sub>2</sub>O<sub>2</sub> (0001) slabs. For metal surfaces, electrons will spill out the surface, so the near the surface area is relatively negatively charged.<sup>7</sup> And for Li<sub>2</sub>O<sub>2</sub> (0001) surface, the Li-terminating surface is positively charged and O-terminating one is negatively charged, thus a closer binding distance between Li and Au is expected.

### 6.3.1.2 Formation energy

For coherent interface structure, the formation energy is calculated by using the following formula:

$$E_f = \frac{1}{2A} (E_{tot} - N_{Au}\mu_{Au} - N_{Li}\mu_{Li} - N_O\mu_O) \quad (\text{Eq. 6.13})$$

where,  $E_f$  is the formation energy of the interface structure,  $E_{tot}$  is the total energy of the supercell.  $A$  is the area of the interface.  $N_{Au}$ ,  $N_{Li}$ ,  $N_O$  are the numbers of Au, Li and O in the supercell. The chemical potential of gold,  $\mu_{Au}$ , is taken as the total energy of bulk gold metal per atom. And the chemical potential of Li and O are related to each other through the total energy of bulk Li<sub>2</sub>O<sub>2</sub>.

$$\mu_{Li} + \mu_O = \frac{1}{2} E_{bulk}(Li_2O_2) \quad (\text{Eq. 6.14})$$

Thus the formation energy can be finally written as:

$$E_f = \frac{1}{2A} [E_{tot} - N_{Au}E_{bulk}(Au) - \frac{1}{2}N_{Li}E_{bulk}(Li_2O_2) + (N_{Li} - N_O)\mu_O] \quad (\text{Eq. 6.15})$$

Besides, the formation energy of interface contains two components, the elastic energy caused by interface misfit and the chemical related energy caused by atomic bonding cross the interface.

$$E_f = E_{st.} + E_{ch.} \quad (\text{Eq. 6.16})$$

$E_{st.}$  stands for the strain energy in each phase, and  $E_{ch.}$  is the chemical related energy. The strain energy related to the interface can be calculated referenced to the energy of bulk phase using the following formula:

$$E_{st.} = \min[E_{slab}(a_S, c) + E_{bulk}] \quad (\text{Eq. 6.17})$$

In this formula,  $E_{slab}(a_S, c)$  is the slab energy per atom. For this slab, the in-plane lattice parameter is  $a_S$ , which is the same with the underlying substrate, and  $c$  is the lattice parameter perpendicular to the plane. In order to calculate the total energy of slab, the in-plane lattice constants are confined as the optimized values of the interface, and the  $c$  parameter is optimized to obtain



an energy minimum. Then the energy difference reference to the bulk phase is taken as the strain energy.

The calculated formation energy, strain energy component as well as the chemical energy components are listed in Table. 6.2.

Table. 6.2: Formation energy, strain energy and chemical energy of the Li- and O-terminating interfaces for the most stable configurations.

Interface type	$E_f$ / (eV/Å <sup>2</sup> )	$E_{st.}$ / (eV/Å <sup>2</sup> )	$E_{ch.}$ / (eV/Å <sup>2</sup> )
Li-term-H2	0.092	0.020	0.072
O-term-H1	0.070	0.015	0.055

The results show that the by subtracting the strain energy in the formation energy, the chemical component is in the range of 0.5~0.7 eV/Å<sup>2</sup>, which is comparable to the formation energy of grain boundary reported in the literature study.<sup>8</sup>

### 6.3.1.3 Differential charge density

In order to investigate the charge transfer mechanism between Au and Li<sub>2</sub>O<sub>2</sub>, we carried out the calculation of differential charge density for the two different interface configurations by using the following formula:

$$\rho_{diff} = \rho_{Au/Li_2O_2} - \rho_{Au} - \rho_{Li_2O_2} \quad (\text{Eq. 6.18})$$

Here,  $\rho_{Au/Li_2O_2}$ ,  $\rho_{Au}$  and  $\rho_{Li_2O_2}$  are the charge density of the whole interface system, the individual Au and Li<sub>2</sub>O<sub>2</sub> systems respectively.

In Fig. 6.12, we plotted the result of differential charge density for Li-terminating and O-terminating system respectively. For Li-terminating interface, the result shows that there is a clearly electron accumulation between the Au and Li layers, and the electrons are mainly from the interfacial Au and O atoms. In contrary, for the O-terminating case, there is a charge reduction between Au and O layers.

In addition, we also calculated the Bader charge for each atom. The results

demonstrated that for Li-terminating case, both the interfacial Au and O-O species have more electrons than the center atoms (0.3e for Au and 0.15e for O-O). Whereas, for O-terminating case, both of interfacial Au and O-O species have a slightly electron lost. This result is attributed to the calculation method of the Bader charge. The electron density at the interfacial region will also be added to the charge of Au and O-O.

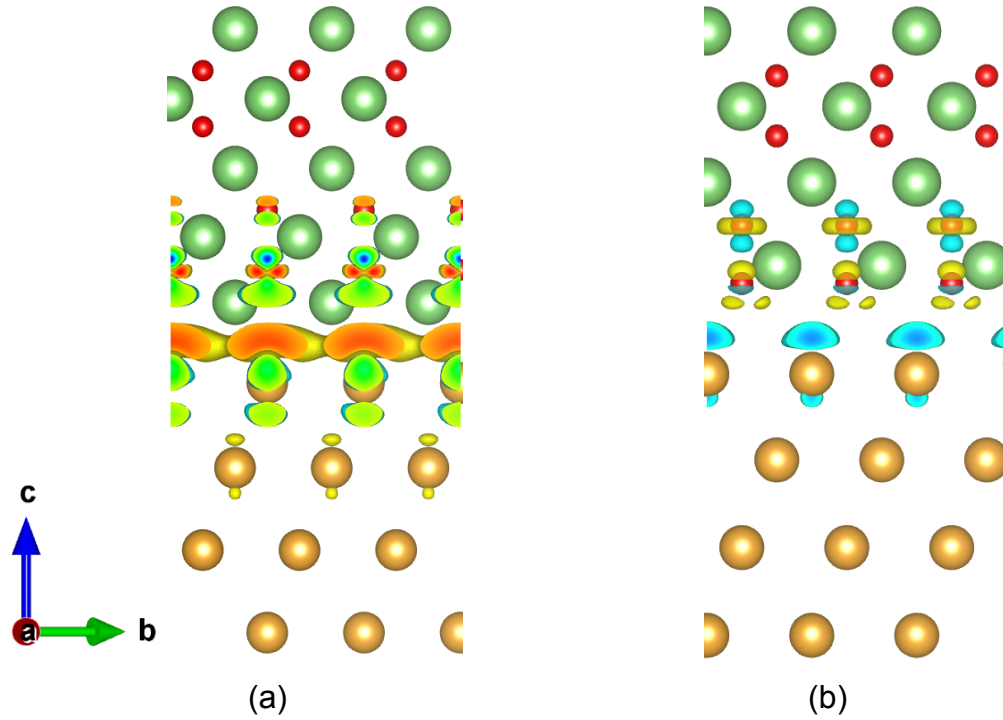


Fig. 6.12: Differential charge density for (a) Li-term-H2 and (b) O-term-H1 coherent Au/Li<sub>2</sub>O<sub>2</sub> interfaces. The isosurface level is  $0.002 a_0^{-3}$  ( $a_0$ : Bohr radius). Yellow denotes gain of electrons and cyan denotes lost of electrons.

#### 6.3.1.4 Electronic structure

To further investigate the interface induced conductivity of Li<sub>2</sub>O<sub>2</sub>, we calculated the density of states (DOS) of the interface structures. The results are shown in Fig. 6.13. From the comparison of the Li-terminating and O-terminating interfaces, we found that the formation of interface leads the O-states shift to lower energy levels for the Li-terminating case, and to a little bit higher than the Fermi level for O-terminating case. The latter is similar to the result of contact states induced by carbon sheets,<sup>1</sup> that some hole states are induced to the valence band of Li<sub>2</sub>O<sub>2</sub>. However, despite the difference, for

both terminating interfaces, the Au states fill the bandgap between the valence and conduction band of Li<sub>2</sub>O<sub>2</sub>. The Au states will finally cause conductivity in the interface system.

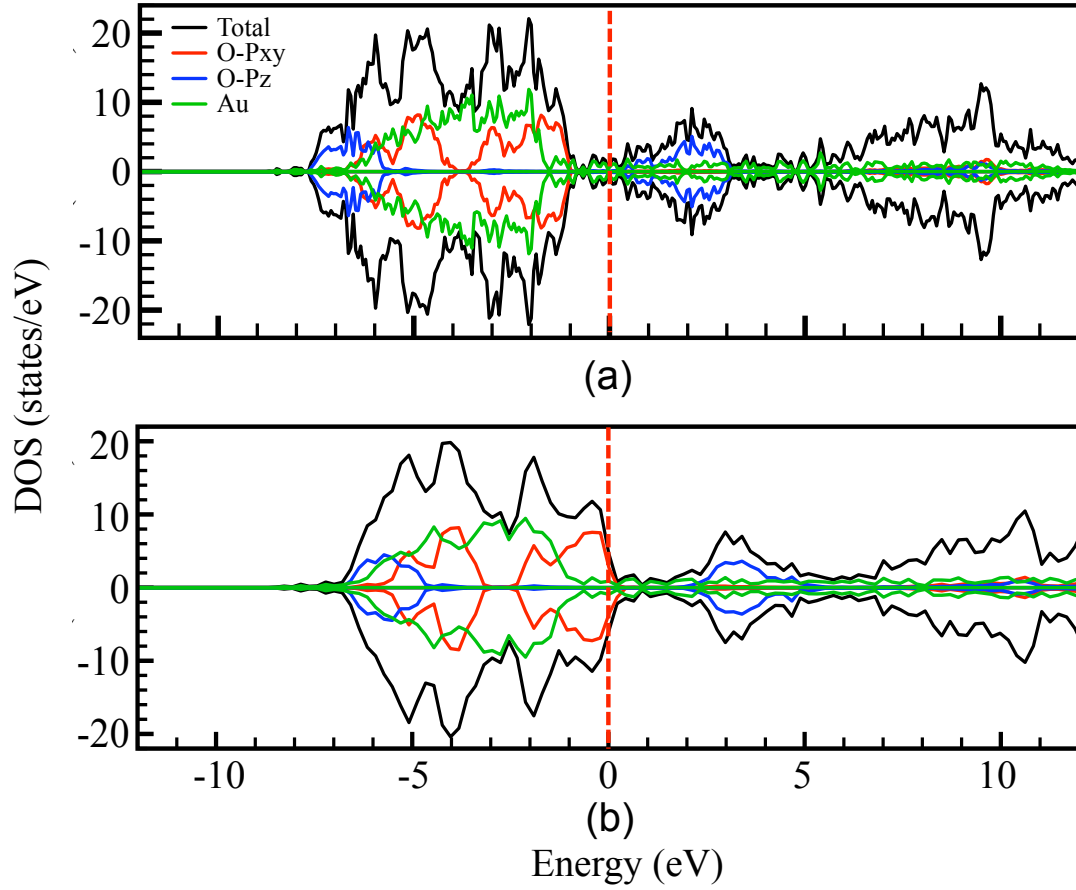


Fig. 6.13: Total and projected DOS on Au and O atoms for (a) Li-term-H2 and (b) O-term-H1 interface configurations.

In addition, the previous calculation of the defective properties has demonstrated that the defect levels are highly depended on the bandgap, consequently the calculation methods. Thus, we also compared the DOS for the Li-terminating system by using PBE, HSE with 25% and 50% exact exchange. The results are shown in Fig. 6.14.

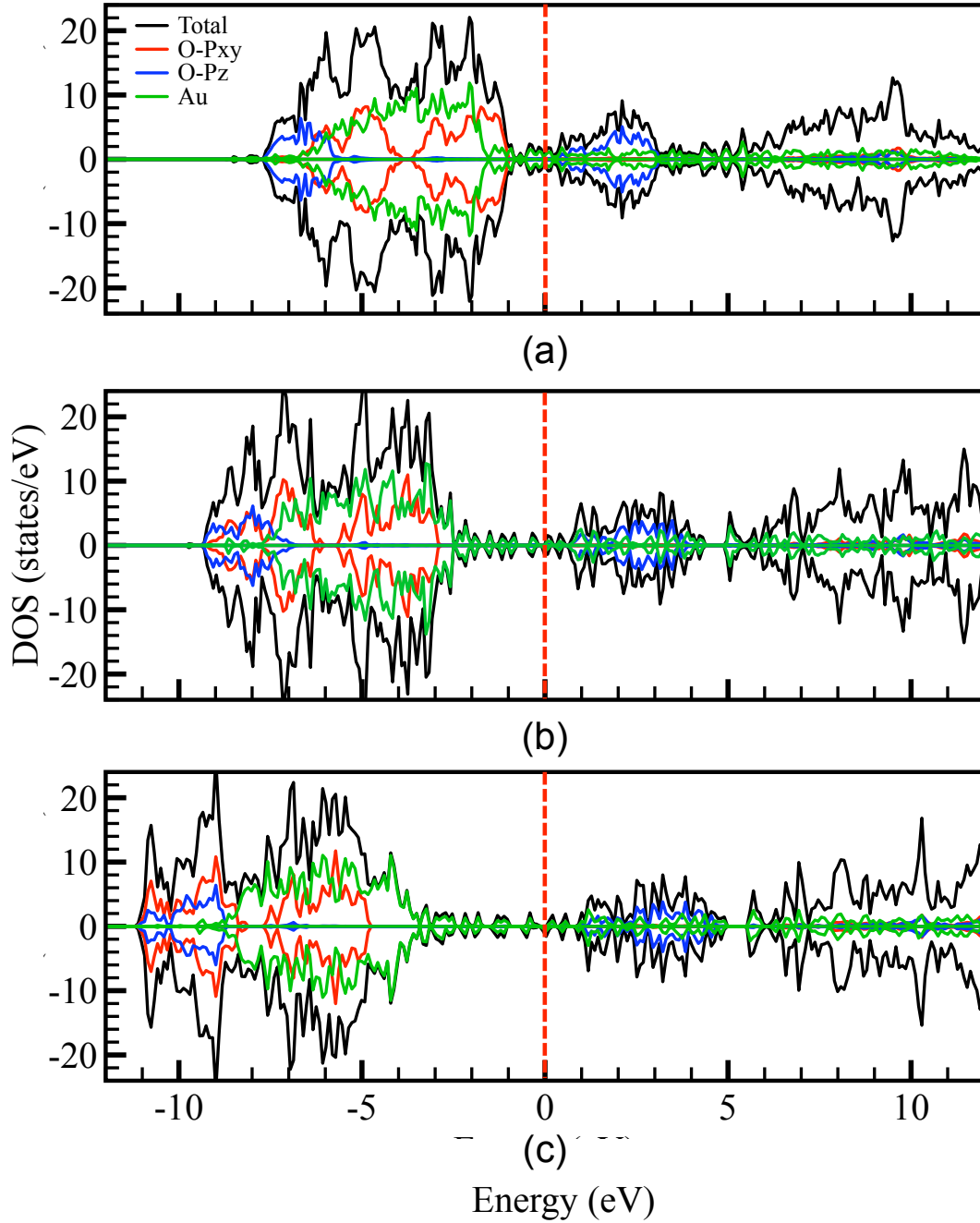


Fig. 6.14: Total and projected DOS on Au and O atoms for Li-term-H2 as calculated by (a) PBE, (b) HSE-0.25 and (c) HSE-0.5 respectively.

The comparison clearly reveals that upon bandgap opening, both the Au and O pxy states shift to lower energy levels. However the O pxy states shift faster than the Au states, and the final relative position of Au and O pxy are changed. By PBE, the O pxy states are higher in energy than the Au states, while by HSE, the O pxy states locate in lower energy level than Au. Nevertheless, the Au states still fill the gap between the valence and conduction band of Li<sub>2</sub>O<sub>2</sub>.

The interface induced conductivity is not changed according to the calculation method.

### 6.3.2 Semicoherent interface

#### 6.3.2.1 Atomic configuration

For this part of semicoherent interface calculation, we selected three different configurations with different lattice misfits (see Fig. 6.4 and Fig. 6.5). After structure relaxation, we found that the Au ( $\sqrt{13} \times \sqrt{13}$ )R13.9°/ Li<sub>2</sub>O<sub>2</sub> ( $2\sqrt{3} \times 2\sqrt{3}$ )R30° configuration with 3.2% misfit will result in a disordered Li<sub>2</sub>O<sub>2</sub> phase, and this is probably due to the still relatively large lattice misfit. As the disordered phase induced conductivity is out of the scheme of our current study, we will not consider this configuration. And for the Au ( $\sqrt{31} \times \sqrt{31}$ )R8.9°/ Li<sub>2</sub>O<sub>2</sub> ( $3\sqrt{3} \times 3\sqrt{3}$ )R30° configuration, even though the lattice misfit in this structure is reduced to less than 1%, however, due to the extremely large supercell, the computation cost is quite large. So in this study we will focus on the third type of configuration, Au ( $\sqrt{19} \times \sqrt{19}$ )R23.4°/ Li<sub>2</sub>O<sub>2</sub> p(4×4). This configuration has a reasonable lattice misfit of 1.4%, and the structural relaxation results in a stable interface structure as shown in Fig. 6.15.

From the results we can clearly see that the free O-rich surface was relaxed to be the same as the previous proposed most stable surface configuration.<sup>4,5</sup> The O-O bond length at the surface is reduced to be 1.46 Å and the outmost Li<sup>+</sup> layers shifted outward to compensate the surface dipole. The interfacial and bulk regions of Li<sub>2</sub>O<sub>2</sub> maintain the ordered structure as that in bulk Li<sub>2</sub>O<sub>2</sub>. Because of the large interface area of this supercell, the binding distances between Au-Li and Au-O distribute in a range. There are four different binding distances between Au-Li: 2.57 Å, 2.62 Å, 2.73 Å, and 2.79 Å. These binding distances are all smaller than that in the coherent configuration. And for Au-O, the binding distances vary from 2.97 Å to 3.37 Å, which are larger than that in coherent configuration. This result indicates that the interface strain introduced into Au and Li<sub>2</sub>O<sub>2</sub> will increase the binding distance between Au-Li and decrease that between Au-O. Alternatively speaking, the artificial strain

in coherent configuration will weaken the interaction between Au and Li layers, and enhance the interaction between Au and O layers. The O-O bond length at the interface region is increased to be 1.57 Å for Li-terminating interface, and similar to the free surface in the O-terminating case. This results indicate that for this semicoherent configuration, the affinity between Au and O-terminating surface might be quite small.

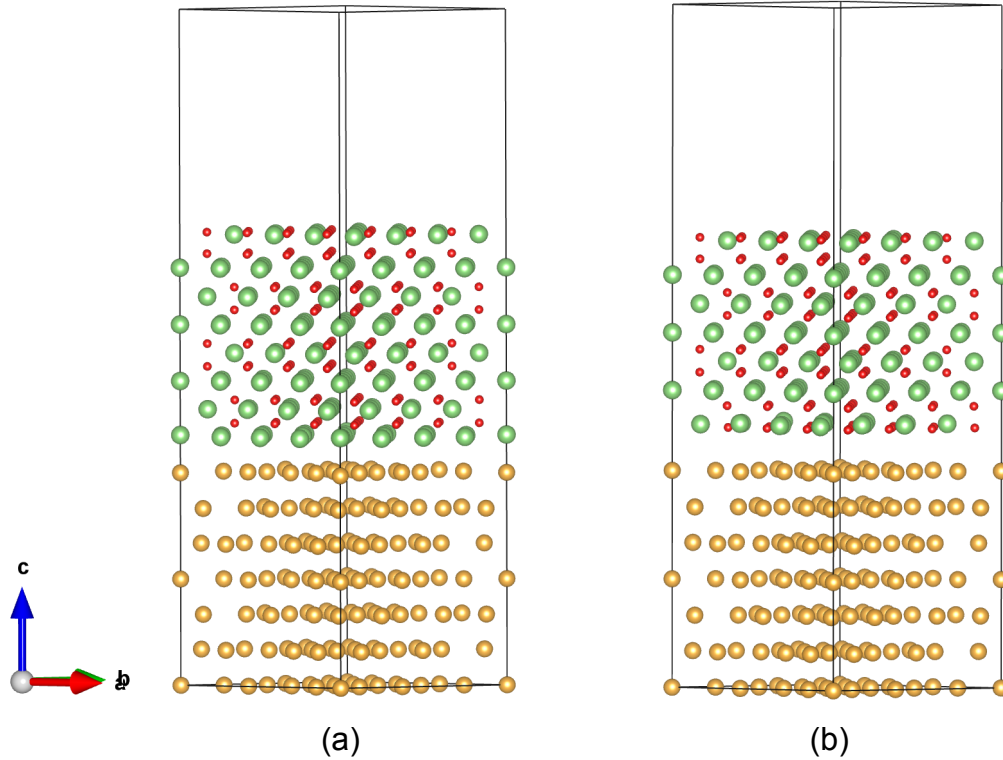


Fig. 6.15: Optimized supercell for (a) Li-terminating interface and (b) O-terminating semicoherent Au ( $\sqrt{19} \times \sqrt{19}$ )R23.4°/Li<sub>2</sub>O<sub>2</sub> p(4×4) interface configuration.

### 6.3.2.2 Differential charge density

As a similar approach, we also calculated the differential charge density for the semicoherent interfaces. Fig. 6.16 gives the results for both two terminating cases. For the Li-terminating case, the calculation gives a similar result to that of coherent configuration, that there is a clear charge accumulation between the Li and Au layers at the interface region. This charge comes from the nearest Au and O-O species, and its magnitude is little bit larger than that of the coherent case. For the O-terminating case, a similar

but greatly reduced charge transfer between the Au- and O-layers was obtained. This result agrees with the atomic configuration of these two structures, that for the O-terminating interface, the interaction between Au and Li<sub>2</sub>O<sub>2</sub> is rather weak.

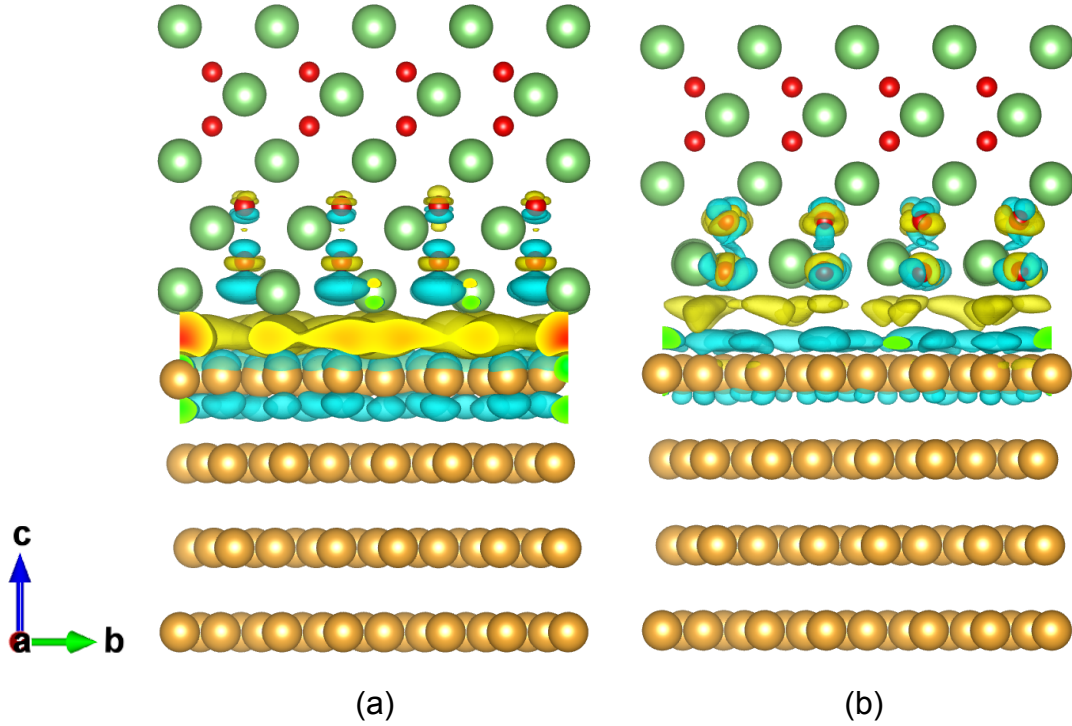


Fig. 6.16: Differential charge density for (a) Li-terminating and (b) O-terminating semicoherent Au ( $\sqrt{19} \times \sqrt{19}$ )R23.4°/Li<sub>2</sub>O<sub>2</sub> p(4×4) interface configuration. The isosurface level is  $0.002 a_0^{-3}$  for (a), and  $0.0005 a_0^{-3}$  for (b) ( $a_0$ : Bohr radius). Yellow denotes gain of electrons and cyan denotes lost of electrons.

### 6.3.2.3 Electronic structure

We continued to calculate the DOS of the interface systems, and the PBE calculated results are given in Fig. 6.17. Similar to the coherent interface configuration, we found the Au states still fill the gap between the O Pxy and O Pz states for both two cases. However, what different from the coherent configuration is that in the semicoherent case, both Li- and O-terminating configurations forms hole in the O Pxy states. And spin polarization was observed, as the majority and minority spin channels are not equal at the Fermi level.

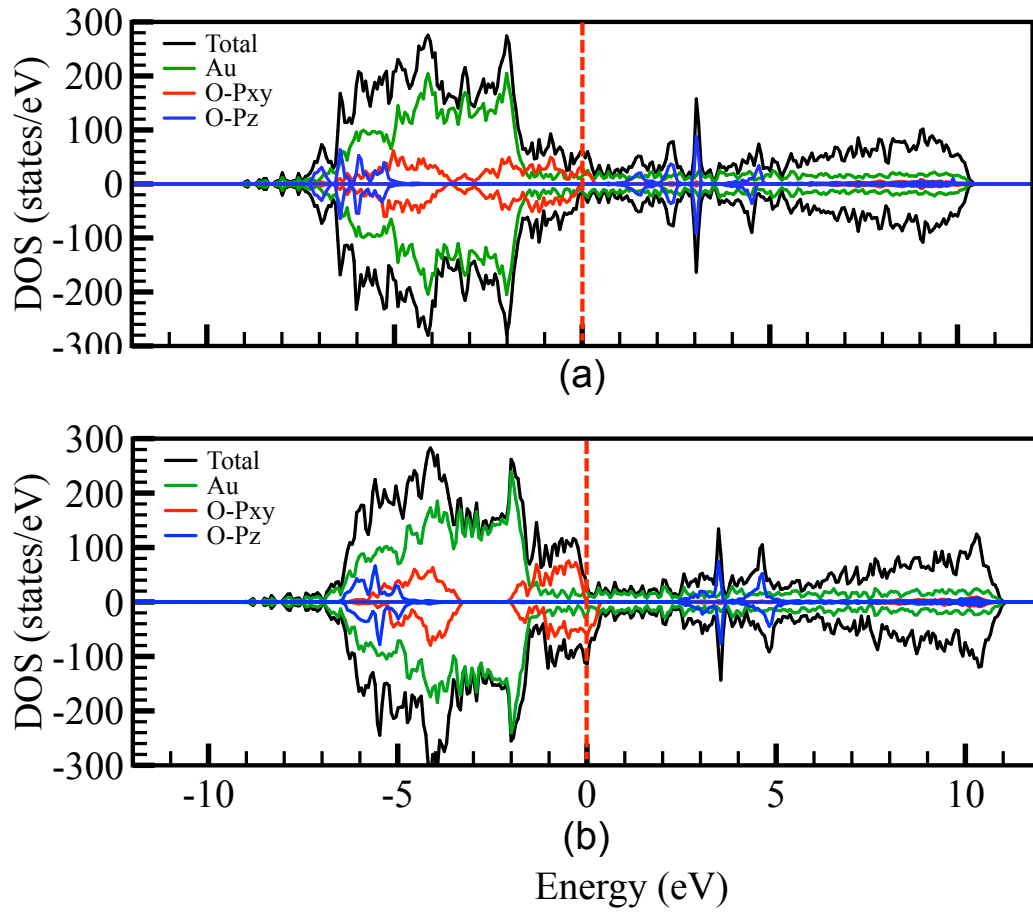
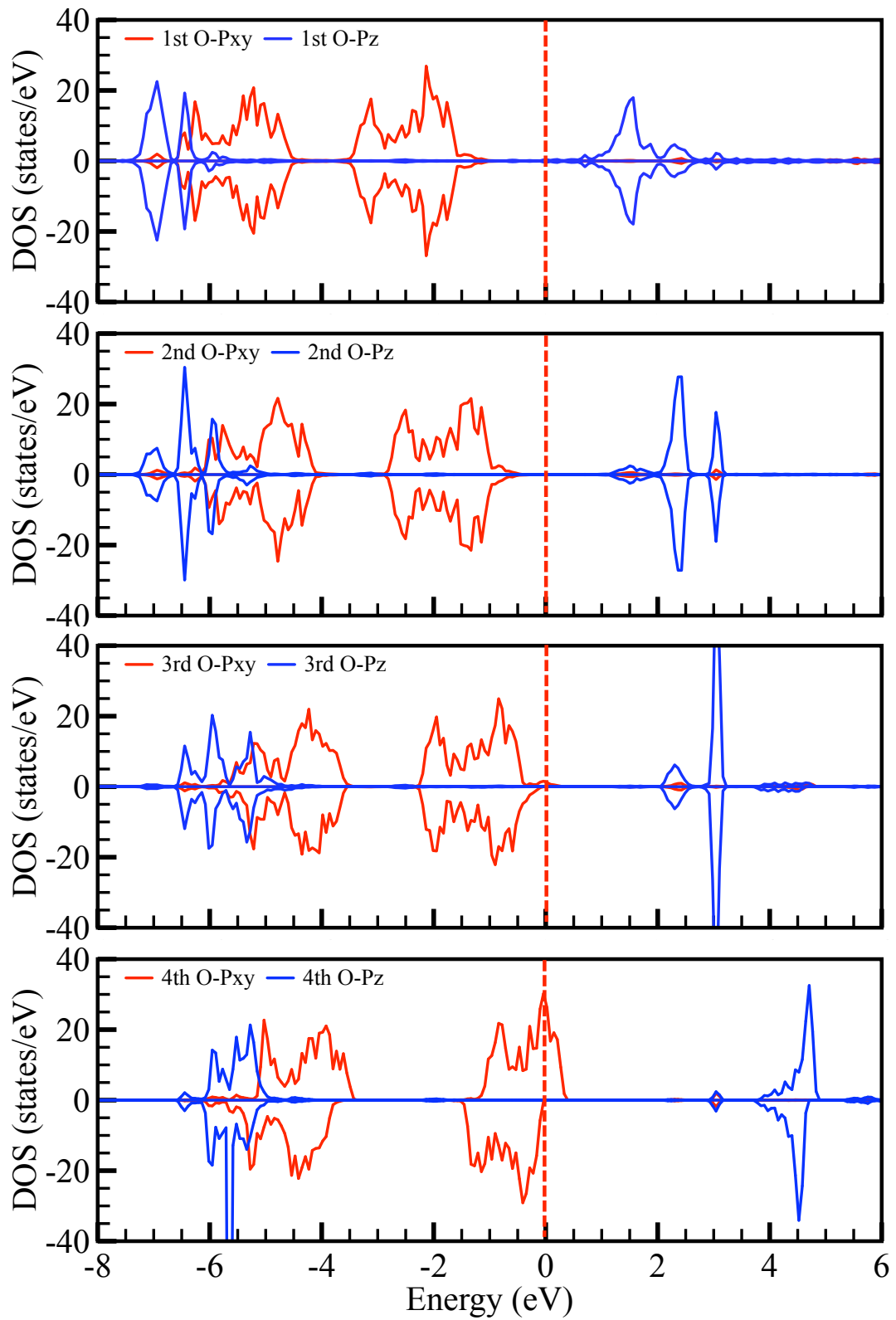


Fig. 6.17: Total and projected DOS on Au and O atoms for (a) Li-terminating and (b) O-terminating semicoherent interface configurations.

Given the fact that in our semicoherent interface configuration, an oxygen rich free surface is also included, and this oxygen rich free surface has been confirmed to be half-metallic by previous calculation,<sup>5</sup> in order to further investigate the interface effect on the DOS, we analyzed the layer-by-layer projected DOS, and the results are plotted in Fig. 6.18.





(a)

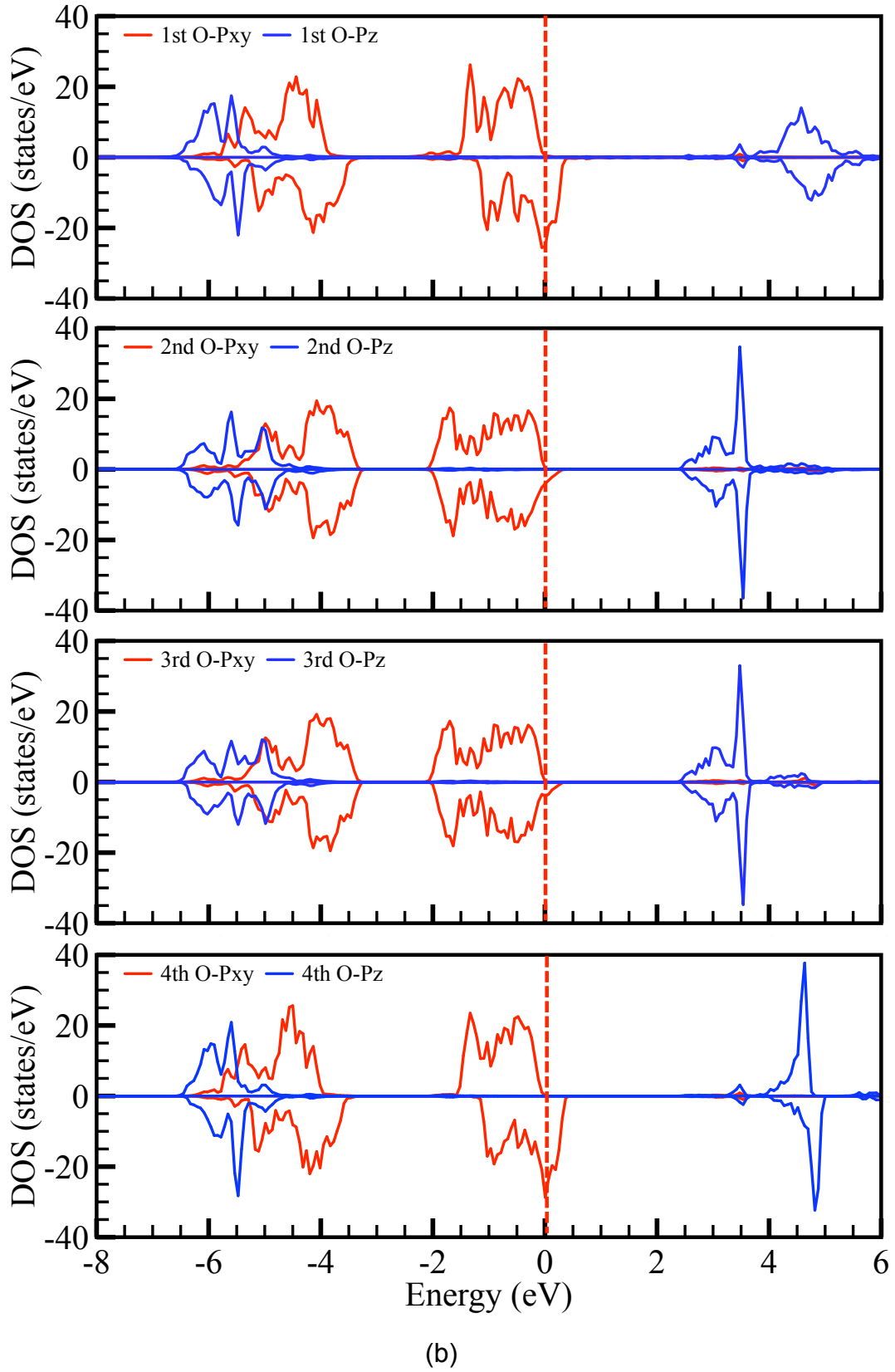


Fig. 6.18: Layer by layer projected DOS on O atoms for (a) Li-terminating and (b) O-terminating semicoherent interface configurations. The number of the layers is counted from the interface to the surface.

From the above layer-by-layer projected DOS, we can easily see the ultimate difference between Li- and O-terminating systems. For Li-terminating case, the O states shift gradually to higher energy levels from the interfacial region to surface. Alternatively speaking, the formation of interface with Au will drag the adjacent O states to lower energy level. Thus the conduction band of O in this region will also move to near Fermi level, effectively reducing the bandgap of Li<sub>2</sub>O<sub>2</sub>. The hole states located on O P<sub>xy</sub> of the total DOS are originated from the surface states. And this result agrees with the previous calculation of the most stable Li<sub>2</sub>O<sub>2</sub> (0001) surface. For the O-terminating case, however the results show that the interfacial DOS are almost the same as the surface states. An almost symmetric result was obtained for these four O-O layers. And the half-metallic property of the interface system is originated from both the O-rich (0001) surface and the interfacial O-rich terminating surface. Thus this result further confirmed the above discussion that the affinity between Au and O-terminating interface is actually quite small.

## 6.4 Conclusions

In this part of study, we performed the calculation for interface between Au and Li<sub>2</sub>O<sub>2</sub>. In order to take the large interfacial misfit into account, we carried out the calculation in both the coherent and semicoherent configurations. The results show that for both configurations, the formation of interface between Au and Li<sub>2</sub>O<sub>2</sub> will introduce conduction states between the valence and conduction band of Li<sub>2</sub>O<sub>2</sub>. These states are from the Au d states, which fill the gap between O P<sub>xy</sub> and O P<sub>z</sub> orbitals. The affinity and charge transfer between Au/Li-terminating interface and Au/O-terminating system are different because of the polar nature of both Au and Li<sub>2</sub>O<sub>2</sub> (0001) surfaces. Compared to the coherent interface configuration, the semicoherent case can greatly reduce the strain energy. And the ultimate difference between Li-terminating and O-terminating interfaces can be obtained in the more realistic semicoherent configuration. Au-Li binding at the interface region will gradually shift the O states of the adjacent O-O layer to lower energy levels,

consequently decrease the bandgap of the Li<sub>2</sub>O<sub>2</sub>, while the weak interaction between the both negatively charged Au-O layers results in almost no change in the electronic structure of Li<sub>2</sub>O<sub>2</sub>.

## REFERENCES

1. Y. Zhao, C. Ban, J. Kang, S. Santhanagopalan, G.-H. Kim, S.-H. Wei, and A. C. Dillon, *Appl. Phys. Lett.*, 2012, **101**, 023903.
2. J. Chen, J. S. Hummelshøj, K. S. Thygesen, J. S. G. Myrdal, J. K. Nørskov, and T. Vegge, *Catalysis Today*, 2011, **165**, 2–9.
3. V. Viswanathan, K. S. Thygesen, J. S. Hummelshøj, J. K. Nørskov, G. Girishkumar, B. D. McCloskey, and A. C. Luntz, 2011, **135**, 214704.
4. M. D. Radin, J. F. Rodriguez, F. Tian, and D. J. Siegel, *J. Am. Chem. Soc.*, 2012, **134**, 1093–1103.
5. M. D. Radin, F. Tian, and D. J. Siegel, *J Mater Sci*, 2012, **47**, 7564–7570.
6. T. Fujita, 2012, 1–6.
7. S. Ling, M. B. Watkins, and A. L. Shluger, *Phys. Chem. Chem. Phys.*, 2013, **15**, 19615.
8. W. T. Geng, B. L. He, and T. Ohno, *J. Phys. Chem. C*, 2013, **117**, 25222–25228.



## Chapter 7 Final conclusions

In this study, we focus on the defective and interfacial properties of  $\text{Li}_2\text{O}_2$  to investigate their effects on the conductivity of  $\text{Li}_2\text{O}_2$ . The calculations are divided into four parts, including the benchmark bulk properties, the intrinsic point defects, the extrinsic point defects, and finally the interfacial properties between Au and  $\text{Li}_2\text{O}_2$ . The following conclusions were obtained for each part in this study:

- 1) Bulk  $\text{Li}_2\text{O}_2$  is a large bandgap insulator, and our HSE06-GW0 result gives a bandgap value of more than 6.50 eV. The electronic structure of  $\text{Li}_2\text{O}_2$  is mainly dominated by the molecular orbital of  $\text{O}_2^{-2}$  peroxide anions. As there is no experimental bandgap value available now, a careful theoretical calculation of its bandgap is essential to obtain a reliable prediction of its other properties.
- 2) The intrinsic defect properties of  $\text{Li}_2\text{O}_2$  are controlled by the ability of  $\text{O}_2^{-2}$  peroxide anion to change its charge states through the formation of electron and hole polarons. Polaron hopping and Li vacancy migration are supposed to be the dominating charge transfer mechanisms related to intrinsic  $\text{Li}_2\text{O}_2$ . The calculated conductivity related these two mechanisms are consistent with the low conductivity in  $\text{Li}_2\text{O}_2$ .
- 3) Metal/semimetal doping in  $\text{Li}_2\text{O}_2$  will result in multi-electron polarons formed next to the dopant atom due to electron donation from the additional valence electrons. Highly localized defect levels form deep acceptor levels, and can hardly be effective to improve the conductivity of  $\text{Li}_2\text{O}_2$ .

Hydrogen atom can be easily incorporated into  $\text{Li}_2\text{O}_2$  as an interstitial impurity. However, both types of hydrogen impurities will electrically counteract with the prevailing conductivity of  $\text{Li}_2\text{O}_2$ .

- 4) The interfacial calculation demonstrated that the Au states will fill the gap between the valence band and conduction band of  $\text{Li}_2\text{O}_2$ , resulting in conductivity.

Thus so far, our calculation proposed that doing in  $\text{Li}_2\text{O}_2$  will not be a wise strategy to improve its conductivity, while the formation of interface between Au and  $\text{Li}_2\text{O}_2$  provides possible mechanism to enhance the conductivity.



